Field-Induced Switching of Ferro-Quadrupole Order Parameter in $PrTi_2Al_{20}$

Takigawa, Sakakibara, and Nakatsuji Groups

The series of Pr-based cubic compounds PrT_2X_{20} (T = Ir, Rh, X = Zn; T = V, Ti, X = Al) has been actively studied recently to explore novel phenomena caused by multipoles of 4*f* electrons because the non-Kramers Γ_3 doublet ground states in the crystalline electric field (CEF) has active quadrupole ($O_Z = 3z^2\text{-}r^2$ and $O_X = \sqrt{3}\,(x^2\text{-}y^2)$) and an octupole ($T_{XYZ} = xyz$) moments but no magnetic dipole moment [1]. Among this series, $PrTi_2Al_{20}$ shows the highest transition temperature of 2 K into a simple ferro-ordered state of O_Z quadrupole moment.

We have performed ^{27}Ai-NMR and magnetization measurements on high quality single crystals of $PrTi_2Al_{20}$ and unexpectedly observed discontinuous switching of quadrupole order parameter by applying small magnetic fields $\boldsymbol{B}$ of a few tesla along [001] and [110] but not along [111] directions [2]. The symmetry of order parameters for different field directions were determined as shown in Fig. 1. For $\boldsymbol{B}$ along [111], there is a single ordered phase of O_Z type below T_Q = 2.2 K, which is independent of B. Here we expect coexistence of three domains, where the symmetry axis $\boldsymbol{Z}$ of the quadrupole moment points along three equivalent <001> directions. The quadrupole order parameter can be conveniently represented as a two-dimensional vector with O_Z and O_X chosen to be the basis (rightmost panel of Fig. 1) [3]. For example, order parameters of the three domains for $\boldsymbol{B} /\!/ [111]$ is given by $O_Z = 3x^2 - r^2 = -O_Z/2 + \sqrt{3}\,O_X/2$ and $3y^2 - r^2 = -O_Z/2 + \sqrt{3}\,O_X/2$, corresponding to the polar angle of 0 and $\pm 2\pi/\sqrt{3}$.

For $\boldsymbol{B}$ along [001], however, discontinuous jump of the NMR frequency occurs near 2 tesla with a finite range of field where two lines coexist, indicating a first order phase transition (Fig. 2a). From the analysis of NMR spectra and

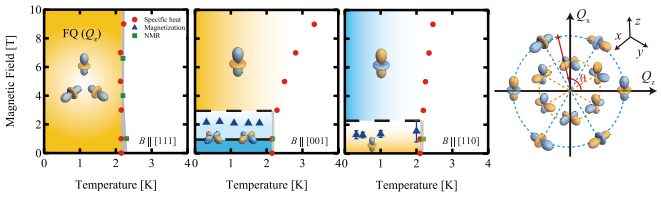

Fig. 1. The temperature vs. magnetic field phase diagram of the ferro-quadrupole order in $PrTi_2Al_{20}$ for B // [111], [001], and [110]. The order parameters are indicated by graphical symbols corresponding to specific values of θ in the order parameter space shown in the rightmost panel. The phase boundaries are determined by the peak of $d(C/T)/dt$, C being the specific heat, splitting of the NMR lines, or kink in the Knight shift. The dashed lines for $\boldsymbol{B} /\!/$ [001] and [110] indicate the region of coexistence of high- and low-field phases. For $\boldsymbol{B} /\!/$ [001] and [110], there is no phase transition but only a crossover as a function of temperature in high fields.

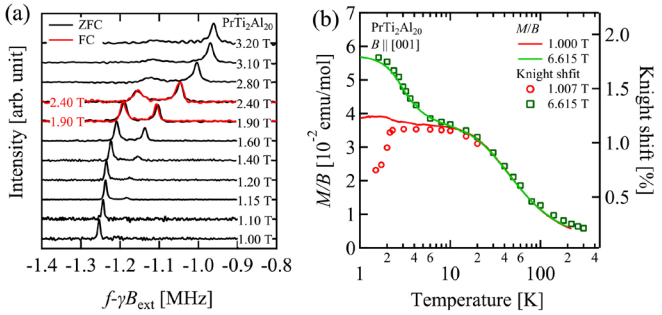

Fig. 2. (a) Magnetic-field dependence of the NMR spectrum (plotted as a function of shift from the nuclear Zeeman frequency) for B // [001] at 1.5 K. (b) The temperature dependences of the Knight shift at low (1T) and high (6.6T) magnetic field along [001] are compared with those of the magnetic susceptibility.

magnetic susceptibility, we conclude that while the high field phase has ferro-order of O_Z with $\boldsymbol{Z} /\!/ \boldsymbol{B}$, the order parameter of the low field phase is closer to O_X type ($\theta \sim \pm\pi/2$). For $\boldsymbol{B}$ along [110], the order parameter changes from O_Z with $\boldsymbol{Z} /\!/ \boldsymbol{B}$ in low fields to $\boldsymbol{Z} \sim -\boldsymbol{B}$ in high fields. The field-induced transition was also confirmed by measurements of heat capacity and magnetocaloric effect [4].

We have developed a Landau theory to identify symmetry allowed interactions between quadrupole and magnetic field, which can account for the experimentally observed switching of the order parameter [2]. Frist, the magnetic field induces mixing between Γ_3 ground doublet and excited CEF levels, leading to the van-Vleck paramagnetism. This anisotropic Zeeman interaction, which is quadratic in $\boldsymbol{B}$, turns out to stabilize the order parameters observed in the high field phases both for $\boldsymbol{B} /\!/ [001]$ and $\boldsymbol{B} /\!/ [110]$, leaving only a crossover as a function of temperature. On the other hand, we found that symmetry allows interaction between quadrupoles on neighboring Pr sites, which is responsible for the ferro-quadrupole order, to depend also quadratically on $\boldsymbol{B}$ for small $\boldsymbol{B}$. This anisotropic interaction competes against the Zeeman interaction and can stabilize the order parameter of the low field phases. Therefore, the observed switching of the order parameter can be explained if the anisotropy of the quadrupole-quadrupole interaction wins the Zeeman interaction at low fields but becomes suppressed at high fields compared with the Zeeman interaction. We have indeed succeeded in reproducing the experimental phase diagram by assuming a non-monotonic field dependence of the anisotropic quadrupole interaction.

Although the mechanism for such a non-trivial field dependence of the quadrupole interaction is not understood yet, anomalous behavior of the NMR Knight shift in the quadrupole ordered states provides an important insight. As shown in Fig. 2(b), the Knight shift at Al sites, which probes the polarization of conduction electron spin, shows the identical temperature dependence to the magnetic susceptibility at a high field (6.6T). At a low field (1T), however, they show remarkable separation below the ordering

temperature, indicating that the hybridization between 4*f* and conduction electrons (*c*-*f* hybridization) is strongly influenced by the quadrupole order. Since the quadrupole-quadrupole interaction is mediated by the *c*-*f* hybridization, this means that the quadrupole order modifies the quadrupole-quadrupole interaction via redistribution of 4*f* charge density, which in turn should affect the order itself. We suspect that such a feedback mechanism may be the key to understand the field-induced discontinuous transition.

References
[1] T. Onimaru and H. Kusunose, J. Phys. Soc. Jpn. **85**, 082002 (2016).
[2] T. Taniguchi *et al.*, J. Phys. Soc. Jpn. **88**, 084707 (2019).
[3] K. Hattori and H. Tsunetsugu, J. Phys. Soc. Jpn. **83**, 034709 (2014).
[4] S. Kittaka *et al.*, J. Phys. Soc. Jpn. **89**, 043701 (2020).

Authors
T. Taniguchi, K. Hattori[a], M. Yoshida, H. Takeda, S. Nakamura, T. Sakakibara, M. Tsujimoto, A. Sakai, Y. Matsumoto, S. Nakatsuji, and M. Takigawa
[a]Tokyo Metropolitan University

Fluctuation-Induced First-Order Transition and Tricritical Point in a Cubic Chiral Magnet EuPtSi

Sakakibara Group

The cubic chiral compound EuPtSi (space group $P2_13$) helimagneitcally orders at T_N=4.0 K with the propagation vector $\boldsymbol{q}_1^*$=(0.2,0.3,0.04). There has been growing interest in this compound because a skyrmion lattice phase with a triple-*q* structure emerges in a magnetic field applied along the [111] direction [1,2]. One of the intriguing features of this compound is that the transition at T_N is of first order [1-3]. We studied the helimagnetic transition on a single crystal of EuPtSi by means of high-precision magnetization measurements, and found that the transition, which is of first order at low fields, becomes of second order at high fields, and there exists a tricritical point (TCP) in the phase diagram [4].

Figure 1 shows the temperature derivative of the magnetization, *dM*/*dT*, in magnetic fields *H* applied along the [110] direction. At *H* = 1.8 kOe, the first-order transition (FOT) is characterized by a sharp peak in *dM*/*dT* at *T* = 4.0 K. By increasing *H*, $T_N(H)$ defined by the peak position in *dM*/*dT* moves to the lower temperature side with a decrease in the peak amplitude. Above *H* = 8.8 kOe, the shape of *dM*/*dT* dramatically changes and excibits a step function like jump at $T_N(H)$, implying that the transition becomes of second order above 8.8 kOe.

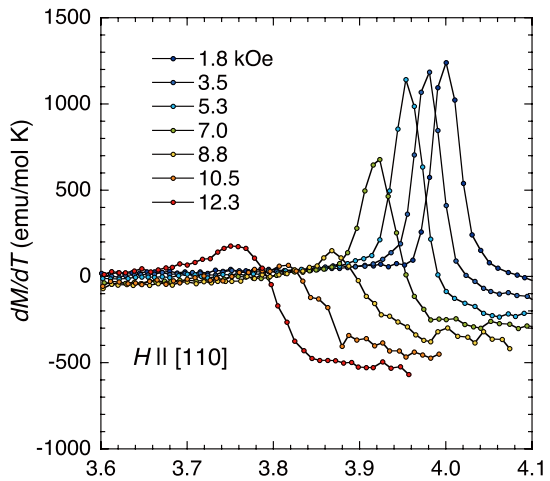

Fig. 1. Temperature derivative of the magnetization *dM*/*dT* of EuPtSi in fields applied along the [110] direction.

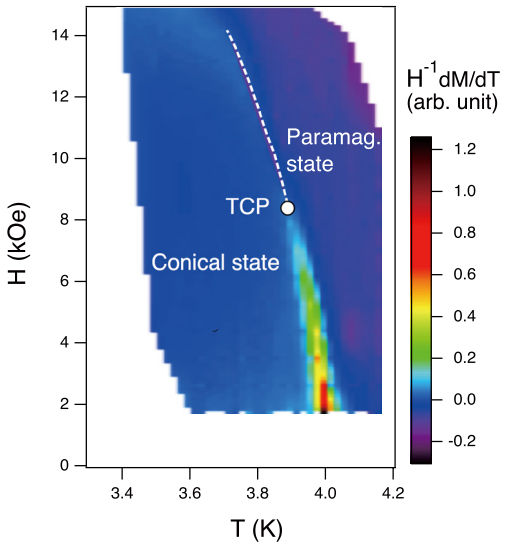

Fig. 2. Phase boundary between the paramagnetic and the single-*q* helical (conical) states of EuPtSi, constructed by colour contour mapping of the *dM*/*dT* data with *H*||[110]. The bright line in low fields indicates the first-order boundary, whereas the dashed line shows the second-order one. TCP denotes the position of the tricritical point.

In order to construct the phase boundary between the paramagnetic and the ordered states, we show in Fig. 2 the color contour mapping of the *dM*/*dT* data for *H*||[110]. The bright line in the low-field region indicates the FOT boundary, and the dashed line in the high-field region denotes the second-order one. In between there is a TCP as indicated in the figure. A similar crossover of the transition has also been observed for [111] and [100] directions [4].

In systems described by order parameters with *n*>4 components, a usual second-order phase transition is avoided due to interactions among critical fluctuations of the order parameters [5]. FOT then takes place when the correlation length exceeds a certain limit, where a discontinuous phase transition occurs to a state energetically favorable. This fluctuation-induced FOT takes place even for systems in which the mean-field theory predicts second-order phase transitions, and the actual transition temperature is suppressed much below the mean-field transition temperature. In EuPtSi, the lattice-symmetry operations on $\boldsymbol{q}_1^*$ yields 12 distinct propagation vectors, which is large enough in number to drive the transition to be first order. Applying a magnetic field reduces the symmetry of the system, and the number of components of the order parameter is effectively decreased, leading to a second-order phase transition. The presence of TCP in the phase diagram in Fig. 2 supports this scenario of a fluctuation-induced FOT in EuPtSi. This situation is favorable for the occurrence of multi-*q* orders such as the skyrmion lattice phase, since they need to be stabilized against a single-*q* helical (or a conical) phase.

References
[1] M. Kakihana *et al.*, J. Phys. Soc. Jpn. **87**, 023701 (2018).
[2] K. Kaneko *et al.*, J. Phys. Soc. Jpn. **88**, 013702 (2019).
[3] D.G. Franco *et al.*, Phys. Rev. B **96**, 014401, (2017).
[4] T. Sakakibara *et al.*, J. Phys. Soc. Jpn. **88**, 093701 (2019).
[5] P. Bak, S. Krinsky and D. Mukamel, Phys. Rev. Lett. **36**, 52 (1976).

Authors
T. Sakakibara, S. Nakamura, S. Kittaka
M. Kakihana[a], M. Hedo[a], T. Nakama[a], and Y. Onuki[a]
[a]University of Ryukyus

Effects of Molecular Dynamics on the Anhydrous Proton Conductivity of Imidazolium Hydrogen Dicarboxylates

Mori Group

Hydrogen (H) is a ubiquitous element, which plays important role in a wide range of fields from the deep underground to the interstellar space, and from inorganic oxides to biosystems. Proton (H^+) migration in solids is one of such extensively studied research topics. Recently, anhydrous organic proton conductors, which can show proton conductivity at above 100 °C without humidification, have attracted scientific interests owing not only to their wide applicability as solid-state electrolytes for fuel cells, but also to their peculiar proton conduction mechanism mediated not by water molecules. However, there have been only a few reports about anhydrous organic proton conductors.

Previously, we investigated the "intrinsic" proton conductivities of imidazolium succinate (= Im-Suc; Fig. 1a) and glutarate (= Im-Glu; Fig. 1b), by single-crystal measurements, and successfully disclosed two key factors for realization of anhydrous proton conductivity: (1) the hydrogen-bond (H-bond) network structures, and (2) difference of the proton donating/accepting abilities between acid and base molecules, i.e., ΔpK_a [1]. In this study, we newly prepared high-quality single crystals of another salt, imidazolium fumarate (Im-Fum; Fig. 1c), in addition to Im-Suc and Im-Glu, and investigated the effect of molecular "dynamics" on the anhydrous proton conductivities of these three salts [2].

Im-Fum has similar 2D H-bond network structure as Im-Suc and Im-Glu (Fig. 1), and showed the anisotropic proton conductivity consistent with the previously disclosed "static" key factors (1) and (2). Interestingly, Im-Fum exhibits linear dependence on the reciprocal temperature in contrast to non-linear dependence in Im-Suc and Im-Glu. We speculated that it is contributed by the imidazolium cation in the 2D H-bond network because the E_a showed quite high values in Im-Suc and Im-Glu similar to the other imidazolium-based salts, and that the molecular orientation of imidazolium cation is different between Im-Fum and the other two. Thus, we investigated the dynamic property of imidazolium cations in these salts by high-temperature X-ray structure analyses and solid-state ^{2}H NMR.

In Im-Suc, a structural transition was observed in X-ray structural analysis at ca. 80 °C, accompanied with the in-plane orientational disorder of imidazolium molecules in one out of two layers. Consistently, the proton conductivity showed abrupt increase at ca. 80 °C, which indicates that the imidazolium libration motion promotes proton conduction in Im-Suc (Fig. 2 upper). On the other hand, no significant

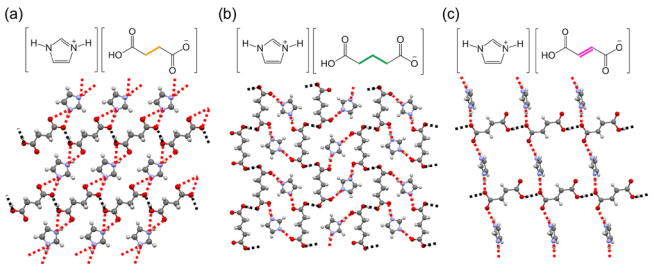

Fig. 1. (upper) Chemical structures and (lower) H-bond network structures of (a) Im-Suc, (b) Im-Glu, and (c) Im-Fum. Red and black dashed lines denote N–H…O and O–H…O H-bonds, respectively.

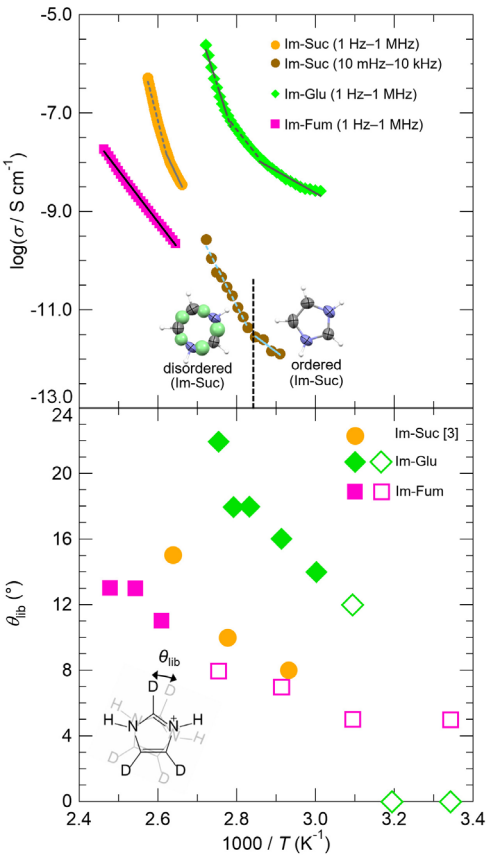

Fig. 2. (upper) The single-crystal proton conductivity (σ) and (lower) libration angle θ_{lib} *vs.* 1000/*T* plots for Im-Suc (orange and dark orange circles), Im-Glu (green diamonds), and Im-Fum (pink squares). In upper graph, the lines denote the Arrhenius fitting, and the inset figures show ordered/disordered imidazolium cation in Im-Suc below/above the transition temperature, ca. 80 °C. In bottom graph, filled circles, diamonds, and squares denote libration angles of Im-Suc (orange)[3], Im-Glu (green), and Im-Fum (pink) in the proton-conducting temperatures, and open markers denote those below proton-conducting temperatures. Inset shows the model for the libration motion of imidazolium cations.

changes were observed for Im-Glu and Im-Fum in X-ray analyses.

Then, in order to investigate the local dynamics of imidazolium cations, we performed the solid-state ^{2}H NMR experiments for Im-Glu and Im-Fum using imidazole-d_3 molecules (Fig. 2 lower inset). By spectral simulations assuming the two-site jump model describing the libration motion of imidazolium molecules, we estimated the librational rates k_{lib} and angles θ_{lib}. Comparing the libration angles θ_{lib} and proton conductivities σ of Im-Glu and Im-Fum together with the reported values of Im-Suc [3], magnitude of θ_{lib} is Im-Glu > Im-Suc > Im-Fum, in consistent with the same relationship of σ. This result clearly indicates that the libration motion of the imidazolium cations promotes proton conduction in these salts.

We consider that this "dynamic" factor synergistically contributes to anhydrous proton conductivity with the already mentioned the "static" factors. Imidazolium molecules lie within the 2D H-bond network in Im-Suc and Im-Glu whereas imidazolium sticks out from the network in Im-Fum (Fig. 1). In former case, directions of libration and proton conduction matches, and the libration can make additional H-bonds or short contacts to promote the proton transfer in the H-bond network, leading to the nonlinear dependence of σ in the Arrhenius plot, whereas it is not for the latter case.

In conclusion, in addition to previously disclosed "static" key factors, (1) H-bond network structures and (2) ΔpK_a between acid and base molecules, we revealed that (3) the molecular "dynamics" is another key factor for realization of anhydrous proton conductivity. These "static" and "dynamic" factors synergistically play important roles, which is thought as peculiar nature of Grotthuss-type conduction in anhydrous solids.

References

[1] Y. Sunairi, A. Ueda, J. Yoshida, K. Suzuki, and H. Mori, J. Phys. Chem. C **122**, 11623 (2018).
[2] Y. Sunairi, S. Dekura, A. Ueda, T. Ida, M. Mizuno, and H. Mori, J. Phys. Soc. Jpn. **89**, 051008 (2020).
[3] T. Umiyama, R. Ohashi, T. Ida, and M. Mizuno, Chem. Lett. **42**, 1323 (2013).

Authors

Y. Sunairi, S. Dekura, A. Ueda[a], T. Ida[b], M. Mizuno[b], and H. Mori
[a]Kumamoto University
[b]Kanazawa University

Topological Properties of τ-Type Organic Conductors

Osada Group

It is desirable that topological phases can be realized in organic molecular crystals with high designability. However, the search for topological states in organic crystals has met with some challenges. Generally, organic molecular crystals have too poor symmetry to protect topological states. The width of their tight-binding band is too narrow to cause the band inversion. Moreover, organic molecules consist of light elements with correspondingly small spin–orbit coupling (SOC). So far, only a few molecular crystals, such as a two-dimensional (2D) Dirac semimetal α-(BEDT-TTF)$_2$I$_3$ and a 3D nodal-line Dirac semimetal Pd(dddt)$_2$, have been studied as topological materials in the field of organic conductors.

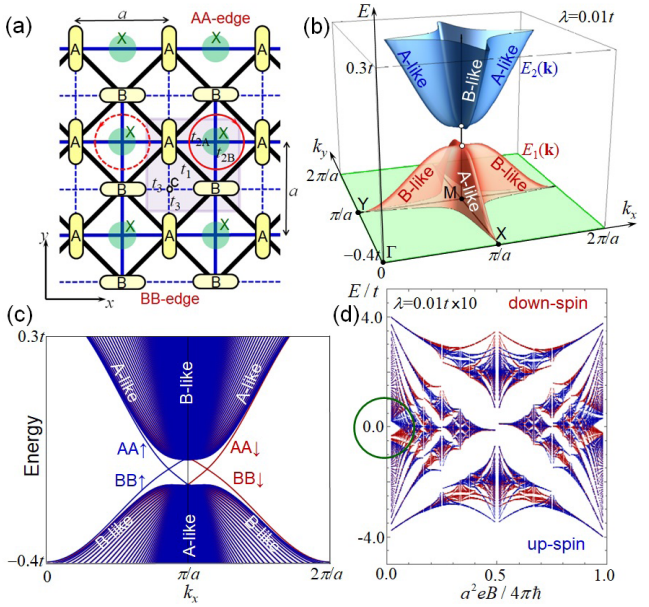

Fig. 1. (a) Schematics of a conducting layer of τ-type organic conductors. A and B indicate donor molecule sites, and X indicates anion sites. (b) Bulk band dispersion of τ-type conductors with finite spin-orbit coupling (SOC). A gap opens at the quadratic band contact point at M. (c) Energy dispersion of the system with finite width. Helical edge states along AA and BB edges appear in the gap. (d) Hofstadter butterfly (energy spectra as a function of magnetic field) of τ-type conductors. Blue and Red patterns correspond to up-spin and down-spin, respectively. The value of SOC is enlarged to see its effect easily.

Here, we demonstrate that the conducting layer of τ-type organic layered conductor, τ-(EDO-S,S-DMEDT-TTF)$_2$X$_{1+y}$ and τ-(P-S,S-DMEDT-TTF)$_2$X$_{1+y}$ (X=AuBr$_2$, I$_3$, IBr$_2$), is a 2D electron system with unique topological properties [1]. On each layer, donor molecules (EDO-S,S-DMEDT-TTF or P-S,S-DMEDT-TTF) form a square lattice, and anion molecules (X) are arranged on it with a checkerboard pattern as shown in Fig. 1(a). This lattice structure is a modification of Mielke's lattice, which is a typical flat band system, so that topological natures of Mielke's lattice are inherited. In addition, rather strong spin-orbit coupling (SOC) can be expected in τ-type conductors, although SOC is generally weak in organic materials. It results from the strong in-plane potential modulation generated by the inorganic anion X. Using a Kane-Mele type model, we discuss possible topological properties of the τ-type organic conductors.

In the absence of SOC, the conduction and valence bands with four-fold rotational symmetry show quadratic band touching. Since the Fermi level is located in the conduction band, the actual τ-type organic conductors (y = 0.75~0.875) have is a star-shaped electron Fermi surface. Under the in-plane uniaxial strain breaking the four-fold symmetry, the band contact point splits into a pair of Dirac cones. This is a kind of Lifshitz transition from a 2D Luttinger semimetal to a 2D Dirac semimetal.

Once the SOC becomes finite, a small gap opens at the band contact point as seen in Fig. 1(b). The product of the valence band parity values at symmetric point (time-reversal invariant momentums) is -1. This fact indicates that the gapped state is a topologically nontrivial insulator with band inversion. In fact, there exists a helical edge state characteristic to the quantum spin Hall insulator (Z_2-topological insulator) along each edge as shown in Fig. 1(c). Therefore, the actual τ-type conductors could be regarded as heavily-doped topological insulators. Since they have finite spin-dependent Berry curvature at the Fermi level, finite spin Hall effect could appear although its experimental detection needs microfabrication of samples.

Because of finite spin-dependent orbital magnetic moment due to SOC, the Landau levels (LLs) have additional spin splitting to the Zeeman effect. Figure 1(d) shows the Hofstadter butterfly of the LLs for each spin subband. Since the Zeeman effect is not included in this figure, the difference of both spin levels indicates the orbital contribution to the spin splitting due to SOC. At the zero-field limit, we can see the Chern number below the SOC gap takes finite values of -1 or +1 depending on the spin. As actual τ-type conductors are doped up to 10% of the conduction band, the orbital contribution to the spin splitting is about several % of the Zeeman splitting, which is possible to detect experimentally in the Shubnikov-de Haas oscillations at low temperature and high magnetic fields.

Reference

[1] T. Osada, J. Phys. Soc. Jpn. **88**, 114707 (2019).

Authors

T. Osada, T. Taen, K. Uchida, M. Sato, and A. Kiswandhi

Nonequilibrium Dynamics in Strongly Correlated Electrons in One Dimension and Clogged Charge Current

Tsunetsugu Group

Understanding nonequilibrium dynamics in strongly correlated systems is an important issue and a big challenge for both theorists and experimentalists. Recently proposed generalized hydrodynamic (GHD) theory [1] succeeds in describing nonequilibrium dynamics in one-dimensional models that are exactly solvable through the Bethe ansatz (BA) equations. Its fundamental degrees of freedom are local distribution function of multiple types of "quasiparticles" corresponding to real roots and complex roots (strings) in the BA equations. These distribution functions evolve in space and time following continuity equations, and these equations include effective velocities that need to be determined self-consistently from the local distribution functions.

We have applied the GHD theory to the one-dimensional Hubbard model and studied quench dynamics with a partitioning protocol [2]. The system is initially divided at the origin $x = 0$ to two semi-infinite parts. The left part is equilibrated at a fixed temperature with half-filling electron density, while the right part is set empty and has no electrons. At time $t = 0$, the two parts are connected and start to evolve. In this case, local physical quantities depend only on the ray $\xi = x/t$, and vary continuously in the transient region $V_L < \xi < V_R$. We have calculated charge and energy densities, $n(\xi)$, $e(\xi)$, and their currents, $j_n(\xi)$, $j_e(\xi)$, and examined the proportionality relation between $j_n(\xi)$ and $j_e(\xi)$. An interesting finding is a phenomenon we named *clogging*. Inside the transition region, there appears at high temperatures a region that has *zero charge current* although nonzero energy current flows. This clogged region locates next to the left part with half-filling electron density. A similar behavior was found for spin current in quantum spin systems [3]. We proved its presence in the infinite temperature limit, and also confirmed by numerical calculations a finite region size, which shrinks with decreasing temperature. In the clogged region, one type of quasiparticles have the same charge as electron and they flow towards the empty side as one expects. This charge current is cancelled by the counterflow carried by other types of quasiparticles that are bound states of multiple electrons. All the types of quasiparticles carry negative energy towards the empty part, thus leading to a nonzero energy current in the clogged region.

The clogging of charge current is an interesting unexpected behavior in nonequilibrium dynamics of strongly correlated electrons in one dimension, and it is worth trying to observe it in experiments.

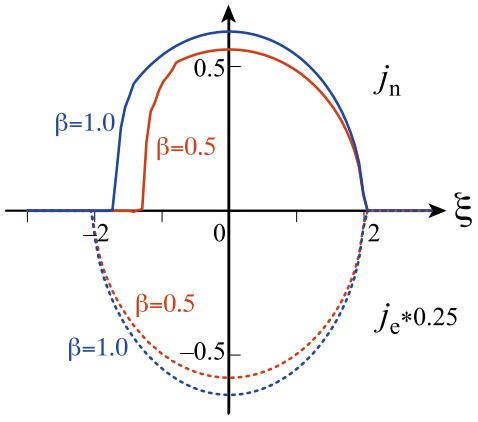

Fig. 1. Profile of charge and energy currents at reciprocal temperature $\beta = 0.5$ and 1.0. Coulomb repulsion is $U = 8$, and energy units are the electron transfer energy. Charge current j_n is normalized by the electron charge –|e|.

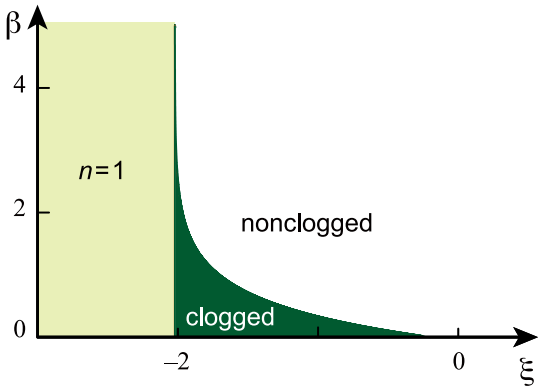

Fig. 2. Change of clogged region with reciprocal temperature β at U=8.

References

[1] O.A. Castro-Alvaredo, *et al.*, Phys. Rev. X **6**, 041065 (2016); B. Bertini *et al.*, Phys. Rev. Lett. **117**, 207201 (2016).
[2] Y. Nozawa and H. Tsunetsugu, Phys. Rev. B **101**, 035121 (2020).
[3] L. Piroli *et al.*, Phys. Rev. B **96**, 115124 (2017).

Authors

H. Tsunetsugu and Y. Nozawa

High-Harmonic Generation in Solids

Kato Group

Recently, high-harmonic generation (HHG) in solids has been experimentally observed. In contrast to that of the gaseous media, solids have the vastly diverse nature such as in their band structures, energy gaps, crystalline anisotropy, magnetism, and so on. Thus, HHG shows various properties depending on the materials, and clarifying the universal properties of HHG in solids should be needed to progress the high-intensity optical technology.

Based on this motivation, we have theoretically investigated HHG mechanism in solids. In Ref. [1] and [2], we have shown that the HHG mechanism can be classified into three regimes depending on the field intensity: (i) the multiphoton absorption regime, (ii) ac Zener regime, and (iii) semimetal regime. This consideration enables us to predict that HHG in graphene would show unique properties in its ellipticity dependence, and this was identified in the experiment [3]. In this consideration, a concept of the field-induced dynamic band structure is essential to gaining a full understanding of extreme nonlinear optics in solids. Although fundamental mechanisms of HHG in solids have already been revealed [3], the connection between HHG and other high-field phenomena, such as the dynamical Franz-Keldysh effect, above-threshold ionization, and dynamical localization has

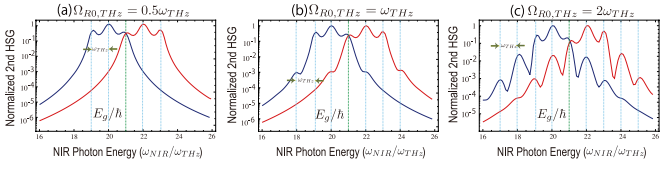

Fig. 1. NIR frequency dependence of 2nd HSG for $E_g = 21\omega_{THz}$ in the case of (a) $\Omega_{THz} = 0.5\omega_{THz}$, (b) $\Omega_{THz} = \omega_{THz}$, and (c) $\Omega_{THz} = 2\omega_{THz}$. The blue and red lines indicate positive and negative 2nd HSG, respectively.

not been clarified yet. It appears that HHG and these optical phenomena are different aspects of the same electron interaction with the strong light field. We tried to clarify the relation between HHG and these phenomena, by supposing the pump-probe spectroscopy where weak near infrared (NIR) and strong terahertz (THz) light are simultaneously imposed.

The weak NIR and strong THz lights induce the high-order sideband generation (HSG), which changes depending on the THz intensity and NIR frequency. These changes are considered as a probe of the modified states of solids under strong THz light irradiation. Figures 1 (a)-(c) show the intensities of 2nd positive and negative HSG as a function of NIR frequency (ω_{NIR}) for different THz intensities (Ω_{THz}). These figures indicate that with increasing the THz intensities, more peaks at different frequencies of ω_{THz} become visible, which reflects the modified state of the system has new energy levels around the band-gap energy. By an analytical consideration, we have shown that these energy levels (subbands) are derived from a concept of the field-induced dynamic band structure, as shown in Fig. 2(a). We have also shown that kth Bessel function, $\Omega_{\mathrm{THz}}J_k(\Omega_{\mathrm{THz}}/\omega_{\mathrm{THz}})$, effectively describes mixing matrix elements between the kth subband and the valence band, which can be used for a rough estimate of the transition amplitude. This presumption could be identified by numerical calculation, as shown in Fig. 2(b), where the positive 2nd HSG resonates to subbands with their energy levels $E_g = 20\omega_{\mathrm{THz}}$, $E_g = 19\omega_{\mathrm{THz}}$, and $E_g = 18\omega_{\mathrm{THz}}$, respectively (see Fig. 2(a)). These non-monotonic properties are generally confirmed in other high-field phenomena such as the dynamical Franz-Keldysh effect and dynamical localization. Thus, we could clarify the relationship between HHG and other high-field phenomena and suggest a new experiment for identifying oscillatory behavior that would be observed in field-intensity dependence of HHG in solids [5].

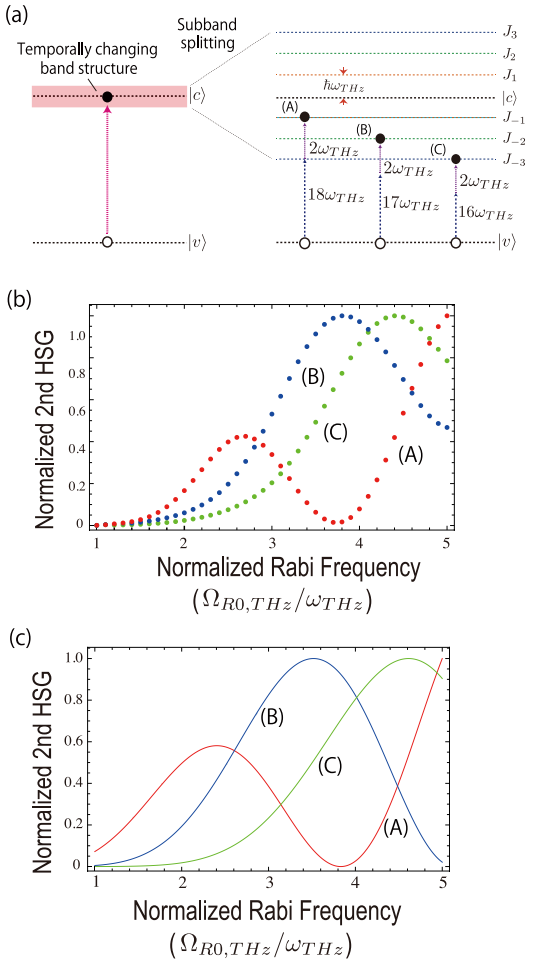

Fig. 2. (a) Schematic diagram of the subband picture originating from temporally changing band structure. (b) Numerical results of positive 2nd HSG as a function of $\Omega_{\mathrm{THz}}/\omega_{\mathrm{THz}}$. Here, the red, blue, and green dots indicate (A) $\omega_{\mathrm{NIR}} = 18\omega_{\mathrm{THz}}$, (B) $\omega_{\mathrm{NIR}} = 17\omega_{\mathrm{THz}}$, and (C) $\omega_{\mathrm{NIR}} = 16\omega_{\mathrm{THz}}$, respectively, whose processes are illustrated in (a). Inset figure: Analytic results of 2nd HSG as a function of $\Omega_{\mathrm{THz}}/\omega_{\mathrm{THz}}$. The red, blue, and green lines show $|xJ_{-1}(x)|^2$, $|xJ_{-2}(x)|^2$, and $|xJ_{-3}(x)|^2$, respectively, where $x = \Omega_{\mathrm{THz}}/\omega_{\mathrm{THz}}$.

References

[1] T. Tamaya *et al*., Phys. Rev. Lett. **116**, 016601 (2016).
[2] T. Tamaya *et al*., Phys. Rev. B **94**, 241107(R) (2016).
[3] N. Yoshikawa, T. Tamaya, and K. Tanaka, Science **356**, 736 (2017).
[4] T. Tamaya and T. Kato, Phys. Rev. B **100**, 081203(R) (2019).
[5] P. Xia*, T. Tamaya*, C. Kim, F. Lu, T. Kanai, N. Ishii, J. Itatani, H. Akiyama, and T. Kato: arXiv:2004.04492. (*equally contributed)

Authors
T. Tamaya and T. Kato

Electric Control of Flying Qubit on Quantum Hall Edge Channels

Katsumoto Group

For composing a quantum circuit with electron spins, "flying qubits" (FQs) are used for transferring quantum information between qubit clusters. A simple realization of FQ is an electron wave packet, which brings 1 qubit information as its spin. In a flight process, quantum decoherence, *i.e.* loss of information should be avoided, and also a unitary operation on the FQ is desirable. In the quantum Hall effect one-dimensional channels are formed at the sample edges (quantum Hall edge channel, QHEC) and the quantum coherence of electronic states on them are robust against disturbances from the environment. Also when the magnetic

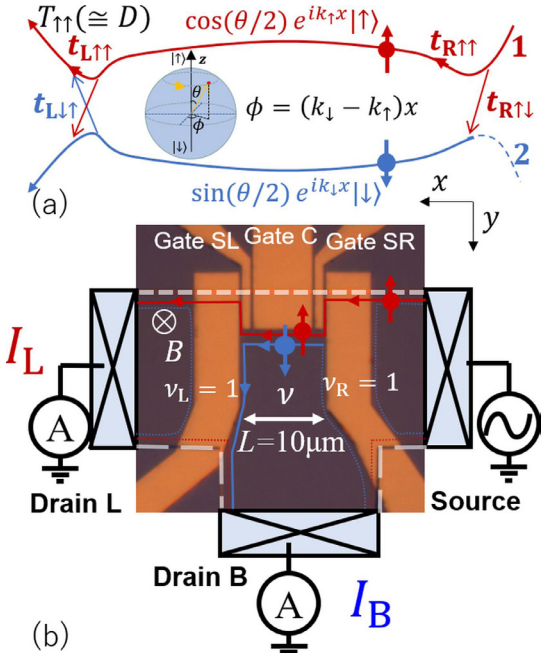

Fig. 1. (a) Schematic diagram of unitary operation on an electron spin flying qubit. An FQ is injected to channel-1 and some portion of the wave packet tunnels into channel-2 with down spin (gaining of zenith angle.) During the travel, the FQ gains azimuth angle via the difference in the kinetic phase. The spin state is detected as the overall transmission amplitude. (b) Optical micrograph of metallic gates (regions with orange color) configuration fabricated on a 2DES. Edge conduction channels and measurement circuits are illustrated and superposed.

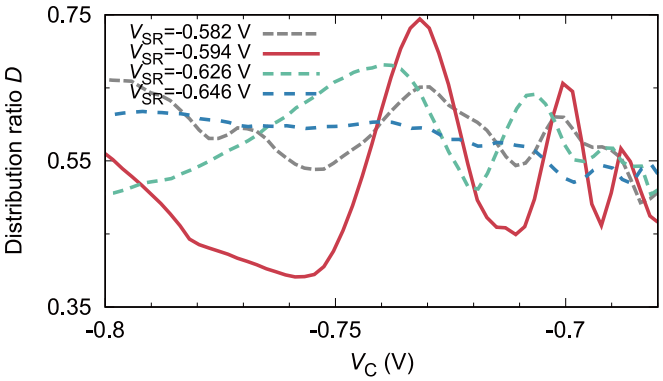

Fig. 2. Current distribution ratio to drain L, which is equal to the overall transmission coefficient of channel-1 in Fig.1(b) as a function of center gate voltage.

field is strong enough, the electronic states of QHECs are spin-polarized due to the Zeeman energy and the exchange effect (quantum Hall ferromagnet). Hence in a spin up and down pair of QHEC, the spin and orbital degrees of freedom are quantum mechanically entangled. If one can separate an electron wave packet into two QHECs in such a pair, operations on the orbitals readily change the spin states. For example, spin precession can be realized through the Aharonov-Bohm (AB) interference. Here we report unitary operation of FQs on QHECs by using non-adiabatic inter edge channel tunneling.

Figure 1(a) shows the scheme of the unitary operation. From the right end, an electron wave packet with up spin is injected into QHEC-1 and experiences partial inter-edge tunneling to QHEC-2, which corresponds to a gain of zenith angle in electron. During the travel to the left crossing, a phase difference is given, which corresponds to an azimuth angle rotation. The partition rate to QHEC-1 reflects both zenith and azimuth angles. We realized such quantum interference circuits on semiconductor (AlGaAs/GaAs) two-dimensional system (2DES) and micro-fabricated Schottky gates on it. In Fig.1(b), we illustrate the channels for FQs, the terminals and measurement circuits superposed on an optical micrograph of the sample gate configuration on a 2DES. The first crossing point is realized by Gate SR as a sharp corner, where inter edge tunneling is caused by spin-orbit interaction. The phase difference between QHEC-1 and 2 is developed during the travel along the down edges of Gate SR, C and SL. This process corresponds to the precession of the spin around the zenith axis (z-axis). At the left end of the device, the two QHEC are intermixed again and the total transmission rate to the electrode L reflects both zenith and azimuth angles.

In Fig. 2, we plot the current partition ratio (distribution ratio, D) to drain L as a function of the gate voltage applied to gate C (V_C). The parameter is the gate voltage applied to gate SR (V_{SR}). A large oscillation versus V_C is visible and the amplitude strongly depends on V_{SR}. The oscillation is a consequence of interference in kinetic phases of QHEC-1 and 2, or equivalently precession of electron spin (azimuth angle rotation) [1]. Here V_C is changing the distance between the two channels. The amplitude depends on the zenith angle of the spin, and should be largest making the visibility 100%, when the spin is in xy-plane. Hence from the amplitude we can deduce the zenith angle, *e.g.* 14 degree for V_{SR}= -0.549 V.

From the above, we conclude that unitary operation on electron spin FQ can be done electrically by using spin-polarized QHEC.

Reference
[1] T. Nakajima, K. T. Lin, and S. Komiyama, AIP Conf. Proc. **1566**, 301 (2013).

Authors
T. Shimizu, Y. Hashimoto, A. Endo, T. Nakamura, and S. Katsumoto

Spin Excitations Propagation Dynamics along Skyrmion Strings

Otani Group

Magnetic skyrmions, topological solitons characterized by a two-dimensional swirling spin texture, have recently attracted attention as stable particle-like objects. In three-dimensional systems, the skyrmion can form a string structure by extending in the third dimension, which consists of the uniform stacking of two-dimensional skyrmions along the string direction. Skyrmion strings can be considered as an analog of the vortex line in a superfluid, type-II superconductors, and trapped dilute-gas Bose-Einstein condensates or the cosmic string in the universe. They are all flexible, and some of these strings are proposed to host a resonant oscillation mode propagating through the string path. This implies the possible coherent signal transfer along skyrmion strings, whereas the propagation character of their excitations has rarely been investigated before.

Experimentally, such skyrmion strings appear in a series of bulk magnets with chiral cubic atomic lattice. The examples are metallic B20 or β-Mn-type Co-Zn-Mn alloys and insulating Cu_2OSeO_3, the latter of which is the target of this work. In these materials, the Dzyaloshinskii–Moriya (DM) interaction is the key to the skyrmion formation. For a limited temperature range, these compounds host a hexagonal lattice of skyrmion strings aligned along the static magnetic field (H) direction. This skyrmion crystal (SkX) phase is predicted to host three distinctive magnetic resonance modes (Fig. 1a–c), i.e., the counter-clockwise (CCW) and clockwise (CW) rotational modes both excited by an oscillating magnetic field $H^{\nu} \perp H$, as well as the breathing (B) mode excited by $H^{\nu} /\!/ H$, which have

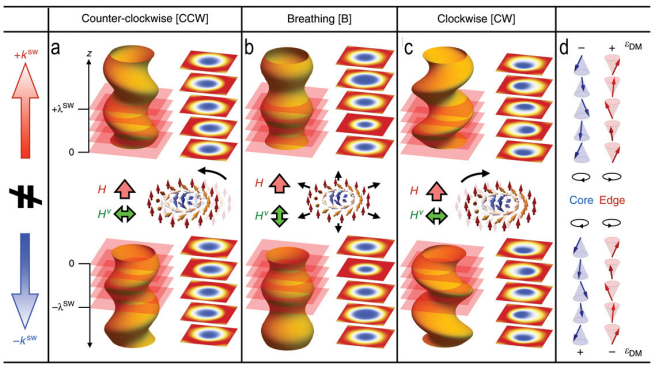

Fig. 1. **a-c** Schematic illustration of CCW, breathing, and CW excitation modes on skyrmion strings. The central part represents the local oscillation manner of skyrmion at the $z = 0$ plane. The upper and lower parts are the snapshot images describing how the spin excitation launched at $z = 0$ propagates on the skyrmion strings, along the $\pm z$ direction parallel and antiparallel to H, respectively. The cross-sectional images describing the size and position of skyrmion at selected z-planes (shown by red layers) are also indicated. **d** The direction of the local magnetic moment at the core and edge position of skyrmion in each z layer. Black rounded arrows denote the sense of local moment precession in the time domain, and ± symbols indicate the sign of local Dzyaloshinskii-Moriya interaction energy gain ϵDM.

recently been identified by magnetic resonance experiments. However, these previous works mostly focused on the character of non-propagating uniform excitations with wave number $k^{SW} = 0$. To understand their propagation character, the employment of a different experimental approach sensitive to the $k^{SW} \neq 0$ regime, as well as the theoretical identification of their dispersion relation, is essential.

In the present study, we experimentally demonstrate the coherent propagation of spin excitations along skyrmion strings for the chiral-lattice magnet Cu_2OSeO_3. We find that the counter-propagating spin excitations show different propagation behavior, and the degree of non-reciprocity, as well as the associated group velocity and decay length, are strongly dependent on the character of the excitation modes. Our theoretically calculated dispersion relations well reproduce these experimental features. The observed decay lengths exceed 50 μm, reflecting the excellent long-range order of the skyrmion-string structure. The present results revealed the peculiar propagation dynamics of skyrmion-string excitations and suggest that skyrmion string can be an excellent medium for magnon transport with unique functionalities. Our combined experimental and theoretical analyses offer a comprehensive account of the propagation dynamics of skyrmion-string excitations and suggest the possibility of unidirectional information transfer along such topologically protected strings.

Reference

[1] S. Seki, M. Garst, J. Waizner, R. Takagi, N. D. Khanh, Y. Okamura, K. Kondou, F. Kagawa, Y. Otani, and Y. Tokura, Nat. Commun. **11**, 256 (2020).

Authors

S. Seki[a,b,c], M. Garst[d], J. Waizner[e], R. Takagi[a,b], N. D. Khanh[b], Y. Okamura[a], K. Kondou[b], F. Kagawa[a,b], Y. Otani and Y. Tokura[a,b]

[a]The University of Tokyo

[b]RIKEN Center for Emergent Matter Science (CEMS)

[c]PRESTO, Japan Science and Technology Agency (JST)

[d]Institut für Theoretische Festkörperphysik, Karlsruher Institut für Technologie

[e]Institut für Theoretische Physik, Universität zu Köln

Creation of Magnetic Skyrmions by Surface Acoustic Waves

Otani Group

Non-collinear and non-coplanar spin textures, such as chiral domain walls and helical or triangular spin structures, bring about diverse functionalities. Among them, magnetic skyrmions, particle-like non-coplanar topological spin structures characterized by a non-zero integer topological charge called the skyrmion number (N_{sk}), have great potential for various spintronic applications, such as energy-saving, non-volatile memory, and non-von Neumann devices. Current pulses can nucleate skyrmion in thin-film samples but require relatively large current densities, which probably causes Joule heating. Moreover, skyrmion creation is localized at a specific position in the film, depending on the sample design. Here, we experimentally demonstrate an approach to skyrmion creation employing surface acoustic waves (SAWs); in asymmetric multilayers of Pt/Co/Ir, propagating SAWs induce skyrmions in a wide area of the magnetic film (Fig. 1a,b). We use multilayer films of Pt/Co/Ir in which the formation of thermodynamically stable skyrmions has already been well-studied in previous

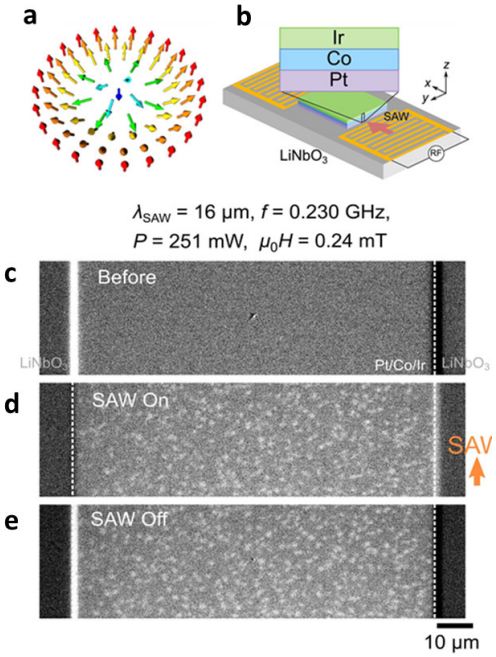

Fig. 1. **a**, Schematic spin configuration of Néel skyrmion. **b**, Schematic illustration of the device structure. Pt/Co/Ir films are deposited on LiNbO3 substrates, and interdigital transducers (IDTs) are fabricated on both sides of a rectangular-shaped Pt/Co/Ir film. Surface acoustic waves (SAWs) are excited by applying radio-frequency (RF) voltage to IDTs. **c-e**, Polar Kerr images before (a), during (b), and after (c) exciting a propagating surface acoustic wave (SAW) with the wavelength (λ_{SAW}) of 16 μm by applying radio-frequency (RF) voltage with the power (P) of 251 mW. The white dashed lines represent the boundaries between Pt/Co/Ir film and LiNbO3 substrate. The orange arrow represents the propagation direction of SAW.

research. All measurements were performed at room temperature, and the magnetic field (H) was applied perpendicular to the film plane. Firstly, we determined, from magnetic images taken before and after the application of SAWs at various H, the magnetic field H_{sk} at which skyrmions begin to appear in the ferromagnetic state without SAWs. The magnetic field evolution of polar Kerr images in a Pt/Co/Ir film with the nominal Co thickness of d_{Co} = 0.55 nm shows that maze domains firstly appear at $\mu_0 H$ = 0.01 mT and transforms to thermodynamically stable skyrmions 3 μm in diameter at 0.21 mT. A further increase in H makes the skyrmions annihilate and leads to the ferromagnetic state at $\mu_0 H$ = 0.31 mT. Here, we note that the size of the observed skyrmions is relatively large, indicating that the dipole-dipole interaction plays an essential role in their stabilization, in addition to the interfacial DMI, and these types of skyrmion are sometimes called a 'skyrmion bubble'.

Figures 1c–e represent the magnetic images before and during excitation by the propagating SAWs. Before exciting with SAWs, we observe no magnetic contrast (Fig. 1c), which indicates that the sample is in the single-domain ferromagnetic state. When the SAW is continuously excited, skyrmions appear (Fig. 1d); skyrmions are nucleated over almost the whole region of a rectangular-shaped Pt/Co/Ir film of width 100 μm and length 400 μm because of the long propagation length of the SAWs. Even after turning off the SAW, most of the skyrmions survive, indicating the emergence of metastable skyrmions (Fig. 1e). The density (n_{sk}) of the nucleated skyrmions in the ferromagnetic state gradually increases with RF power above the threshold of P = 100 mW (Fig. 2a). When H is close to H_{sk}, the number of skyrmions dramatically increases after exciting with SAWs. Besides, when the skyrmions coexist with the ferromagnetic state before exciting with SAWs, that is, $H < H_{sk}$, skyrmions

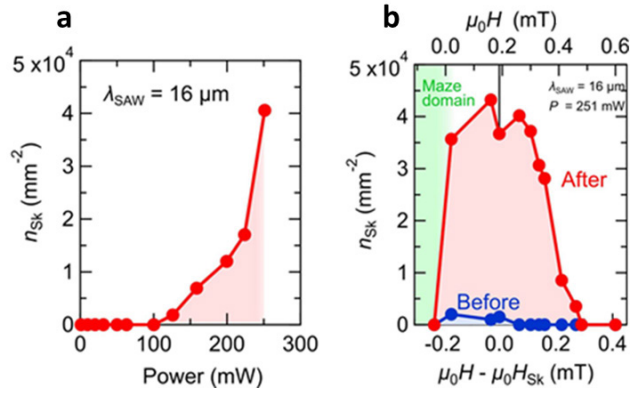

Fig. 2. **a**, Density of skyrmions (n_{sk}) as a function of the power of the RF signal that excites the SAWs. **b**, Magnetic field dependence of n_{sk} before and after exciting a SAW with λ_{SAW} = 16 μm and P = 251 mW.

are also created. The value of n_{sk} after exciting with SAWs is much larger than that before exciting with SAWs (Fig. 2b). In contrast, skyrmions cannot be created in the high field region. This is probably because, in the high field region, the energetically stable ferromagnetic state cannot accommodate skyrmions due to the gain in Zeeman energy, even when SAWs are excited.

Micromagnetic simulations reveal that inhomogeneous torque arising from both SAWs and thermal fluctuations creates magnetic textures, with pair structures consisting of a Néel skyrmion like and an antiskyrmion-like structure. Subsequently, such pairs transform into a Néel skyrmion due to the instability of the antiskyrmion-like structure in a system with interfacial Dzyaloshinskii–Moriya interaction. Our findings provide a tool for efficient manipulation of topological spin objects without heat dissipation and over large areas, given that the propagation length of SAWs is of the order of millimeters.

Reference

[1] T. Yokouchi, S. Sugimoto, B. Rana, S. Seki, N. Ogawa, S. Kasai, and Y. Otani, Nat. Nanotechnol. **15**, 361 (2020).

Authors
T. Yokouchi[a], S. Sugimoto[b], B. Rana[a], S. Seki[a,c,d], N. Ogawa[a,c], S. Kasaia[b,c] and Y. Otani
[a]RIKEN Center for Emergent Matter Science (CEMS)
[b]National Institute for Materials Science (NIMS)
[c]PRESTO, Japan Science and Technology Agency (JST)
[d]The University of Tokyo

Large Magnetic Anisotropy of $L1_0$ Ultrathin Film Grown by Nitrogen-surfactant Epitaxy

Komori Group

For the development of useful magnetic materials, important are uniaxial magnetic anisotropy with high magnetic moment, coercivity, and transition temperature. Moreover, for their wide use, rare-element free materials are strongly required. One of the excellent candidates of such magnetic materials is $L1_0$ FeNi with large uniaxial anisotropy energy, K_u, up to 1.3 MJm^{-3}. While its single crystal cannot be prepared by conventional macroscopic crystal growth, the single-crystal films have been fabricated by layer-by-layer epitaxial growth on Cu(001) and other substrates in a vacuum. The K_u values of the films are, however, lower than the above ideal one. Thus, the magnetic anisotropy perpendicular to the film has not been realized because the in-plane film shape anisotropy is larger than the magnetocrystalline anisotropy. The limitation in the epitaxial films has been attributed to the imperfect atomic layer-by-layer mode in the alternative deposition process of Fe and Ni atoms and the intermixing of the two elements at the interface.

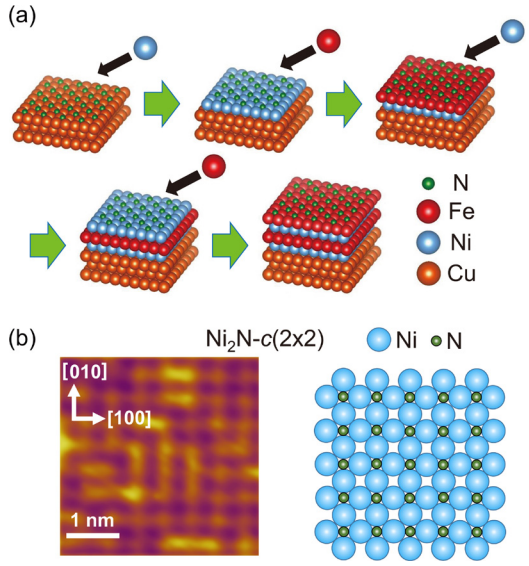

Fig. 1. (a) Schematic model of an FeN/Ni/Fe/Ni film formation process on Cu(001) by surfactant epitaxy using N atoms. First, monolayer c(2x2) Ni_2N is formed on Cu(001) surface as shown in (b) by N adsorption and Ni deposition. Then, 1-ML Fe is deposited below 150 K. After annealing above 300 K, N atoms segregate to the Fe surface and Fe_2N monolayer is formed. Next, on top of this surface, 1-ML Ni is deposited below 150 K. By repeating deposition and annealing, the $L1_0$ FeNi film is prepared. (b) STM image of a Ni_2N atomic layer on Cu(001) (left) and its ball model (right). The 0.5-ML N form c(2x2) structure with 1x1 Ni atoms [1].

We have demonstrated significant improvement of the uniaxial magnetic anisotropy of an $L1_0$ FeNi epitaxial film prepared by surfactant epitaxy of Fe and Ni atomic layers using nitrogen (N) atoms and the deposition on a cooled Cu(001) substrate [1]. The N-surfactant epitaxy, that is, successive and selected segregation of the N atoms to the surface during the alternate Fe and Ni monolayer

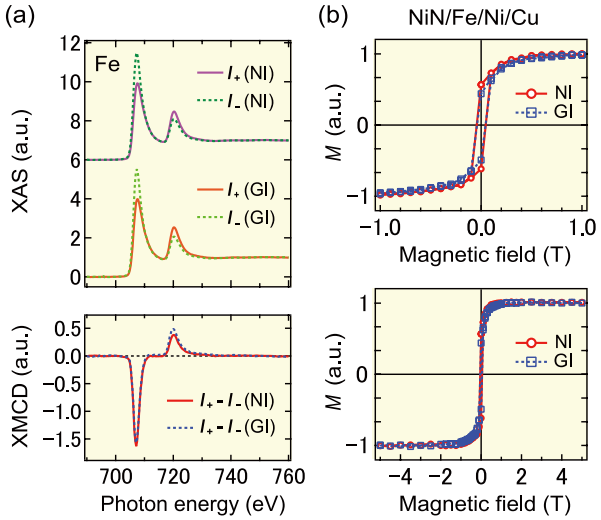

Fig. 2. (a) Fe L-edge XAS (upper) and XMCD (lower) spectra of the NiN/Fe/Ni trilayer for the NI and GI geometries. In the NI (GI) geometry, the magnetic field direction is 0° (55°) off from the surface normal to the [100] direction of the Cu(001) substrate. The XAS intensity was measured with the photon helicity parallel (I_+) and antiparallel (I_-) to the external magnetic field of 5 T at 8 K. (b) Narrow- (upper) and wide- (lower) range Fe magnetization (M) curves of the NiN/Fe/Ni trilayer [1].

(ML) deposition in the present case, suppresses the mixing between Fe and Ni atoms during the deposition and annealing. The schema is given in Fig. 1(a). It was previously shown on the N-adsorbed Cu(001) substrate that N atoms segregate to the surface during the Fe and Co deposition without mixing between the deposited metal and the substrate Cu atoms [2]. This is quite in contrast to the mixing during the deposition of magnetic transition metals on the same substrate [3]. Sharp interface between the atomic layers of Fe and Ni in the film is ensured by the present method. A monatomic layer is grown on the cooled substrate while bilayer islands are formed at room temperature. Satisfactory growth of the $L1_0$ FeNi films up to four monolayers was confirmed after post-annealing process at 430 K by *in-situ* X-ray photoelectron spectroscopy, scanning tunneling microscopy and low energy electron diffraction. Magnetic properties were studied using element-specific soft-X-ray magnetic circular dichroism (XMCD). The value of Fe $L_{2,3}$ XMCD is an order of magnitude larger than that of Ni $L_{2,3}$ XMCD, and thus the Fe monolayer dominates the magnetism of the film. The results of the NiN/Fe/Ni trilayer are shown in Fig. 2. The Fe hysteresis curve measured at 8 K indicates the out-of-plane magnetocrystalline anisotropy is large enough for overcoming the in-plane film shape anisotropy. According to the XMCD sum rule analyses, both Fe and Ni magnetic moments increase with increasing the thickness of the FeNi film.

References

[1] K. Kawaguchi *et al.*, Phys. Rev. Material **4**, 054403 (2020).
[2] D. Sekiba *et al.*, Surf. Sci. **590**, 138 (2005).
[3] H. L. Meyerheim *et al.*, Phys. Rev. B **71**, 035409 (2005).

Authors

K. Kawaguchi,T. Miyamachi, T. Iimori, Y. Takahashi, T. Hattori, T. Yokoyama[a], M. Kotsugi[b], and F. Komori
[a]Institute for Molecular Science
[b]Tokyo University of Science

Enhanced Critical Magnetic Field for Mono-Layer Superconductor by Step Confinement

Hasegawa Group

In a usual superconductor, electrons that have opposite momentum are bound to form a Cooper pair. Under magnetic fields, the pairs lose their stability as the field exerts forces that unbalance the electrons' momenta. Since breaking the pairs costs an energy, however, superconductivity survives up to a certain magnetic field. Enhancing the robustness against magnetic field is technically important, *e.g.* for generating high magnetic fields. In the case of thin films, superconductivity is naturally robust against the in-plane magnetic field because the above-mentioned orbital breaking mechanism is suppressed due to the geometrical limitation. It would therefore be an impact if one finds approaches that make them robust against magnetic fields in other directions. We report here that for a single atomic layer superconductor narrowing terraces by steps improves the tolerance against the out-of-plane magnetic field.

Here as a monolayer (ML) superconductor, we used a Pb-induced reconstructed structure, $\sqrt{3} \times \sqrt{43}$ Pb/Si(111), whose nominal Pb coverage is 1.23 ML. An STM image and a tunneling spectrum taken on the structure at 0.4 K

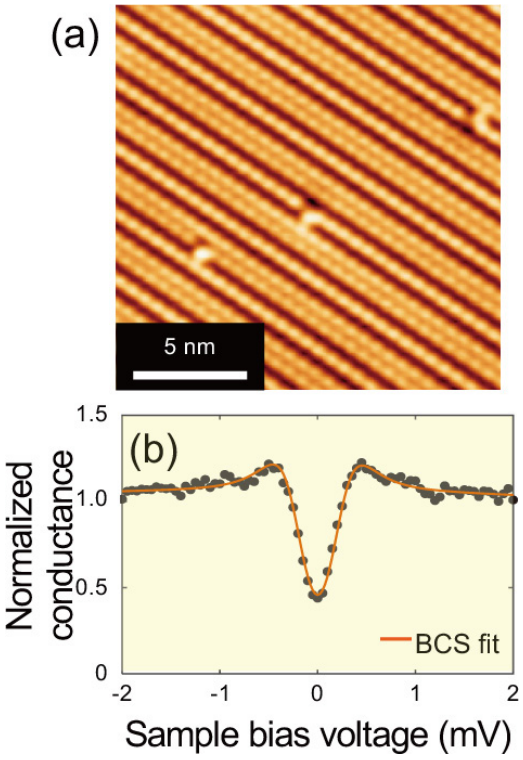

Fig. 1. (a) Atomically resolved image and (b) tunneling conductance spectrum taken on the $\sqrt{3} \times \sqrt{43}$ Pb/Si(111) structure at 0.4 K.

are presented in Fig. 1. From a fitting of the spectrum with the Dynes function, whose curve is drawn with a red line in Fig. 1(b), we found the gap is 0.28 meV. Figures 2(a) show an STM image taken in a wider area (1μm×1μm). The whole surface is covered with the $\sqrt{3} \times \sqrt{43}$ phase including the area close to the step edges. In the same area as Fig. 2(a), we have taken spatial mappings of tunneling conductance at zero bias voltage (ZBC: zero bias conductance), which corresponds to the minimum conductance in the superconducting gap, under various out-of-plane magnetic fields. The amount of the magnetic field ranges from 0 to 400 mT, as shown in Figs. 2(b-h). The ZBC mapping taken under zero field (Fig. 2(b)) demonstrates almost uniform distribution of the deep gaps (low ZBC value) over the entire surface, indicting uniform superconductivity including the area of steps. The steps do not locally break the superconductivity of the ML Pb structure.

When the out-of-plane magnetic fields of 30-100 mT (Figs. 2(c-f)) are applied, several round protrusions of high-ZBC (light green) area are observed. The size of the protrusion is mostly uniform and the diameter is ~100 nm.

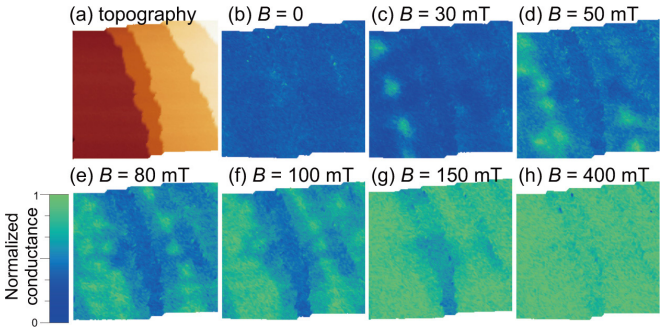

Fig. 2. (a) STM image of $\sqrt{3} \times \sqrt{43}$ Pb/Si(111). (b-h) zero bias conductance mappings in the same field of view with (a) taken under the out-of-plane magnetic field of 0, 30 mT, 50 mT, 80 mT, 100 mT, 150 mT, and 400 mT, respectively.

The number of the protrusions increases with the magnetic field, and the ZBC value at the center of the protrusions is almost same as the saturated ZBC measured at high magnetic fields (*e.g.* 400 mT of Fig. 2(h)). These features lead us to identify these protrusions as a vortex. We noticed in the mapping of 80 and 100 mT (Figs. 2(e, f)) that the vortices are formed only around the middle of wide terraces, apparently repelled from the step edges. In a narrow terrace that is observed vertically around the center of the images, no vortices are found. The apparent repelling of vortices by step edges can be explained with the presence of Josephson vortices at the step edges [1]. A Josephson vortex, formed at a Josephson junction, has an extended core along the junction with suppressed breaking of superconductivity, and therefore appeared dark (blue) along the junction, that is, along the step edges in our case. Since all the vortices including Josephson's exhibit repulsive interaction with each other, the conventional vortices seem repelled from the step edges.

In parallel with the vortex formation, the amount of ZBC behind the vortices gradually increases with the applied magnetic field. At 150 mT (Fig. 2(g)), the vortices almost lose their contrast with the background, which signals saturation of ZBC. Strikingly, in the narrow terrace, ZBC is still low, clearly demonstrating suppression of the superconductivity breaking there. In order to break the superconductivity of the narrow terrace, further increase in the magnetic field was required up to 400 mT (Fig. 2(h)), where all the area reached the saturated ZBC value. The spatially resolved ZBC evolution presented in Fig. 2 clearly demonstrates that the field that makes ZBC saturated, which corresponds to the critical magnetic field, is larger in the narrow terrace than the wide terraces.

From the ZBC evolutions we then investigated how the critical field (H_{c2}) depends on the terrace width w. For the quantitative analysis we first estimated H_{c2} at various sites by measuring the amount of the out-of-plane magnetic field that saturates ZBC, and then dependence of the estimated H_{c2} on terrace width w was investigated. Our analysis indicated a clear crossover around w = 200 nm; for w > 200 nm H_{c2} is constant whereas for w < 200 nm H_{c2} increases steeply with the reduction in w.

According to the Ginzburg-Landau (GL) equation, H_{c2} of low dimensional superconductors whose cross-section is narrower than $2\sqrt{2}\xi$ is given by a formula of $H_{c2} = 4\phi_0/\pi w^2$, where w is the width (the length of short side) of the cross-section and ϕ_0 is magnetic flux quantum. We thus expected our H_{c2} measured on narrow terraces (< 200 nm) are also explained with the formula. However, H_{c2} of our step-confined terraces was found markedly larger than the formula. In order to explain our results, we had to introduce a width-reduction factor w_0 in the formula as $H_{c2} = 4\phi_0/\pi(w\text{-}w_0)2$, and found good agreements with w_0 = 37 nm. The effective reduction in terrace width is probably due to the presence of Josephson vortices; their presence effectively reduces the terrace width through the modification of the boundary condition at the edges. Based on our experimental results we thus conclude that the step confinement makes the superconductor tolerant against the out-of-plane magnetic field more effectively than the geometrical confinement. It should be noted here that since the steps work as a Josephson junction, the superconductivity is not totally disconnected; coherent supercurrent flows across the steps, which is an important aspect for practical applications.

Reference

[1] S. Yoshizawa *et al.*, Phys. Rev. Lett. **113**, 247004 (2014).

Authors

F. Oguro, Y. Sato, K. Asakawa, M. Haze, and Y. Hasegawa

Carrier Transport in Gradient-Doped Photoelectrochemical Electrodes

Lippmaa Group

The interest in developing electrode materials for photoelectrochemical water splitting cells stems from a vision of a sustainable and pollution-free hydrogen-based energy cycle. In essence, the technique is reliant on the development of wide-gap semiconductor materials that are electrochemically and structurally stable over an extended time period, measured in years, in a hydrogen or oxygen evolution reaction under sunlight illumination. Perovskite titanates such as $SrTiO_3$ provide the prerequisite stability in water, but suffer from a variety of intrinsic factors that rate-limit the solar-to-chemical energy conversion process. The primary rate-limiting issues are the non-optimal band gap of 3.2 eV and a short, sub nanosecond photocarrier lifetime. The band gap can be brought down closer to the optimal value of around 2 eV by doping, but adding dopants to the crystal also tends to further shorten the carrier lifetime to picosecond range, negating any possibility of high-efficiency diffusive photocarrier transport from the bulk of the semiconductor to the water interface to drive the water splitting reaction.

We have recently attempted to determine the role of Ti-site dopants on the energy conversion efficiency under ultraviolet band-gap excitation using non-doped and Nb-doped $SrTiO_3$ single crystals (A-D) shown in Fig. 1.

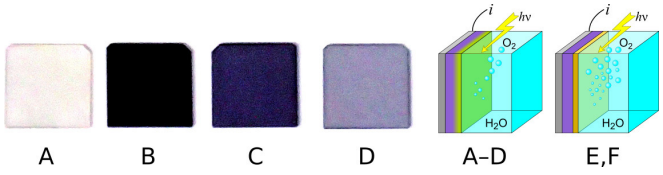

Fig. 1. (A to D) Nb:$SrTiO_3$ single-crystal electrode materials, with doping levels of A:0%, B:1%, C:0.1%, D:0.04%. (A-D) photoelectrochemical cell configuration. Electrode crystal shown in violet, surface depletion layer in yellow. (E,F) Cell configuration for thin film samples consisting of a $SrTiO_3$ film (yellow) on a metallic Nb:$SrTiO_3$ substrate (violet).

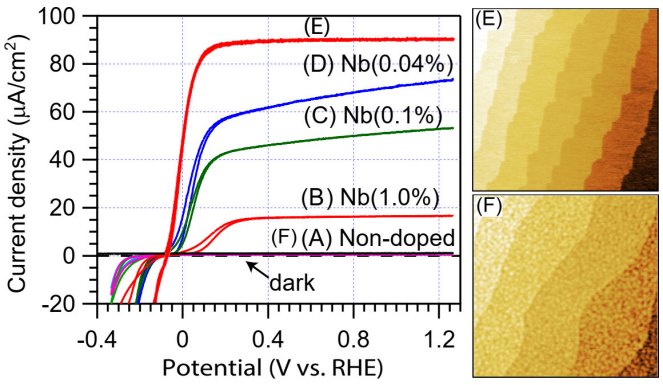

Fig. 2. Illustration of energy conversion efficiency, which is proportional to the cyclic voltammetry current for crystals A to F. The atomic force microscope images for films E and F illustrate the difference in surface morphology related to lower (E) and higher (F) point defect densities in the films.

The corresponding cyclic voltammetry curves are shown in Fig. 2, where the current density is directly proportional to the efficiency of the energy conversion process, i.e., the number of generated gas molecules. The photoresponse of a non-doped 0.5-mm-thick $SrTiO_3$ crystal (A) is zero due to the large resistance of the insulating crystal, which prevents current flow in an electrochemical cell (PEC) illustrated in Fig. 1(A-D). Photoinduced holes in the surface depletion layer of the substrate crystal, marked with a yellow gradient in the PEC diagram in Fig. 1, drive the oxygen evolution reaction but the short lifetime of photocarriers prevents diffusive photoelectron transport through the bulk part of the crystal, stopping the water splitting reaction.

Electron transport becomes possible when bulk conductivity is induced by slight Nb doping of $SrTiO_3$ at the Ti site. As shown in Fig. 2, the efficiency gradually increases as the doping level is reduced from 1% to 0.04% (B to D). Further doping reduction will lead to reduced efficiency due to increasing internal resistance of the substrate crystals.

Improvement of the PEC efficiency can be achieved with a bilayer heterostructure design that combines a non-doped defect-free $SrTiO_3$ crystal in the ~100 nm thick surface depletion region of the electrode with a slightly-doped Nb:$SrTiO_3$ substrate, illustrated in Fig. 1(E,F). Photocarrier recombination losses are minimized and extraction efficiency maximized in the depletion region where the high internal field associated with the surface band bending drives fast carrier transport, whereas bulk doping is used to promote electron transport in the bulk diffusive region of the electrode. Ideally, a continuously varying doping gradient could be used to match the bulk doping level to the width of the surface depletion layer by growing a crystal with a depth-direction gradient of the doping level.

As a simplified demonstration of this concept, we grew a high-crystallinity film with a minimal point defect density and an atomically flat surface morphology (Fig. 2, E) on a highly-doped Nb:$SrTiO_3$ substrate [1]. The importance of defect density control can be seen in a comparison electrode, which was grown at a low temperature and thus contained a high density of point defects (Fig. 2, F). The energy conversion performance of the defect-rich film was, as expected, nearly zero.

This work demonstrates the importance of point defect density control in PEC electrode materials and shows that depth-graded doping control can be a viable strategy for designing efficient hydrogen generation photoelectrochemical electrodes.

Reference
[1] S. Kawasaki, R. Takahashi, and M. Lippmaa, J. Phys. Chem. C, **123**, 15551 (2019).

Authors
S. Kawasaki[a], R. Takahashi, and M. Lippmaa
[a]NIMS

The Roles of Step-Site and Zinc in Surface Chemistry of Formic Acid on Clean and Zn-mModified Cu(111) and Cu(997) Surfaces

Yoshinobu Group

Methanol is of great interest as a source of future hydrogen energy systems, because it is a useful chemical that can produce hydrogen. On the other hand, the synthesis of methanol from CO_2 and H_2 ($CO_2 + 3H_2 \rightarrow CH_3OH + H_2O$) is one of the effective use of CO_2, where the Cu/ZnO catalyst has been used for this reaction. However, the details of reaction mechanism including intermediate species have not been fully elucidated yet. The chemistry of formic acid (HCOOH) on Cu surfaces is important, because the formate species (HCOO) is one of the stable intermediate species in methanol synthesis.

In this study, we systematically investigated the adsorption, desorption and decomposition of formic acid (HCOOH) on Cu(111), Cu(997), Zn-Cu(111) and Zn-Cu(997) using high-resolution X-ray photoelectron spectroscopy (HR-XPS), temperature programmed desorption (TPD) and infrared reflection absorption spectroscopy (IRAS) [1]. On the clean Cu(111) surface, 13% of formic acid molecules adsorbed at 83 K were dissociated to form bidentate formate species by heating at 300 K (Fig. 1a); however, on the Zn-Cu(111) surface, only 4% or less of adsorbed HCOOH were dissociated into the bidentate formate species (Fig. 1b). On the other hand, 13% of adsorbed HCOOH were already dissociated into monodentate formate species on Cu(997)

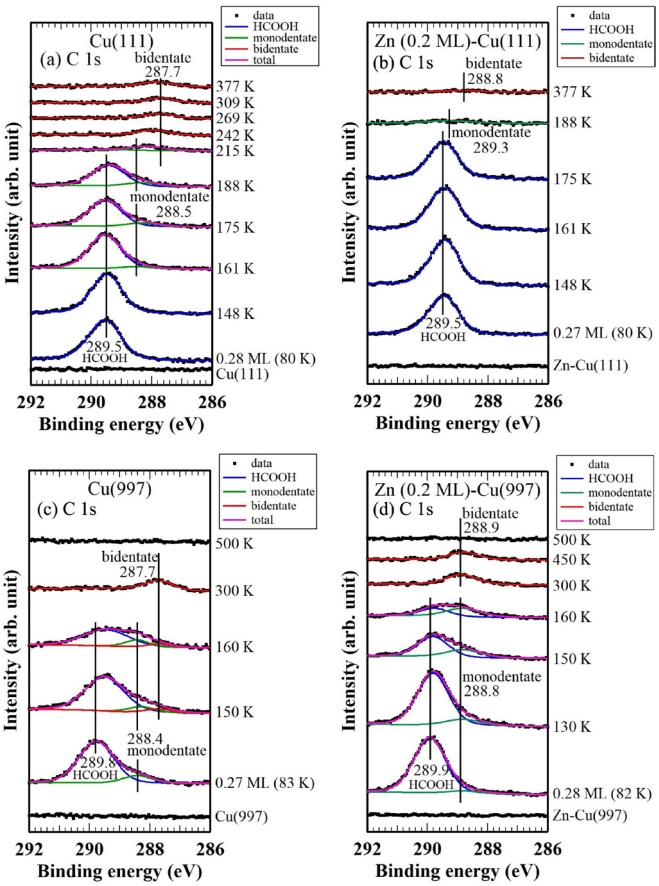

Fig. 1. C 1s XPS spectra of formic acid and formate species as a function of temperature on (a) Cu(111), (b) Zn-Cu(111), (c) Cu(997) and (d) Zn-Cu(997)

even at 83 K and 17% of adsorbed formic acid molecules were transformed to bidentate formate species by heating (Fig.1c). Thus, the stepped Cu surface has higher reactivity for HCOOH dissociation at low temperature. On the Zn-Cu(997) surface, 20% of formic acid became bidentate formate species in contrast to the case with Zn-Cu(111) (Fig. 1d); the Zn deposited Cu step surface shows special activity for adsorption and dissociation of formic acid.

The desorption peak maxima of the formate decomposition products (CO_2 and H_2) on Zn-Cu(997) were shifted to higher temperature than those on Cu(997) in TPD results. Thus, the Zn on Cu surfaces plays an important role in the stabilization of formate species, which probably leads to the decrease in the activation barrier for hydrogenation on the Zn-Cu surface. The bidentate formate species at the Zn-Cu sites can remain after heating at 472 K on Zn-Cu(997); we found that the formate species at Zn-Cu step sites are further stabilized. Therefore, in the real Zn-Cu catalysts that have many step sites, we think that the synergy by the Zn and Cu step site can play a vital role in methanol synthesis.

Reference
[1] Y. Shiozawa, T. Koitaya, K. Mukai, S. Yoshimoto, and J. Yoshinobu, J. Chem. Phys. 152, 044703 (2020).

Author
J. Yoshinobu

The Structural Study on Microbial Rhodopsins and the Characterization of New Microbial Rhodopsin Families

Inoue Group

Rhodopsin is photo-receptive heptahelical transmembrane protein in which a retinal chromophore is covalently bound to a conserved lysine residue in the seventh transmembrane helix (TM7), and animal and microbial rhodopsin families are known so far. Animal rhodopsins are present in animal retina to transfer visual signal to brain and are also related to non-visual light sensing in various tissues. Microbial rhodopsins show diverse functions: light-driven ion pump, light-gated ion channel, phototactic sensor, light-dependent regulation of gene expression and enzyme, and so on. Both types of rhodopsins are being widely used in optogenetics to control various cellular events, such as neural activity, gene expression, dynamic protein localization, and so on, by light.

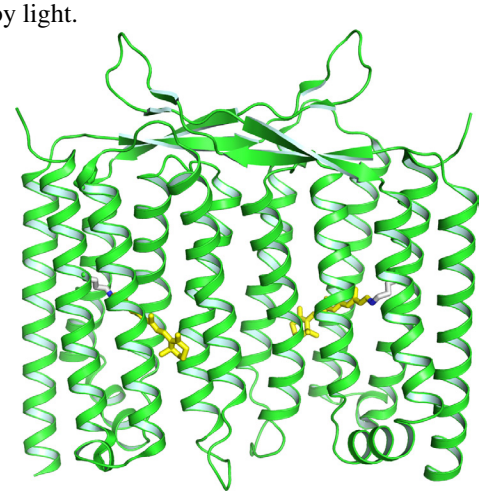

Fig. 1. The x-ray crystallographic structure of HeR

Recently, we discovered the third class of rhodopsin, heliorhodopsin (HeR), which is evolutionally distinct from both of microbial and animal rhodopsins. In 2019, we reported the three-dimensional structure of HeR at atomic level by the x-ray crystallographic analysis (Fig. 1) [1]. It revealed that HeR forms dimers and a fenestration is present near the β-ionone ring of the retinal chromophore. The biochemical experiment suggested that this fenestration is used for the uptake of the retinal chromophore from the environment. This molecular character unique for HeR is considered to be physiologically important for microorganisms having HeR without retinal synthetic genes. Also, the bioinformatic analysis suggested that, while HeR is widely distributed in many gram-positive bacteria, no gram-negative bacteria do not have HeR in their genomes. Because many typical microbial rhodopsins are used by many gram-negative bacteria, the absence of HeR in them is a highly unexpected fact suggesting that the physiological function of HeR would be related to the structure of the cellular membrane of gram-positive bacteria without outer membranes. The study on the ultrafast photoisomerization process of the retinal chromophore in HeR revealed that its isomerization process is similar to those of typical microbial rhodopsins despite of considerably different amino acid residues surrounding the chromophore. A convergent evolution may have occurred in typical microbial rhodopsins and HeR to achieve efficient retinal isomerization with high quantum yields.

The three-dimensional atomic structure of *Gloeobacter* rhodopsin (GR) was solved by the x-ray crystallographic analysis. The electron microscopic observation revealed that GR exists as a pentamer, and the structural detail obtained in our study will provide new insights to understand the mechanism of oligomerization of membrane protein.

A new type of rhodopsin showing unique isomerization process and microbial rhodopsin without retinal binding lysine (Rh-noK) were also identified from bacteria [2]. The former has a new type of amino acid residues in the TM3 consisting of threonine, alanine and threonine called the "TAT motif" at the position where typical proton pumping rhodopsin has the DTD (aspartic acid-threonine-aspartic acid) or DTE (aspartic acid-threonine-glutamic acid) motifs. In the study of Rh-noK, we revealed that ca. 10% of 5,558

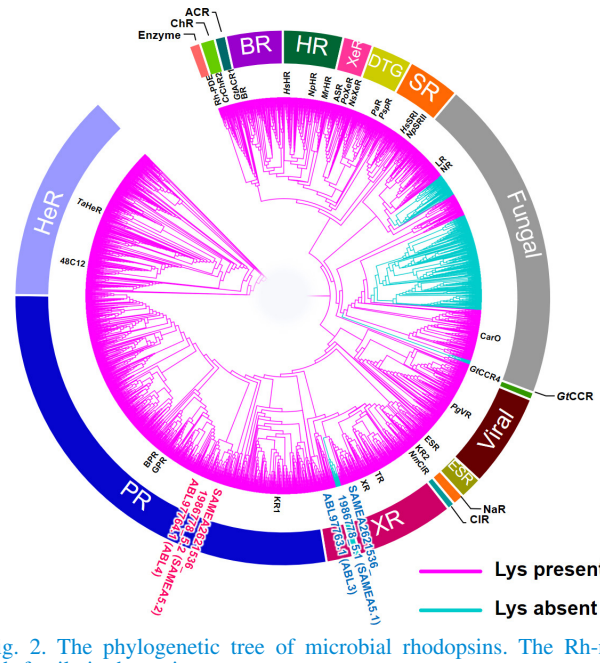

Fig. 2. The phylogenetic tree of microbial rhodopsins. The Rh-noK sub-family is shown in cyan.

microbial rhodopsins do not have the lysine residue in TM7 which typically is used to bind the retinal chromophore by making a covalent Schiff base linkage (Fig. 2). A colored protein was formed by introducing a lysine residue at this position, and, interestingly, additional introduction of an aspartate functioning as a counterion to the protonated retinal Schiff-base recovered the light-driven outward proton pumping function. This suggests that the Rh-noK protein was recently evolved from natural outward proton pumping rhodopsin, and most of structural elements important for the pump function has been retained even after the lack of the retinal binding lysine and counterion aspartate. The physiological roles of TAT rhodopsin and Rh-noK have not been revealed yet, and they will be investigated in the near future.

References
[1] W. Shihoya, K. Inoue *et al*., Nature **574**, 132 (2019).
[2] C. Kataoka, K. Inoue *et al*., J. Phys. Chem. Lett. **10**, 5117 (2019).

Authors
K. Inoue, T. Nagata, and H. Yawo

Electrical Manipulation of a Topological Antiferromagnetic State

Nakatsuji, Otani, and Miwa Groups

Recently, materials with nontrivial band topology have attracted considerable attention due to their novel physical properties. One such example is a Weyl semimetal, in which two non-degenerate bands linearly touch in momentum space, forming gapless Weyl fermions with different chiralities in a time-reversal-symmetry (TRS) or inversion-symmetry breaking state. These touching points or Weyl nodes act as topologically protected, unit-strength monopoles or antimonopoles of underlying Berry curvature such as a large anomalous Hall effect (AHE) and chiral anomaly. The electrical manipulation of these novel properties becomes an important topic for developing new technologies utilizing novel topological state. For this purpose, TRS-breaking or magnetic Weyl semimetals would be suitable owing to their magnetic texture. Moreover, given the prospects of antiferromagnetic (AF) spintronics for realizing high-density devices with ultrafast operation [1], electrical manipulation of an AF Weyl metal is ideal, but have not yet been reported. In this study, we demonstrate the electrical switching of a topological AF state and its detection by AHE at room temperature in a Weyl antiferromagnet Mn_3Sn by using spin-orbit torque (SOT) switching method.

Mn_3Sn has a hexagonal $D0_{19}$ structure with the ABAB-stacking sequence of a (0001)-kagome layer of Mn, and the geometrical frustration leads to a three-sublattice non-collinear AF ordering of Mn spins below the Néel temperature T_N ~ 430 K (Fig. 1(a)) [2]. The magnetic octupole's polarization direction determines the location of Weyl nodes and the associated distribution of the Berry curvature in the momentum space (Fig. 1(b) right). To induce possible SOT switching in Mn_3Sn, we prepared the Mn_3Sn/nonmagnetic metal (NM = Pt, W, Cu) bilayer devices. Figure 2(a) shows the schematic image of the SOT switching in Mn_3Sn/Pt bilayer devices. When an electrical current flows into the Pt layer, a spin polarized current generated by the spin Hall effect of Pt induces the SOT on the Mn_3Sn layer and causes the switching of the polarization direction of the magnetic octupole. The measurement configuration and optical micrograph of the fabricated bilayer Hall bar devices are shown in Fig. 2(b). In our study, we first perform the magnetic field switching of the Hall voltage V_H by using an out-of-plane magnetic field H_z with a read current of 0.2 mA. A clear hysteresis of V_H with the zero-field change of ΔV_H^{field} (= $V_H(+H_z \to 0) - V_H(-H_z \to 0)$) is observed (Fig. 2(c)). To examine the possible SOT switching of

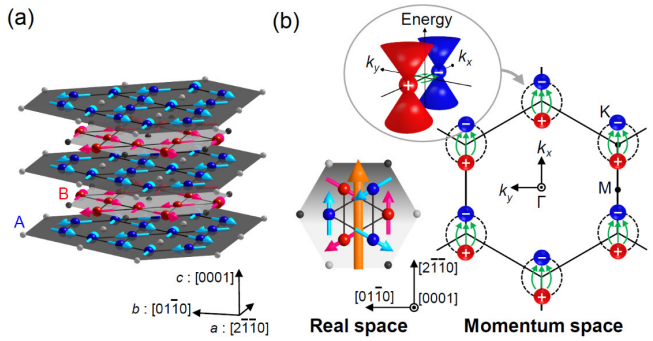

Fig. 1. (a) Mn_3Sn crystal structure and inverse triangular spin (ITS) structure. The large blue and red spheres (small gray and black spheres) represent Mn atoms (Sn atoms) at z = 0 and 1/2, respectively. The Mn magnetic moments (light blue and pink cylindrical arrows) lie within the kagome-layer with the AB-AB stacking sequence and form the ITS structure at room temperature. The spin structure on the kagome bilayers can be viewed as a ferroic ordering of a cluster magnetic octupole. (b) Left: cluster magnetic octupole (orange cylindrical arrow) consisting of the six spins on the kagome bilayer. Right: schematic distribution of the Weyl points near the Fermi energy in the momentum space (k_x-k_y plane at k_z = 0) for the magnetic structure shown in the left-side figure. Red and blue spheres correspond to Weyl nodes, which respectively act as sources (+) and drains (-) of the Berry curvature (green arrows). Inset: three-dimensional schematic picture of a pair of Weyl nodes.

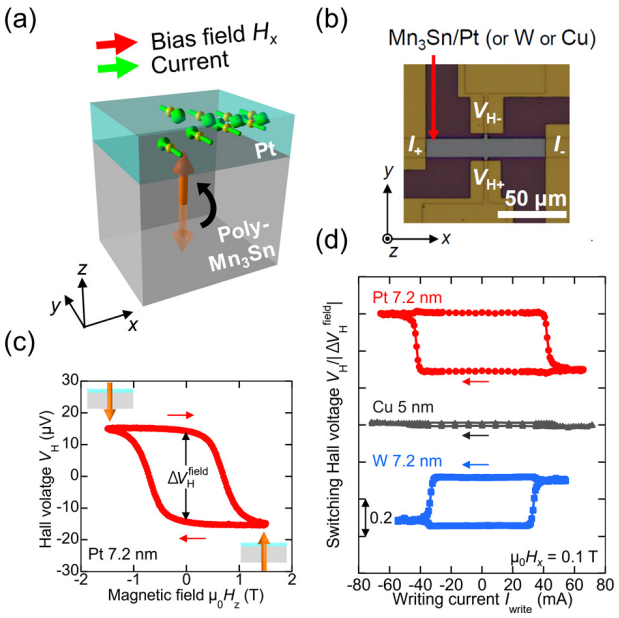

Fig. 2. (a) Schematic image for the spin-orbit torque switching. The spin-polarized current (green cylindrical arrows on yellow spheres) generated in Pt exerts a spin-orbit torque, causing the switching of the polarization axis of the cluster magnetic octupole (orange cylindrical arrow) in the polycrystalline Mn_3Sn under a write current and a bias field along the x-direction. (b) Measurement configuration and optical micrograph of the fabricated Mn_3Sn-nonmagnet bilayer Hall bar devices. (c) Hall voltage V_H vs. magnetic field along the z-direction H_z for the Mn_3Sn/Pt 7.2 nm device at room temperature. Inset: Schematic figures illustrating the direction of the cluster magnetic octupole. (d) Hall voltage V_H vs. write current I_{write} for the Pt 7.2 nm, Cu 5 nm, and W 7.2 nm devices at room temperature. The Hall voltage is normalized by the zero-field Hall voltage $|\Delta V_H^{field}|$ in the magnetic field dependence for each sample.

Mn_3Sn, we pass a 100 ms write-pulse current I_{write} along the x-direction; then, we wait for 600 ms after the pulse current and measure V_H with a 0.2 mA read current. Fig. 2(d) shows V_H as a function of I_{write} in Pt, W, and Cu devices. For the NM = Pt (spin Hall angle $\theta_{SH} > 0$), a clear negative (positive) jump appeared in the Hall voltage under a positive (negative) current larger than a critical threshold write-current I_c with a bias field H_x along the current direction x. The magnitude of the jump reaches ~30 % of the total Hall voltage change $|\Delta V_H^{field}|$ in the field sweep measurements. To confirm that this switching of V_H is related to the SOT from the spin Hall effect in the NM layer, we prepared NM = W ($\theta_{SH} < 0$) and Cu ($\theta_{SH} \sim 0$) instead of Pt. For NM = W, the switching polarity is opposite to the Pt one, while for NM = Cu, there is almost no hysteresis with the electrical current cycle. The difference in switching polarity between Pt and W devices and the absence of switching in Cu devices cannot be accounted for by the Oersted field generated by the electrical current but agree well with the sign of θ_{SH} of the NM layer. These results demonstrate that SOT from the NM layer induces the perpendicular switching of the AF domain and thus manipulates the direction of Weyl nodes.

In recent years, utilizing antiferromagnets in spintronics devices have attracted significant attention as its vanishing small stray fields and much faster spin dynamics than ferromagnets [1]. Our electrical switching measurement of AF Weyl metals is made by using the same protocol as the one used for ferromagnetic metals [3,4]. Moreover, the switching or critical write current density J_c in the NM layer is found reasonably small. It is estimated to be 2×10^{11} A/m^2 for 7.2 nm thick Pt and 5×10^{10} A/m^2 for 7.2 nm thick W devices, which are smaller than the original values reported for the first observations of the electrical switching in the NM/FM devices ($J_c \sim 10^{12}$ A/m^2) [3,4]. These results indicate that topological antiferromagnets may replace ferromagnets in spintronics devices.

In summary, we demonstrated the electrical switching of Weyl antiferromagnets Mn_3Sn by using Mn_3Sn/NM bilayer devices. Our findings indicate that SOT switching is a useful tool for electrically manipulating the distribution of Weyl points and Berry curvature in momentum space. These observations may lead to further scientific and technological advances in topological magnetism and antiferromagnetic spintronics [5].

References

[1] T. Jungwirth *et al*., Nat. Nanotechnol. **11**, 231 (2016).
[2] S. Nakatsuji, N. Kiyohara, and T. Higo. Nature **527**, 212 (2015).
[3] I. M. Miron *et al*., Nature **476**, 189 (2011).
[4] L. Liu *et al*., Science **336**, 555 (2012).
[5] H. Tsai, T. Higo, K. Kondou, T. Nomoto, A. Sakai, A. Kobayashi, T. Nakano, K. Yakushiji, R. Arita, S. Miwa, Y. Otani, and S. Nakatsuji, Nature **580**, 608 (2020).

Authors

H. Tsai, T. Higo, K. Kondou[a], T. Nomoto[b], A. Sakai, A. Kobayashi, T. Nakano[c], K. Yakushiji[c], R. Arita[a], S. Miwa, Y. Otani, and S. Nakatsuji

[a]RIKEN CEMS
[b]University of Tokyo
[c]AIST

Large Transverse Thermoelectric Effect in Iron-Based Binary Ferromagnets

Nakatsuji and Miwa Groups

Thermoelectricity, conversion of heat current into electric energy, provides key technology for versatile energy harvesting and heat current sensors. To date, the technology has relied on the longitudinal thermoelectric response known as the Seebeck effect. Its transverse counterpart in ferromagnets, the anomalous Nernst effect (ANE), has gained significant attention, as it has a number of potential benefits [1,2]. For example, the transverse geometry of the Nernst effect enables the efficient, large area and flexible coverage of a curved heat source (Fig. 1(a)). Moreover, the transverse geometry is hypothetically better suited for thermoelectric conversion, as the Ettingshausen heat current should support the Nernst voltage while the Peltier heat current may suppress the Seebeck voltage [3]. However, the anomalous Nernst effect is too small compared to the Seebeck effect for any thermoelectric application. Thus, it is essential to design a new class of materials that exhibit a large ANE at zero magnetic field.

To find candidate compounds efficiently, we carried out a high-throughput calculation to screen materials without synthesizing them first. Here we found two iron-based cubic compounds Fe_3X (where X is Ga or Al) as materials suitable for designing such low-cost, flexible thermoelectric devices, reaching about 6 μVK^{-1} and 4 μVK^{-1} at room temperature, respectively, close to the highest value reported so far. Our successful fabrication of epitaxial Fe_3Ga and Fe_3Al thin films enables us to obtain a large ANE of about 4 μVK^{-1} and 2 μVK^{-1} at room temperature using an in-plane temperature gradient. Moreover, these Fe_3Ga and Fe_3Al films have in-plane magnetization with a coercivity B_C of about 40 Oe and 20 Oe, respectively, and exhibit a spontaneous ANE at zero field (Fig. 1(b)) for the out-of-plane temperature gradient. These features enable us to design a much simpler thermoelectric device than the conventional Seebeck analogues.

The comparison between experiment and theory indicates that the Fermi energy tuning to the nodal web is the key for the substantial enhancement in the transverse thermoelectric coefficient, reaching a value of about 5 AK^{-1}m^{-1} with logarithmic temperature dependence. Figure 2(a) shows a schematic of the nodal web, a flat band structure made of interconnected nodal lines. The Berry curvature

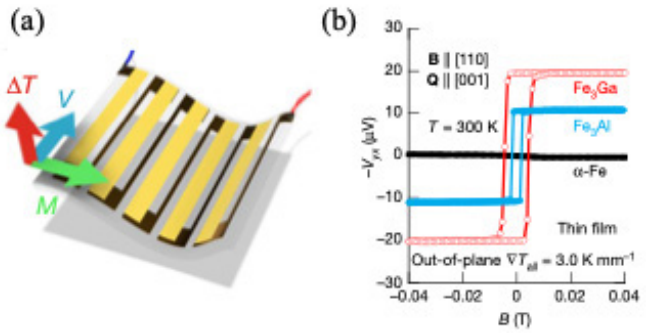

Fig. 1. (a) Thermopiles based on the ANE. V, M, and ΔT is the voltage, magnetization, and temperature difference, respectively. (b) Magnetic field dependence of the Nernst voltage $-V_{yx}$ for the thin films of Fe_3Ga, Fe_3Al and α-Fe. The temperature gradient in the sample (MgO substrate/Fe_3Ga, Fe_3Al, or α-Fe /MgO), ∇T_{all}, is monitored to be 3.0 Kmm^{-1}. The temperature gradient in the Fe_3Ga (Fe_3Al) layer is estimated to be $\nabla T \approx 0.86$ K mm^{-1} (1.0 K mm^{-1}).

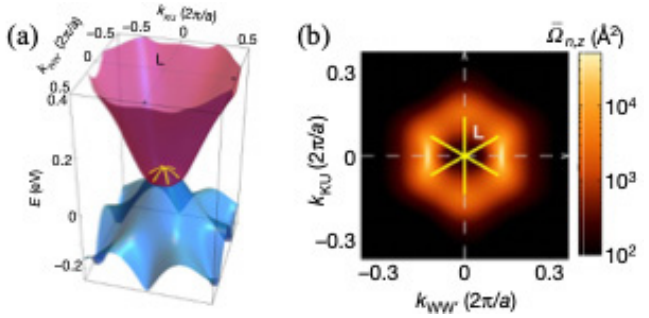

Fig. 2. (a) Energy dispersion of the conduction band (red) and the valence band (blue) around the L point on the BZ boundary for Fe_3Ga. The nodal web is made of nodal lines, shown by the yellow lines (the same as in Fig. 2(b)), along which the flat portions of the conduction and the valence bands touch around the L point. (b) Contour plot of the Berry curvature $\Omega_{n,z}$ of the lower-energy band n around the L point and nodal lines. The z direction is along [001] parallel to the magnetization.

is particularly enhanced at the momenta connecting the edge of the nodal web around the L point on the Brillouin zone boundary, extending over a quasi-2D area spanned by the web (Fig. 2(b)). These results suggest that the strongly enhanced Berry curvature occurs near the momenta originally belonging to the flat nodal web, such as the one around the L point.

Our discovery of the significant spontaneous transverse thermoelectric effects indicates that two iron-based compounds, Fe_3Ga and Fe_3Al, should be suitable for designing low-cost, flexible thermos electric generator by using their thin-film form. It is vital to enhance the coercivity further to achieve stable performance in daily use. Finally, it would be an interesting future direction to look for an enhanced output by combining the ANE with the spin Seebeck effect, both of which occur in the same transverse geometry [4].

References

[1] A. Sakai *et al*., Nat. Phys. **14**, 1119 (2018).
[2] M. Ikhlas, T. Tomita *et al*., Nat. Phys. **13**, 1085 (2017).
[3] M. Mizuguchi and S. Nakatsuji, Sci. Technol. Adv. Mater. **20**, 262 (2019).
[4] A. Sakai *et al*., Nature **581**, 53 (2020).

Authors

A. Sakai, S. Minami[a], T. Koretsune[b], T. Chen, T. Higo, Y. Wang, T. Nomoto[c], M. Hirayama[d], S. Miwa, D. Nishio-Hamane, F. Ishii[a], R. Arita[c,d], and S. Nakatsuji
[a]Kanazawa University
[b]Tohoku University
[c]The University of Tokyo
[d]RIKEN CEMS

Strain-Induced Magnetic Weyl Semimetal in an Epitaxial Thin Film of a Luttinger Semimetal

Nakatsuji, Lippmaa, Katsumoto, and Kindo Groups

Strong electronic correlations serve as a central thread of highly unusual behaviors in quantum materials, ranging from metal-insulator transitions to unconventional superconductivity. The interplay of correlated electron physics with recently discovered novel topological phases establishes a new, fascinating research direction that awaits a full exploration. A vital example of this kind is the magnetic Weyl semimetal (WSM), in which the strongly enhanced Berry curvature inherent to the linearly dispersing crossing points between two electronic bands (i.e., the Weyl points) allows for the emergence of surprisingly large anomalous transport effects even in antiferromagnets or spin-liquid candidates. While the WSM is earlier identified experimentally in nonmagnetic materials with breaking inversion symmetry [1,2], the search for magnetic WSM states in strongly correlated systems remains challenging yet of great importance, due to their excellent tunability and appealing potential for innovative technological applications.

The earliest predicted magnetic WSM is the family of pyrochlore iridates $R_2Ir_2O_7$ (where R is a lanthanoid or yttrium) [3], a 5*d* electron system featuring noncoplanar spin configurations in both 5*d* and 4*f* electron sectors. The 5*d* series provides an ideal ground for realizing exotic topological phases, owing to the comparable strength of the spin-orbit interaction relative to the Coulomb repulsion, allowing the correlation physics to play a critical role. Indeed, recent experiments identified $Pr_2Ir_2O_7$, the metallic end-member of the $R_2Ir_2O_7$ family, as a Luttinger semimetal comprising quadratic band touching of doubly degenerate valence and conduction bands at the Brillouin zone center Γ near the Fermi level E_F (Fig. 1a) [4]. Lattice strain or magnetic field tuning of the Luttinger semimetal may engender a rich topological phase diagram, and is considered a promising route towards realization of a magnetic WSM [5,6].

Recent studies on $Pr_2Ir_2O_7$ have focused on its bulk properties, yet the difficulties of applying uniaxial strain on bulk single crystals leave the magnetic WSM shrouded in mystery. In contrast, thin films allow for control over the crystal growth orientation and lattice deformation via compressive or tensile strain imposed by epitaxial lattice mismatch with a substrate. Here, we report the transport properties of our epitaxial $Pr_2Ir_2O_7$ thin films, which provide firm evidence for a magnetic WSM state induced by the tensile strain along the surface normal [111] direction [7].

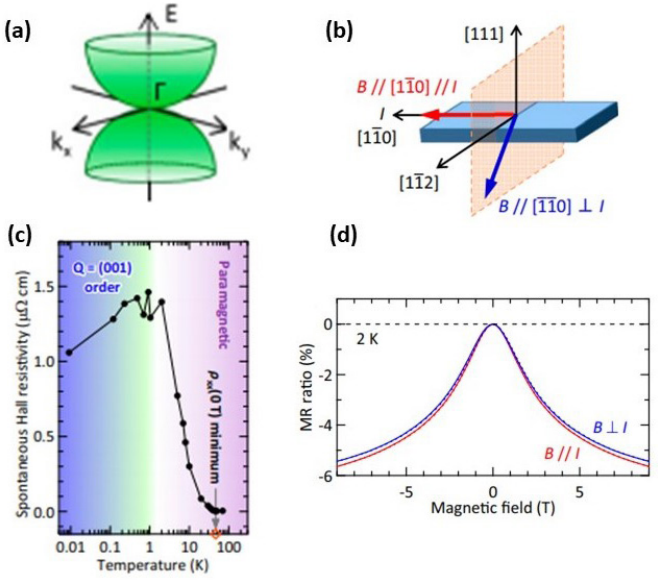

Fig. 1. (a) Band structure of a Luttinger semimetal consisting of quadratic band touching of 5d electrons at the Γ point near EF (b) Schematic for experimental configurations of magnetotransport measurements. (c) Temperature dependence of the spontaneous Hall resistivity. (d) Magnetoresistance curves as a function of the magnetic field B measured at 2 K for $B \parallel I$ and $B \perp I$ configurations. The solid and dotted lines are up and down sweeps of B, respectively. The difference between the two curves arises from the chiral anomaly and indicates that the film is in the Weyl semimetal state.

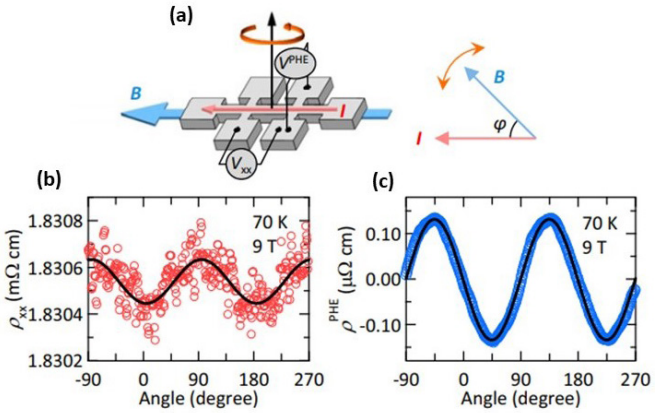

Fig. 2. (a) Schematic for the experimental configuration of the planar Hall effect measurements. (b) and (c) Angle dependence of longitudinal and planar Hall resistivities, respectively, obtained at 70K and 9T

Using strained $Pr_2Ir_2O_7$ thin films, we observed a zero-field Hall effect persisting up to about 50K without detectable spontaneous magnetization (Fig.1c). This onset temperature of the spontaneous Hall effect is much higher than the value (~ 1.5K) observed in bulk single crystals and is nearly two orders of magnitude higher than the exchange coupling (J ~ 0.7K) of Pr 4*f* moments [8], indicating the breaking of time-reversal symmetry induced by the magnetic order of Ir 5*d* electrons. Thus, the condition for realizing a magnetic WSM state is fulfilled in the strained thin film. Moreover, we identified a negative contribution to the magnetoresistance specific to the chiral anomaly (Fig. 1 b and d) and the planar Hall effect (Fig. 2); both phenomena are considered the fingerprints of Weyl points lying close to E_F [9, 10, 11].

In summary, we succeeded in synthesizing epitaxial thin films of $Pr_2Ir_2O_7$ and revealed key transport signatures of the WSM under strain tuning. The discovery of strain-induced magnetic Weyl semimetal state in pyrochlore iridates thin films paves a new avenue to explore topological phases in strongly correlated materials.

References
[1] B. Q. Lv *et al.*, Phys. Rev. X **5**, 031013 (2015).
[2] S.-Y. Xu *et al.*, Science **349**, 613 (2015).
[3] X. Wan *et al.*, Phys. Rev. B **83**, 205101 (2011).
[4] B. Cheng, T. Ohtsuki *et al.*, Nat. Commun. **8**, 2097 (2017).
[5] E.-G. Moon *et al.*, Phys. Rev. Lett. **111**, 206401 (2013).
[6] T. Kondo *et al.*, Nat. Commun. **6**, 10042 (2015).
[7] T. Ohtsuki *et al.*, Proc. Natl. Acad. Sci. U.S.A. **116**, 8803 (2019).
[8] Y. Machida *et al.*, Nature **463**, 210 (2010).
[9] D. T. Son and B. Z. Spivak, Phys. Rev. B **88**, 104412 (2013).
[10] A. A. Burkov, Phys. Rev. B **96**, 041110(R) (2017).
[11] S. Nandy *et al.*, Phys. Rev. Lett. **119**, 176804 (2017).

Authors
T. Ohtsuki, Z. Tian, A. Endo, M. Halim, S. Katsumoto, Y. Kohama, K. Kindo, M. Lippmaa, and S. Nakatsuji

Evidence for the Quadrupolar Kondo Effect in the Heavy Fermion Superconductor PrV_2Al_{20}

Nakatsuji Group

The non-Fermi liquid (NFL) phase holds abiding fascination owing to its prime connections with unconventional superconductivity and other intriguing emergent quantum states in itinerant electron systems. Magnetic heavy-fermion metals offer some prototypical examples of the NFL as a

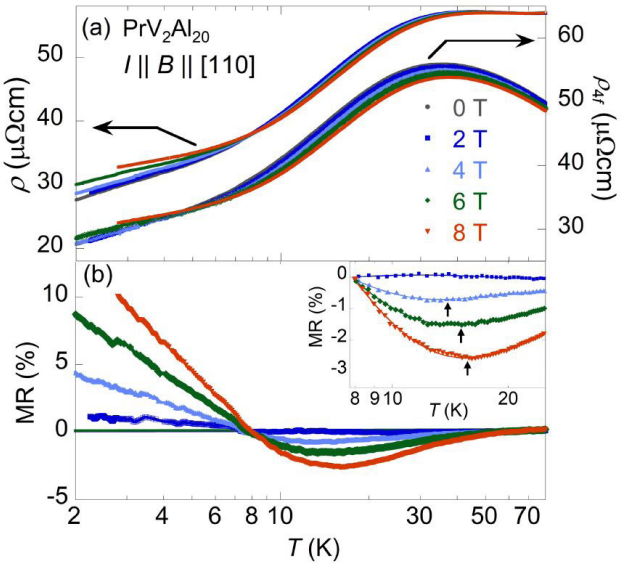

Fig. 1. (a) Temperature dependence of the electric resistivity (left axis) and 4*f*-electron contribution (right axis) of PrV_2Al_{20} under various magnetic fields along [110]. (b) Temperature dependence of the longitudinal magnetoresistance MR of PrV_2Al_{20}.

result of the competing interplay between the magnetic Kondo effect and the Ruderman-Kittle-Kasuya-Yosida (RKKY) interaction among local dipolar moments. Such NFL often appears at the boundary of magnetic instability and is attributed to quantum criticality.

Heavy fermion metals hosting multipolar local moments entail a new route to exotic spin-orbital entangled quantum phases. In the case of quadrupolar systems, the conventional Kondo effect is replaced by a two-channel Kondo mechanism, known as the quadrupolar Kondo effect. Here Kondo entanglement takes place between the quadrupolar moments of f-electrons and the orbital fluctuations of the conduction electrons, while the conduction electron spins offer two separated scattering channels. This effect is considered a key mechanism behind the orbital-driven NFL behavior and quantum critical phenomena. The heavy fermion superconductor PrV_2Al_{20} possesses a nonmagnetic ground-state doublet, featuring both electric quadrupoles

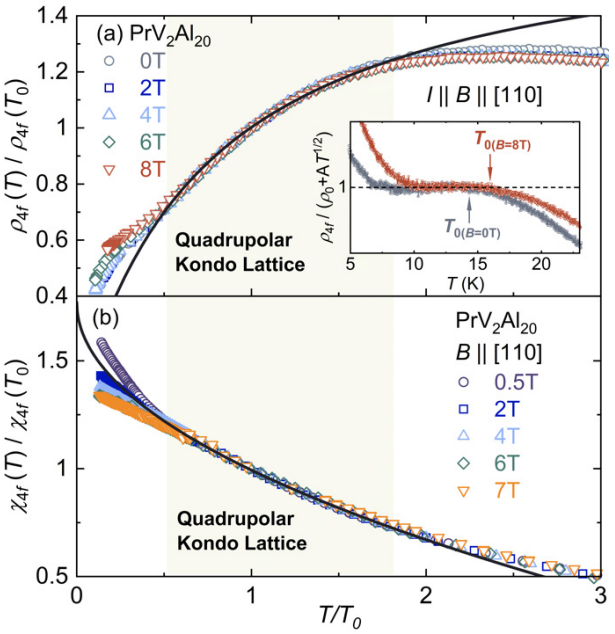

Fig. 2. Universal scaling behavior of (a) the 4*f*-electron contribution to the resistivity and of (b) the magnetic susceptibility measured under a [110] magnetic field.

and magnetic octupoles. It exhibits novel NFL behavior above the antiferroquadrupolar ordering transition at ambient pressure, with ~ $\sqrt{T}$ dependent resistivity and ~ $-\sqrt{T}$ magnetic susceptibility. The relation of this NFL phase with the quadrupolar Kondo effect is yet to be explored.

We report a comprehensive study of the NFL phenomena in PrV_2Al_{20} single crystals based on magnetoresistance (MR), magnetic susceptibility, and specific heat measurements obtained under a [110] magnetic field. Upon entering the NFL regime, we observed a universal scaling behavior expected for the quadrupolar Kondo lattice, which reveals the vital role of the quadrupolar Kondo effect in shaping the NFL phase of PrV_2Al_{20}. Deviations from this scaling relation occur below about 8 K, accompanied by a negative MR and a power-law divergent specific heat. Such behavior signifies the emergence of an anomalous low-temperature state, which is likely driven by heavy-fermion coherence in the quadrupolar Kondo lattice or critical quantum fluctuations of multipolar moments.

References
[1] P. Gegenwart, Q. Si, and F. Steglich, Nat. Phys. **4**, 186 (2008).
[2] D. L. Cox and A. Zawadowski, Adv. Phys. **47**, 599 (1998).
[3] A. Sakai and S. Nakatsuji, J. Phys. Soc. Jpn. **80**, 063701 (2011).
[4] M. Fu *et al*., J. Phys. Soc. Jpn. **89**, 013704 (2020).

Authors
M. Fu, A. Sakai, N. Sogabe, M. Tsujimoto, Y. Matsumotoa, and S. Nakatsuji
[a]Max Planck Institute for Solid State Research

Orbital-Driven Giant Anisotropic Magnetoresistance in the Quadrupolar Heavy Fermion Superconductor PrV_2Al_{20}

Nakatsuji and Sakakibara Groups

The quest for a mechanism that realizes significant transport anomalies in non-ferromagnetic materials may spark a breakthrough in developing ultrafast and energy-efficient memory devices [1,2]. An example of such transport anomaly is anisotropic magnetoresistance (AMR), defined as the difference between the resistance with current applied parallel and perpendicular to the ordered spin direction. To date, however, the AMR effect found in antiferromagnetic materials is limited to a small value of 1% - 2% [3,4]. Rearrangement of electron orbitals may hold the key to further enhancing the AMR in non-ferromagnetic systems, as it should generate anisotropy in the electronic band structure, thereby inducing dramatic effects on the transport properties. A promising discovery along this line is the strongly anisotropic magnetoresistance appearing within the nematic order phase in iron-based superconductors.

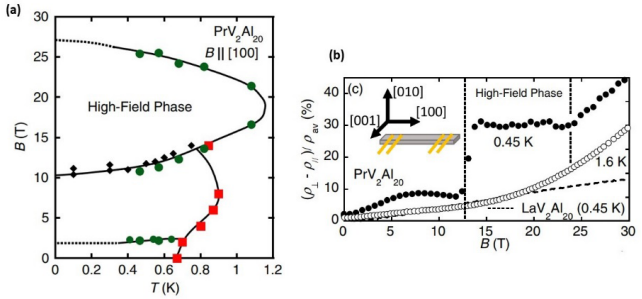

Fig. 1. (a) Temperature-magnetic field (T-B) phase diagram for a [100] magnetic field obtained from the magnetoresistance data. (b) The anisotropic magnetoresistance ratio as a function of magnetic field measured at 0.45K and 1.6K

Here, we focus on a cubic heavy fermion compound PrV_2Al_{20}. A unique feature of this material is its nonmagnetic Γ_3 ground-state doublet, in which the magnetic dipole moment is absent, whereas the quadrupole and octupole moments are active [5], offering an ideal stage for investigating transport phenomena driven solely by electron orbitals. The strong hybridization of these multipolar moments with conduction electrons leads to a rich phase diagram involving a two-stage multipolar order below 0.6–0.7K, non-Fermi-liquid behavior driven by multipolar Kondo effect, and heavy-fermion superconductivity below about 0.05K at ambient pressure [6]. Under a [100] magnetic field, earlier magnetization measurements revealed a high-field phase lying between ~11 – 24T below about 1K [7] (Fig. 1a). This high-field phase is likely the result of rearrangement of the quadrupole moments and therefore is a promising place to explore anisotropic transport properties.

We carried out magnetoresistance measurements under high magnetic fields up to 31.4T at the National High Magnetic Field Laboratory, Tallahassee, USA [8]. Under a [100] magnetic field, we found that, on entering the high-field phase at about 12 T, the rearrangement of quadrupolar moments yields a sharp jump in the magnetoresistance (ΔMR~100%), with a substantial AMR effect of about 30% (Fig. 1b). This feature signifies a Fermi surface reconstruction within the high-field quadrupolar ordered phase, owing to the strong hybridization between the local quadrupolar moment and the conduction electrons. This giant anisotropic magnetoresistance induced by quadrupole rearrangement may form the basis of conceptually new memories and information storage using multipolar states.

References
[1] S. Nakatsuji, N. Kiyohara, and T. Higo, Nature **527**, 212 (2015).
[2] T. Jungwirth *et al*., Nat. Nanotechnol. **11**, 231 (2016).
[3] D. Kriegner *et al*., Nat. Commun. **7**, 11623 (2016).
[4] X. Marti *et al*., Nat. Mater. **13**, 367 (2014).
[5] A. Sakai and S. Nakatsuji, J. Phys. Soc. Jpn. **80**, 063701 (2011).
[6] M. Tsujimoto *et al*., Phys. Rev. Lett. **113**, 267001 (2014).
[7] Y. Shimura *et al*., J. Phys. Soc. Jpn. **82**, 043705 (2013).
[8] Y. Shimura *et al*., Phys. Rev. Lett. **122**, 256601 (2019).

Authors
Y. Shimura[a], Q. Zhang[b], B. Zeng[b], D. Rhodes[b], R. Schönemann[b], M. Tsujimoto, Y. Matsumoto[c], A. Sakai, T. Sakakibara, K. Araki[d], W. Zheng[b], Q. Zhou[b], L. Balicas[b], and S. Nakatsuji
[a]Hiroshima University
[b]National High Magnetic Field Laboratory
[c]Max Planck Institute for Solid State Research
[d]National Defense Academy

Magnetic Field Induced Quantum Phases in a Tensor Network Study of Kitaev Magnets

Kawashima Group

Tensor network (TN) is a useful concept in various fields, not only in the condensed matter theory, but also in data science and machine learning. Even in the condensed matter theory alone, the application of the TN concept is multi-fold. In variational principles calculation, the TN is used as a new type of variational wave function. In the real-space renormalization group (RG) theory, it serves as a natural representation of a renormalized system. In the pure mathematical physics, it is used as a new language for discussing the

topological nature of the quantum states.

In our previous study [Lee, Kaneko, Okubo and Kawashima: Phys. Rev. Lett. **123**, 087203 (2019)], we studied the Kitaev model by the TN representation. We proposed a new wave function that is extremely simple in the TN representation but still shares many essential properties with the ground state of the Kitaev model, such as the quasi-long-range correlation, the short-range magnetic correlation, the flux-free property, the Z_2 gauge structure, and the 2D Ising universality. We call this state the "loop gas state" because of its mathematical equivalence to the loop gas model, one of the standard and solvable statistical physical models. We showed that the loop gas state is adiabatically connected to the ground state of the Kitaev model, indicating a similar role to the AKLT state for the S = 1 AFH chain.

We then extended our method to several other models: S = 1 Kitaev model, and Kitaev-Gamma model. In this study, we studied field-induced quantum phases in the theoretical model of a real candidate material of Kitaev magnets, i.e., α-$RuCl_3$. For this compound, there was an experimental discovery of the half quantized thermal Hall conductivity, which initiated a series of theoretical investigations aiming at finding a concrete connection between the observed quantum phenomena and the theoretical developments of the Kitaev spin liquid. Our TN calculation suggested that a field-induced phase appears between the low field zig-zag magnetic order and the high field polarized state. We found that the chiral Kitaev spin liquid occupies an area in the phase diagram, smaller than predicted by other groups.

Specifically, we studied the K-Γ-Γ' model on the honeycomb lattice represented by the following Hamiltonian,

$$H = \sum_{ij} H_{ij}^{\alpha_{ij}}$$

$$H_{ij}^{\alpha} = \frac{\mathbf{h}}{3}\cdot(\mathbf{S}_i + \mathbf{S}_j) + \mathbf{S}_i^{\mathrm{T}} G^{\alpha} \mathbf{S}j$$

where α_{ij} = x,y,z depending on the direction of the bond (ij). The magnetic field is along the [111] direction. The matrix G_α characterizes the two-body anisotropic interaction, e.g, for α = z,

$$G^z \equiv \begin{pmatrix} 0 & \Gamma & \Gamma' \\ \Gamma & 0 & \Gamma' \\ \Gamma' & \Gamma' & K \end{pmatrix}$$

The matrices for other directions are defined similarly.

In Fig. 1, the obtained phase diagram is presented. The KSL ground state survives only in a small corner of the phase diagram. It disagrees with the previous results obtained by 24-site exact diagonalization and DMRG studies, which suggested a largely extended KSL phase. The discrepancy

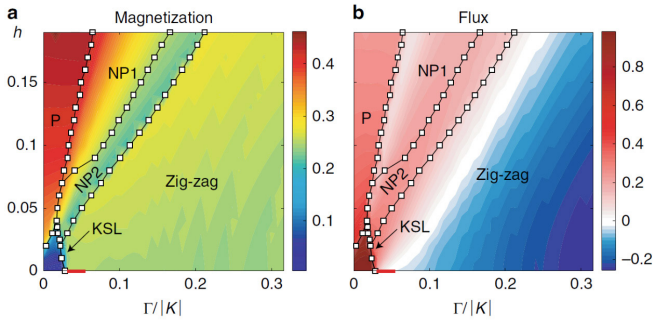

Fig. 1. (a) The magnetization and (b) the flux expectation value of the K-Γ-Γ' model at Γ'= - 0.03. Here "KSL" stands for the chiral Kitaev spin liquid, "P" for a spin-polarized phase, and "NP1" and "NP2" for nematic paramagnet phase. The red solid line at h = 0 denotes a ferromagnetic phase.

may imply the importance of the thermodynamic limit. The tensor network method provides us results for infinite system in contrast to the methods used in the previous ones. At zero field, there is a transition from KSL to a FM (ferromagnetic) phase where spins are aligned in the $[1\bar{1}\bar{1}]$ direction. However, with a very weak magnetic field (h = 0.005), the FM phase disappears, and a direct phase transition from KSL to ZZ (zigzag magnetic ordered) occurs. With increasing the magnetic field, the transition from KSL to the P (polarized) phase occurs at a finite h, where spins start aligning in the [111]-direction.

Apart from the KSL phase, we discovered two non-magnetic states, NP1 and NP2. These phases are characterized by spontaneously-broken 120-degree-lattice-rotational symmetry. When the magnetic field is tilted so that the lattice-rotational symmetry is broken by the Hamiltonian, we found that the phase transition between the KSL and NP2 is continuous in spite that both phases have the same symmetry. This may indicate the non-trivial topological nature of the NP2 phase, which should be clarified in the future study.

Reference

[1] H.-Y. Lee, R. Kaneko, L. E. Chern, T. Okubo, Y. Yamaji, N. Kawashima, and Y. B. Kim, Nature Communications **11**, 1639 (2020)

Authors
H.-Y. Lee[a], R. Kaneko[b], L. E. Chern[c], T. Okubo[d], Y. Yamaji[d], N. Kawashima, and Y. B. Kim[c,e]
[a]ISSP and Korea University
[b]ISSP and Kindai University
[c]University of Toronto
[d]The University of Tokyo
[e]Perimeter Institute

Quantum Criticality of Valence Transition for the Antiferromagnetic Compound $EuCu_2Ge_2$ under Pressure

Uwatoko Group

Most Eu compounds order magnetically because of a divalent electronic state Eu^{2+}. And, valence instability often occurs in Eu compounds, from the divalent electronic state of Eu^{2+} at high temperatures to the nearly nonmagnetic electronic state Eu^{3+} at low temperatures, upon changing the magnetic field and pressure. These compounds can be used to construct a conventional pressure phase diagram with very similar to the Doniach phase diagram for the Ce compounds.

Recently, chemical- and high-pressure measurements have been carried out on single crystals of $EuCu_2(Si_xGe_{1-x})_2$ with the $ThCr_2Si_2$-type tetragonal structure, which undergoes two successive transitions at T_N ~ 15 K and T'_N ~ 9 K on x = 0, and no magnetic orderings on x = 1, at ambient pressure. T_N slightly increases with increasing x and starts decreasing at x = 0.5. and T_N disappears around x ~ 0.7, revealing a mixed-valence or valence-fluctuating state.

In this report, we present the results of electrical resistivity measurements under pressure that revealed a new aspect of the quantum criticality on Eu valence transition[1].

Figure 1 shows the temperature dependence of the electrical resistivity ρ of $EuCu_2Ge_2$ under several pressures. With increasing pressure, the resistivity at room temperature increases because the c - f hybridization between conduction electrons and 4f electrons is enhanced. T_N substantially

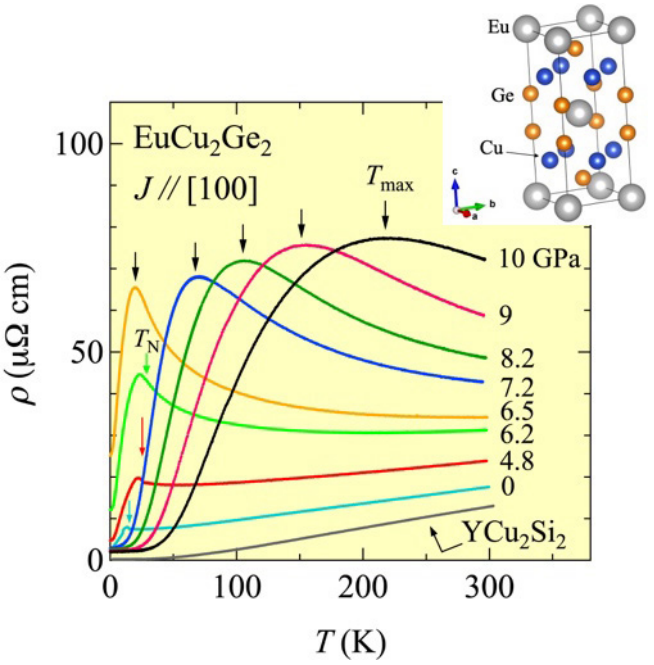

Fig. 1. Temperature dependence of electrical resistivity in $EuCu_2Ge_2$ under several pressures together with the data for YCu_2Si_2 as a reference of the phonon parts of $EuCu_2Ge_2$. The inset shows the tetragonal crystal structure of $EuCu_2Ge_2$.

increases from 15 K and becomes maximum at about 27 K at 6.2 GPa and then it is unclear in a wide temperature region. These results suggest that the valence of Eu increases continuously from nearly divalent to trivalent with increasing pressure. The resistivity at 6.5 GPa indicates no clear magnetic ordering and is typical for a moderate heavy-fermion state. T_{max} remains up to 6.5 GPa and shifts to higher temperatures with further increasing pressure.

Figure 2 shows the P vs Néel temperature T_N phase diagram of $EuCu_2Ge_2$. With increasing pressure, T_N substantially increases from 15 K and becomes maximum at about 27 K at 6.2 GPa. The resistivity at 6.5 GPa indicates no clear magnetic ordering. Note that T'_N disappears rapidly under pressure. In the present case, the Neel temperature became zero abruptly at around 6.5 GPa. This suggests that the valence of Eu increased continuously up to 6.2 GPa, and then the quantum critical point(QCP) of the valence transition arises abruptly at around P_c = 6.5 GPa. The electronic specific heat coefficient, estimated from

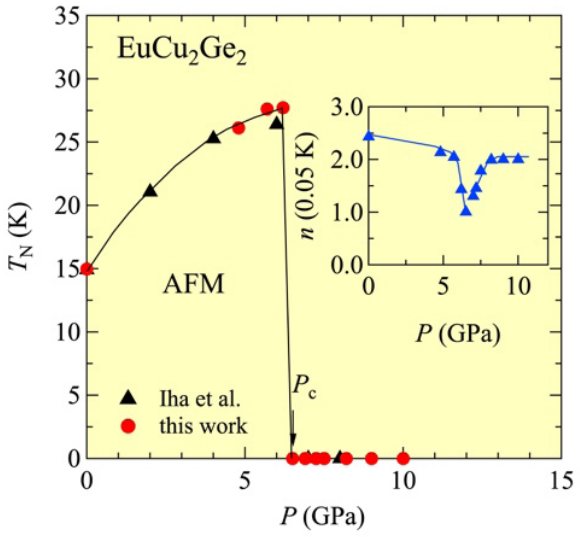

Fig. 2. Pressure-Néel temperature phase diagram in EuCu2Ge2. The inset shows pressure dependence of exponent n of the power law $\rho_{mag} = \rho_{mag0} + BT^n$ of the magnetic resistivity at 0.05 K.

the generalized Kadowaki-Woods plot, was about 510 mJ/(mol K^2), suggesting that the effective mass of the quasiparticles is highly enhanced around P_c. From the analysis of the pressure effect on the exponent n of the power law dependence of the resistivity: $\rho_{mag} = \rho_{mag0} + BT^n$, the fit of the power law to the resistivity data provides valuable information on the pressure dependences of the exponent n of $EuCu_2Ge_2$. It is predicted that n reaches 1.5 for the AF-QCP, while it reaches 1 for the QCP of the valence transition. Inset of Fig. 2 shows the pressure dependence of exponent n. In the magnetic region n is larger than the Fermi liquid value n = 2, probably due to electron-magnon scattering. Approaching P_c, the exponent n decreases as a function of pressure and approaches n = 1. It suggests that the case can be explained as QCP of the valence transition while the scenario based on critical AF-QCP cannot be applied to the present case [1]. This is the first observation of this phenomenon among the Eu compounds.

Reference

[1] J. Gouchi, K. Miyake, W. Iha, M. Hedo, T. Nakama, Y. Ōnuki, and Y. Uwatoko, J. Phys. Soc. Jpn. **89,** 053703 (2020).

Authors
J. Gouchi, K. Miyake[a], W. Iha[b], M. Hedo[b], T. Nakama[b], Y. Ōnuki[b], and Y. Uwatoko
[a]Osaka University
[b]University of the Ryukyus

Kármán-Vortex Cavitation behind Circular-Cylinder Arrays

Noguchi Group

Cavitation is a phenomenon in which bubbles are generated by local pressure changes in a liquid flow. Since cavitation has adverse effects on fluid machinery such as performance degradation, vibration and noise, and erosion, the elucidation of its mechanism is of great engineering importance. Numerically, cavitation has been mainly studied by simulations based on the Navier–Stokes equation. However, it requires a bubble seed to simulate a vapor phase so that it cannot treat the cavitation inception. Here, we directly simulated the cavitation using molecular dynamics (MD) that

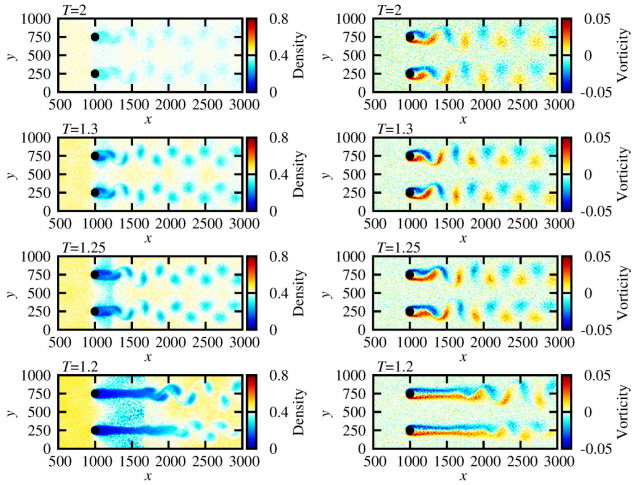

Fig. 1. Snapshots of density (left panels) and vorticity (right panels) fields. The black circles in the figure represent cylinders. At the high temperature, T = 2, Kármán vortex is formed without bubble generation. At the lower temperatures, cavitation occurs. A gas phase (the low-density region in blue color) appears behind the cylinders.

does not require the assumption of a phase transition model or an equation of state for the bubble generation.

We employed Lennard-Jones fluids around periodically aligned side-by-side cylindrical objects at Reynolds number Re~100. As shown in the top panels in Fig. 1, a Newtonian fluid exhibits a Kármán vortex, in which vortexes are periodically generated behind the objects. The neighboring Kármán vortex is synchronized in the antiphase. This synchronization amplifies the vibrations acting on the cylinder. We decrease the temperature to observe the cavitation. At the temperatures T = 1.3 and 1.25, bubbles are generated in conjunction with the shedding cycle of the Kármán vortex (the middle panels in Fig. 1). The Kármán vortex remains synchronized in the anti-phase as in the non-cavitating flow. As the temperature is further reduced to T = 1.2, the gas-phase region behind the cylinder is further expanded, and the upper and lower Kármán vortices become asymmetric (the bottom panels in Fig. 1). This asymmetric structure is switched by a long period of time. A similar dynamics is seen at more closely packed cylindrical arrays in a Newtonian fluid. Thus, the bubbles give an effective increase in the cylindrical diameter.

The change in the vortex structure alters the vibrations excited by the vortex. Because the generated bubbles inhibit the propagation of the vibration associated with the ejection of the vortex, the vibration amplitude decreases and eventually disappears as the cavitation develops.

In summary, the molecular-scale analysis reveals that bubbles generated near the cylinder significantly change the properties of the lift and flow fields.

Reference
[1] Y. Asano, H. Watanabe, and H. Noguchi, J. Chem. Phys. 152, 034501 (2020).

Authors
Y. Asano, H. Watanabe[a], and H. Noguchi
[a]Keio University

Highly Homogeneous Gel without Spatial Heterogeneity

Shibayama Group

Fabrication of ordered nanostructure is a crucial step in a wide range of fields, although the typical size of these objects is still limited to a scale of μm^3 even with current technologies. Polymer gels are a familiar soft material consisting of a nanoporous three-dimensional network that is readily prepared in a large scale, in principle unlimited. However, application of gels as a nanostructured object is obstructed by the fact that gel networks inevitably have a significant level of defects including dangling ends, loops, entanglements, and nonuniform pore sizes, as a result of the fully stochastic gelation reaction. Numerous attempts have been made to remove these defects from polymer gels, including by synthesizing them from monodisperse polymer chains, by using a relatively uniform cross-linking process such as a photoreaction, by limiting unfavorable intramolecular reactions via the A-B type cross-coupling of star polymers, and even by cross-linking polymer chains with movable cross-linkers. Nevertheless, discernible signs of spatial defects have been persistently observed in gels. Gels have been believed to be inherently dis-ordered as a result of the stochastic reaction.

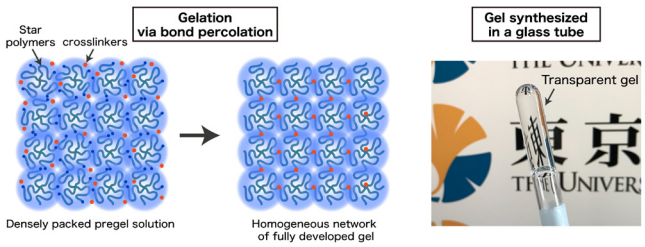

Fig. 1. Illustration of synthesis scheme of highly homogeneous gel via bond percolation. Four-armed star polymer units were dissolved in a good solvent at a concentration much higher than the chain overlapping limit of the polymers. Small crosslinkers were added into the polymer solution. The crosslinkers gradually connect the star polymers and eventually percolate the system. Because there is almost no spatial defect in this polymer gel, the transparency of this material is extremely high.

In this study, we broke this preconception: we present a simple but yet universal scheme to fabricate polymer gels with a highly ordered network. Our strategy is to bring a geometric constraint into the pregel solution so that the space is always uniformly filled with the starting polymer units throughout the gelation reaction (Fig. 1). This gelation framework is known as “bond-percolation” in the classical percolation theory. The spatial and temporal heterogeneity of the synthesized gel network is investigated in the Fourier space by using scattering techniques. Our gel did not show any signatures of heterogeneity: no static laser speckles (Fig. 2), no anomalous small angle scattering, and fully ergodic concentration fluctuations (Fig. 3) and ideal rubber elasticity were observed. These results are completely different from the widely accepted picture of gels. Because both the spatial and temporal correlations of polymer chains in our gels are identical to those of non-crosslinked pre-gel solutions, we cannot even determine the physical state (sol or gel) of our sample by scattering techniques.

Gels have often been discussed in analogy with glass because both gels and glass have a highly disordered structure. However, our results suggest that the bond percolation gel is more like a crystal than glass because almost identical star polymers are closely packed in the space and no spatial defects were detected. The Bragg peaks of the neighboring polymer units were not observed in this gel because the polymer chains can fluctuate much more than atoms in the crystals. This fluctuation of the polymer chains would lead to substantial blurring of the observable correlation between chains.

The simplicity of our gel preparation scheme will enable us to synthesize homogeneous gels with highly ordered network from a variety of polymers with different chemical structures and functionalities (e.g. polydimethylsiloxane, poly(acrylic acid), and poly(N-isopropylacrylamide)), which will open the door to a wide range of new applications.

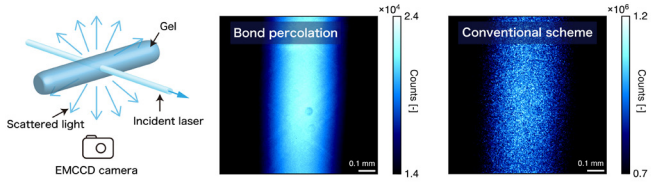

Fig. 2. Static laser speckle test to visualize the spatial defects in the gels synthesized via the bond percolation and conventional scheme. A coherent laser beam was directed to the gel samples and the scattered light was collected using an EMCCD camera. Each image was accumulated for 30 sec to obtain a time-averaged intensity. The bright spots (static laser speckles) in the images denote the static interference from the heterogeneous structures in the gels.

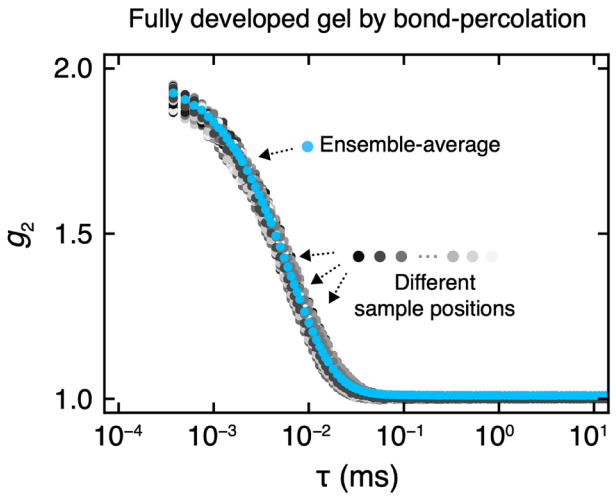

Fig. 3. Intensity time correlation function of the highly homogeneous gel measured with dynamic light scattering at 100 randomly chosen sample positions. All the intensity correlation functions well overlap, indicating the high temporal homogeneity in this gel. The calculated ensemble-averaged intensity correlation function were in perfect consistence with the individual local correlation function, suggesting the ergodic concentration fluctuations of polymer chains in the highly homogeneous gel.

Reference
[1] X. Li, S. Nakagawa, Y. Tsuji, N. Watanabe, and M. Shibayama, Science Advances. **5**, eaax8647 (2019).

Authors
X. Li and M. Shibayama

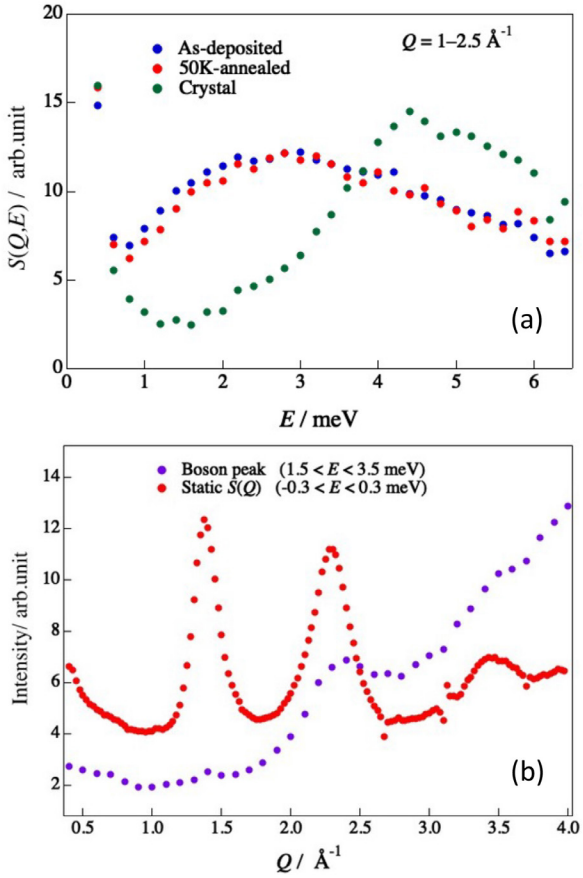

Fig. 1. (a) Inelastic neutron scattering spectra of two glassy and one crystalline states of CCl_4 at 6 K. (b) Q dependence of the boson peak intensity integrated over E = 1.5–3.5 meV. Structure factor $S(Q)$ of glassy CCl_4 is also plotted.

Low-energy Excitations of Glassy Carbon Tetrachloride

Yamamuro Group

There remain many unsolved problems in physical properties of glasses. One of the most important problems is the low-energy excitations (LEE) characteristic to glasses. A broad excitation peak appears around 2-5 meV in most of Raman and inelastic neutron scattering (INS) spectra of glasses. This peak is usually called “boson peak” since the temperature dependence of the peak intensity is scaled well by Bose factors. This peak is basically due to a local excitation since the peak position does not depends on momentum transfer Q. Another interesting phenomenon is the phonon dispersion which has been observed in network glasses [1]. It seems strange that the glasses have phonon dispersion relations since they do not have periodicity. Nevertheless, broad dispersion-like excitations actually exist on dynamic structure factor $S(Q,E)$ planes of glasses. The origins of the above phenomena should be associated with disordered (non-periodic) but locally-ordered structures of glasses. However, their microscopic mechanisms are still unknown.

An essential approach to the LEE problems is the INS study of molecular glasses with simple structures. The study enables us to make direct comparison with the results of various theoretical and computer simulation studies. Vitrification of simple molecules is not easy owing to their prompt crystallization on cooling. Hence we utilize the vapor-deposition (VD) technique whose cooling rate is estimated to be more than 10^7 Ks^{-1}.

We have measured the INS spectra of VD carbon tetrachloride (CCl_4) glass on AMATERAS, J-PARC. Fig. 1(a) shows the $S(Q,E)$ data in the boson peak energy region. A clear boson peak appeared at around 2.5 meV in the glassy state while a sharper peak, which corresponds to the Debye cut-off of the acoustic phonon, at 4.5 meV in the crystalline state. The annealing at 50 K slightly reduced the intensity of the boson peak in the lower-energy side as observed in VD molecular glasses [2]. Fig. 1(b) gives the Q dependence of the boson peak intensity. The intensity has a clear hump at 2.3 Å^{-1} and 3.4 Å^{-1} which coincides with the second and third peak positions in $S(Q)$. This is a similar Q dependence

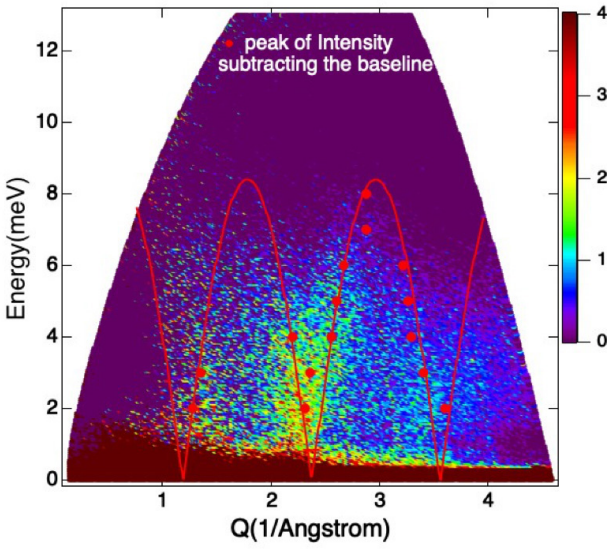

Fig. 2. $S(Q,E)/Q^2$ color contour map of the glassy CCl_4 data at 6 K from which normal phonon contribution proportional to Q^2 has been subtracted in advance.

to that of the boson peak of SiO_2 glass [3]. The phenomenon is roughly explained by a coupled rotation model of the SiO_4 tetrahedral unit. Fig. 3 shows the $S(Q,E)/Q^2$ color contour map of the data in which normal phonon contribution proportional to Q^2 has been subtracted. It is of interest that, as shown by red curves, the phonon excitation has a clear dispersion relation starting at Q = 2.3 Å^{-1} where the boson peak intensity has a maximum and $S(Q)$ exhibits the second peak. This is the first observation of the dispersion-like excitation in molecular glasses. We are now trying a normal mode analysis based on the local structure determined by the reverse Monte Carlo analysis on the X-ray diffraction data which was obtained in SPring-8.

References

[1] M. Arai, Y. Inamura, T. Otomo, N. Kitamura, S. M. Bennington, and A. C. Hannon, Physica B **263**, 268 (1999).
[2] O. Yamamuro, I. Tsukushi, T. Matsuo, K. Takeda, T. Kanaya, and K. Kaji, J. Chem. Phys. **106**, 2997 (1997).
[3] U. Buchenau, M. Prager, N. Nücker. A. J. Dianoux, N. Ahmad, and W. A. Phillips, Phys. Rev. B **34**, 5665 (1986).

Authors

X. Wu, M. Kofu[a], Y. Mizuno, H. Akiba, T. Kikuchi[a], S. Kawamura[a], K. Nakajima[a], and O. Yamamuro

[a]J-PARC, JAEA

Novel Excitations near Quantum Criticality in Geometrically Frustrated Antiferromagnet $CsFeCl_3$

Masuda Group

For understanding condensed matter, the investigation of the collective excitation in low energy range is indispensable. According to the quantum field theory, the excitation in the system with spontaneously symmetry broking is characterized by phase and amplitude fluctuations of order parameters. The former is known as the Nambu-Goldstone (NG) mode, and the latter is called as the amplitude mode. Even though these modes are usually separated, they are hybridized under some conditions, and interesting phenomena are induced; for example in a crystal lattice system, acoustic phonon (NG mode) and optical phonon (amplitude mode) are hybridized through anharmonic terms in a thermoelectric material PbTe, which renormalizes the phonon spectrum and leads to low thermal conductivity and high figure of merit in thermoelectric property [1]. Such a hybridization effect could exist in other types of elementary excitations, however, no research has been reported to our knowledge partially because longitudinal mode itself is not trivial.

Spin S = 1 easy-plane antiferromagnet is one of the prototypical quantum spin systems that allows to explore the quantum phase transition (QPT) [2]. When the anisotropy D is large, the ground state is a quantum disordered (QD) singlet as shown in Fig. 1 left panel. When D is small and the exchange interaction is large, the ground state is magnetically long-range ordered state. A remarkable feature in the renormalized energy scheme in Fig. 1 right panel is that the second excited state can be excited only by the longitudinal component of spin operator $S^{\parallel}$, meaning that the longitudinal mode is allowed in the system. Because the geometrical frustration in magnets could induce the hybridization of the transverse (T) and longitudinal (L) modes, spin S = 1 easy-plane antiferromagnet having geometrically frustrated lattice is the best playground for the research of hybridized modes in magnetic material.

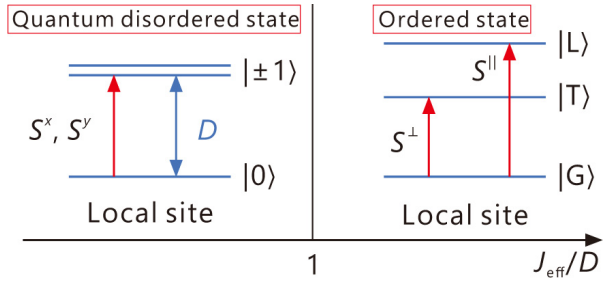

Fig. 1. Schematic diagram of the S = 1 easy-plane antiferromagnet. In the ordered state, the doublet excited states |±1> splits into |*L*> and |*T*>. Here, the former and latter have longitudinal and transverse fluctuations, respectively.

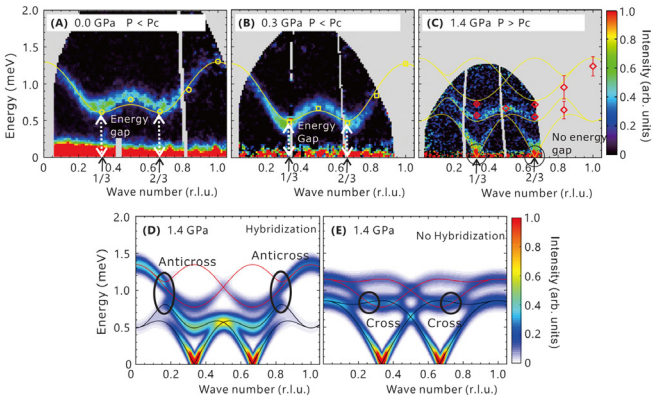

Fig. 2. Inelastic neutron scattering spectra. The spectra obtained at a chopper spectrometer under (A) 0.0 GPa at 6 K, (B) 0.3 GPa at 2.7 K and (C) 1.4 GPa at 0.9 K sliced by the energy transfer - wave vector ($\hbar\omega$ – $\boldsymbol{q}$) plane for q = (-k, 2k, 0). The yellow circles, squares, and red diamonds are the peak positions of the excitations obtained from the constant-q scans using a triple-axis spectrometer. The solid yellow curves are the dispersions calculated by ESW. Calculated neutron cross-section by the ESW under (D) 1.4 GPa at 0 K. Calculated neutron cross-section in the absence of the off-diagonal elements under (E) 1.4 GPa at 0 K. The black and red solid curves in (D) and (E) are gapless and gapped modes, respectively.

$CsFeCl_3$ is the S = 1 easy-plane triangular antiferromagnet. The inelastic neutron scattering (INS) study at ambient pressure revealed that the ferromagnetic chains along the crystallographic c axis are antiferromagnetically coupled in the ab plane [3]. The ground state is the QD state because of large single-ion anisotropy. The magnetic susceptibility measurement under pressures exhibited a pressure-induced magnetic order above a critical pressure of about 0.9 GPa [4]. Owing to the strong easy-plane anisotropy, the ordered moment aligns in the ab plane; the neutron diffraction evidenced the noncollinear 120° structure in the LRO phase [5]. $CsFeCl_3$ is, thus, a promising host for the pressure-induced QPT in the geometrically frustrated lattice. In 2019 our group reported a new hybridization of the phase and amplitude fluctuations of the order parameter near QCP in $CsFeCl_3$ [6].

The INS spectrum measured at 0.0 GPa by using chopper spectrometer in Fig. 2A exhibits a single dispersive excitation with the energy gap of 0.6 meV at the wave vectors $\boldsymbol{q}$ = (-k, 2k, 0) for k = 1/3 and 2/3. The energy gap at 0.3 GPa in Fig. 2B becomes softened when approaching the ordered state. A qualitatively different spectrum is observed in the ordered state at 1.4 GP in Fig. 2C. A well-defined gapless excitation emerges at k = 1/3 and 2/3 and another dispersive excitation are observed in the higher energy range. The INS spectra were collected also by using a triple-axis spectrometer in order to cover wide $\hbar\omega$ – $\boldsymbol{q}$ range, and the

extracted peak energies are overplotted by open symbols in Figs 2A-2C. At 1.4 GPa, the spectral lineshape at k = 5/6 was reproduced by double Lorentzians with broad widths which is reflected by large errorbars. The dispersion relations calculated by the extended spin-wave theory (ESW) [7] are indicated by the solid yellow curves. The calculation is consistent with the experiment both in the QD and LRO phases.

In ESW calculation one can notice that noncollinearity of the magnetic structure makes off-diagonal elements in the Hamiltonian nonzero, leading to the hybridization of L and T modes in one-magnon process. To understand the effects of LT-hybridization, we demonstrate the INS spectra after dropping the off-diagonal element. The results are shown in Figs. 2E, where the black-gapless (red-gapped) modes are pure transverse (longitudinal) modes in this case. The result is inconsistent with the experiment in Fig. 2C. When LT-hybridization is taken into account, the off-diagonal elements lead to anticross of the modes at k~ 5/6 in Fig. 2D, and novel magnetic excitations are formed; both gapless and gapped modes are accompanied by strong longitudinal and transverse fluctuations. The result is consistent with the experiment, and, thus, the LT-hybridization plays an important role in magnon dynamics in noncollinear magnet near QCP.

Since the newly found excitation exists in a noncollinear spin structure, the search of the excitation in different types of noncollinear structures such as cycloidal structure, all-in-all-out structure, and skyrmion lattice would be interesting topics. The search of the hybridized mode in other systems including charge density wave, spin density wave, and ultracold atoms would be important. Finally, the effect of hybridization to the lifetime of the magnon and other elementary excitations would be also interesting.

References

[1] O. Delaire, J. Ma, K. Marty, A. F. May, M. A. McGuire, M. H. Du, D. J. Singh, A. Podlesnyak, G. Ehlers, M. D. Lumsden, and B. C. Sales, Nat. Mat. **10**, 614 (2011).
[2] M. Matsumoto and M. Koga, J. Phys. Soc. Jpn. **76**, 073709 (2007).
[3] H. Yoshizawa,W. Kozukue, and K. Hirakawa, J. Phys. Soc. Jpn. **49**, 144 (1980).
[4] N. Kurita and H. Tanaka, Phys. Rev. B **94**, 104409 (2016).
[5] S. Hayashida, O. Zaharko, N. Kurita, H. Tanaka, M. Hagihala, M. Soda, S. Itoh, Y. Uwatoko, and T. Masuda, Phys. Rev. B **97**, 140405 (2018).
[6] S. Hayashida, M. Matsumoto, M. Hagihala, N. Kurita, H. Tanaka, S. Itoh, T. Hong, M. Soda, Y. Uwatoko, and T. Masuda, Sci. Adv. **5**, eaaw5639 (2019).
[7] R. Shiina, H. Shiba, P. Thalmeier, A. Takahashi, and O. Sakai, J. Phys. Soc. Jpn. **72**, 1216 (2003).

Authors

S. Hayashida, M. Matsumoto[a], M. Hagihala, N. Kurita[b], H. Tanaka[b], S. Itoh[c], T. Hong[d], M. Soda, Y. Uwatoko and T. Masuda

[a]Shizuoka University
[b]Tokyo Institute of Technology
[c]KEK
[d]Oak Ridge National Laboratory

Magnetic Structure and Excitation of Quasi One-Dimensional Antiferromagnet $Ba_2CoSi_2O_7$

Masuda Group

The relationship between magnetism and dielectricity has been extensively studied. In the multiferroics, the ferroelectrics with the cycloidal and proper-screw magnetic structures are explained by the spin-current mechanism and the spin-dependent d–p hybridization mechanism, respectively [1,2]. On the other hand, the multiferroic property has been reported even on a collinear antiferromagnet. One of the maultiferroics with the collinear magnetic structure is an antiferromagnet $Ba_2CoGe_2O_7$. $Ba_2CoGe_2O_7$ with the Co-square lattice shows multiferroic properties, and the local electric polarization of CoO_4 tetrahedra is explained by the spin-dependent d-p hybridization mechanism [3,4]. In contrast, the anomaly of the dielectric constant in similar material $Ba_2CoSi_2O_7$ is not observed at the antiferromagnetic transition temperature T_N =6 K [5]. $Ba_2CoSi_2O_7$ has a distorted crystal structure formed by CoO_4 and SiO_4 networks, as shown in Fig. 1(a), and two kinds of Co-Co bonds exist within the b-plane. In order to clarify the magnetic model of $Ba_2CoSi_2O_7$, the magnetization and neutron scattering measurements have been performed.

In the neutron powder diffraction measurement using the high-resolution powder diffractometer ECHIDNA installed at OPAL, ANSTO, Australia, the magnetic reflections indexed by the propagation vector (1/2, 1/2, 1/2) was observed below T_N = 6 K. By analyzing the powder neutron profile, we found that a collinear antiferromagnetic structure shown in Fig. 1(b) was realized below T_N = 6 K. The magnetic moments with the easy axis along the [10-1] form an antiferromagnetic arrangement along [101] and a ferromagnetic arrangement along [10-1]. In the spin-dependent d-p hybridization mechanism, the local electric polarization of the CoO_4 tetrahedron is almost zero with the magnetic moment along [10-1]. This is consistent with the dielectric property where the temperature dependence of the dielectric constant has no anomaly at T_N = 6 K.

We have also measured the $\boldsymbol{Q}$-dependencies of the magnetic excitations along the b^*, [10-1], and [101] directions at 1.5 K to clarify the magnetic correlation of $Ba_2CoSi_2O_7$ by using a cold-neutron triple-axis spectrometer (CTAX) installed at HFIR, ORNL, USA. Figure 2(a) shows the constant-$\boldsymbol{Q}$ scan profiles measured at (h, 1/2, h). Figure 2(b) shows the h-dependence of integrated intensities and peak energies obtained by Gaussian fitting of the constant-$\boldsymbol{Q}$ profiles at (h, 1/2, h), which corresponds to the $\boldsymbol{Q}$-dependence along the [101] direction. The excitation observed at $\hbar w$ = 2.9 meV is almost dispersionless, but the integrated

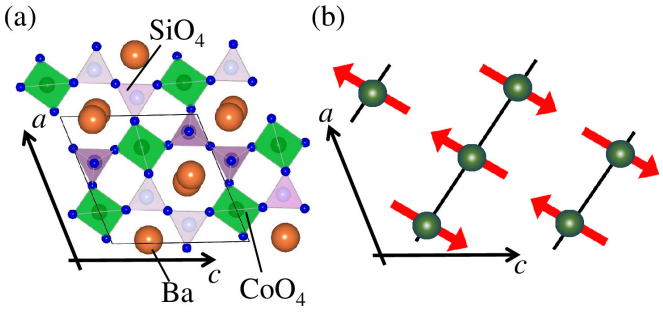

Fig. 1. (a) Crystal structure of $Ba_2CoSi_2O_7$. (b) Schematic magnetic structure of $Ba_2CoSi_2O_7$.

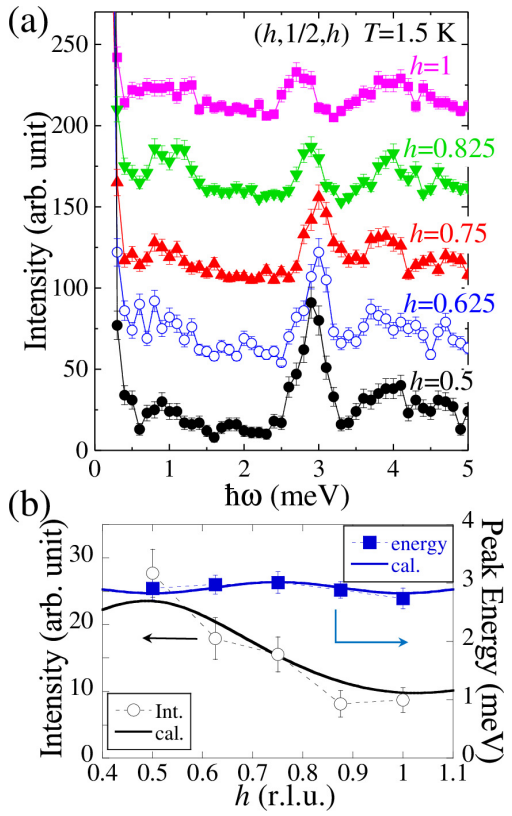

Fig. 2. (a) Constant-$\boldsymbol{Q}$ scans at (h, 1/2, h) measured at 1.5 K. Data are shifted by vertical offsets. (b) Integrated intensities and the peak energies at (h, 1/2, h). Solid lines are the calculated values with the classical spin-wave theory.

intensity exhibits a clear modulation along the [101] direction. In the measurements along the b^* and [10-1] directions, on the other hand, both the neutron intensity and peak energy show less change. (not shown)

We analyzed the magnetic excitation by using the spin Hamiltonian in order to clarify the magnetic model including the magnetic interaction in $Ba_2CoSi_2O_7$. To explain the observed magnetic excitation, we consider the one-dimensional antiferromagnet in which the antiferromagnetic chain is along the [101] direction. We performed the calculations of the neutron intensity and the dispersion energy for both the easy-axis and Ising-like antiferromagnet models; two models cannot be distinguished in the classical spin-wave theory. The magnetic dispersion relation shown in Fig. 2(b) is reproduced by the one-dimensional antiferromagnet model, as shown by solid curves.

Our results of the neutron scattering suggest that the $Ba_2CoSi_2O_7$ is the one-dimensional antiferromagnet with the easy-axis spin anisotropy or the Ising-like spin. On the other hand, $Ba_2CoGe_2O_7$ with the tetragonal structure is two-dimensional easy-plane antiferromagnet. The neutron results suggest that the crystal structure affects both the magnetic interaction dimensionality and anisotropy in åkermanite-type materials.

References

[1] T. Kimura, T. Goto, H. Shintani, K. Ishizaka, T. Arima, and Y. Tokura. Nature **426**, 55 (2003).
[2] S. Seki, Y. Onose, and Y. Tokura. Phys. Rev. Lett. **101** 067204 (2008).
[3] H. Murakawa, Y. Onose, S. Miyahara, N. Furukawa, and Y. Tokura. Phys. Rev. Lett. **105**, 137202 (2010).
[4] M. Soda, M. Matsumoto, M. Månsson, S. Ohira-Kawamura, K. Nakajima, R. Shiina, and T. Masuda, Phys. Rev. Lett. **112**, 127205 (2014).
[5] M. Akaki, J. Tozawa, D. Akahoshi, and H. Kuwahara, J. Phys.: Conf. Ser. **150**, 042001 (2009).

Authors

M. Soda[a], T. Hong[b], M. Avdeev[c], H. Yoshizawa[a], T. Masuda, and H. Kawano-Furukawa[a,d]

[a]RIKEN
[b]ORNL
[c]ANSTO
[d]Ochanomizu University

High-Field Ultrasonic Study of Quadrupole Ordering and Crystal Symmetry Breaking in $CeRhIn_5$

Tokunaga Group

In a number of strongly correlated electron systems, the electronic nematic (EN) state characterized by the lacking of the $C_4^{\pm}$-rotational operations has been focused because the EN contribution to superconductivity and other exotic phenomena have been proposed. Recently, the field-induced EN phase above 30 T has been proposed in the D_{4h}[1] tetragonal compound of $CeRhIn_5$ [1,2], which was well known as a pressure-induced heavy-fermion superconductor.

To investigate the active representation and the order parameter of the field-induced EN phase, we performed an ultrasonic measurement for $CeRhIn_5$ in pulsed magnetic fields up to 56 T [3]. The ultrasound technique is a powerful tool to determine the active representation of a phase transition related to the crystal symmetry breaking because sound waves can induce the symmetry strain belonging to the irreducible representation (IR) of the space group. Furthermore, we can propose the electric quadrupole as an order parameter of the crystal symmetry breaking and the EN state in terms of the electric quadrupole-strain interaction, which is based on the selection rule of group theory.

To identify the active representation of the symmetry breaking at the EN state, we measured all the elastic constants of $CeRhIn_5$ that can be detected in the tetragonal system. As shown in Fig. 1, the transverse elastic constant $C_T = (C_{11} - C_{12})/2$ with the B_{1g} IR of D_{4h} shows the anomaly at B_{IM} = 28.5 T at 1.4 K and 2.1 K. This B_{IM} is consistent with the previous studies [1, 2]. While C_T shows an anomaly, other elastic constants, which can identify the symmetry breaking of B_{2g} and E_g IR, do not exhibit anomaly at B_{IM}. Therefore, our ultrasonic measurements demonstrate the B_{1g}-type crystal symmetry breaking. Furthermore, the

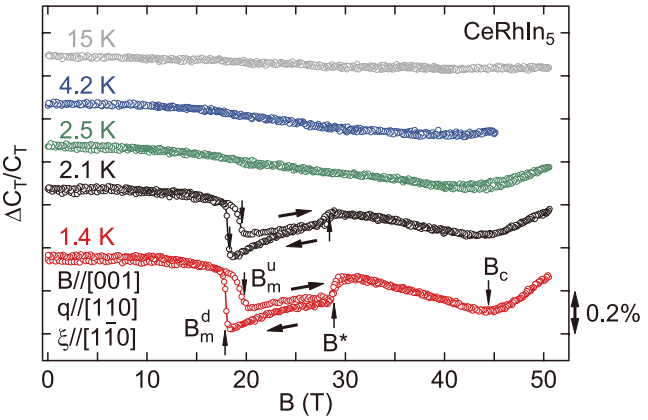

Fig. 1. Magnetic field dependence of the transverse elastic constant $\Delta C_T/C_T$ at several temperatures for B//[001]. The vertical arrows indicate the metamagnetic transition field $B_m^{u(d)}$ for field up(down) sweep, the EN transition field B^*, and the critical field B_c. The right and left arrows show hysteresis direction. The propagation direction $\boldsymbol{q}$ and polarization direction $\boldsymbol{\xi}$ of ultrasound are indicated.

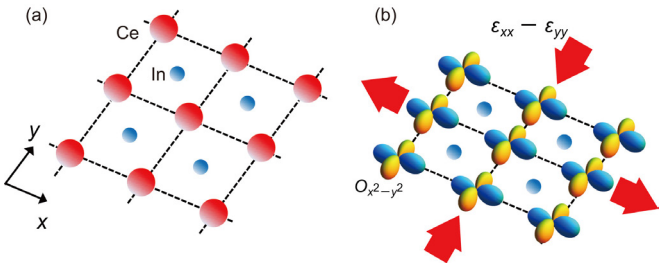

Fig. 2. Schematic view of the B_{1g}-type quadrupole ordering and crystal symmetry breaking. (a) Crystal structure in the xy plane of $CeRhIn_5$ in the normal phase. (b) High-field symmetry breaking state of $CeRhIn_5$. The red arrows indicate the deformation direction of the crystal lattice due to the strain $\varepsilon_{x^2-y^2} = \varepsilon_{xx} - \varepsilon_{yy}$.

electronic degree of freedom with the B_{1g} IR, namely the electric quadrupole $O_{x^2-y^2} \propto (x^2 - y^2)/r^2$, can be the order parameter of the EN state. This symmetry breaking is attributed by the electric quadrupole-strain coupling written as $H_{QS} = -g_{x^2-y^2} O_{x^2-y^2} \varepsilon_{x^2-y^2}$.

We show the schematic view of the B_{1g}-type ferroic electric quadrupole ordering and crystal symmetry breaking in Fig. 2. The square lattice of $CeRhIn_5$ with the tetragonal crystal structure of D_{4h}^1 is drawn in Fig. 2(a). In the field-induced EN state, the electric quadrupole $O_{x^2-y^2}$ appears on the Ce site. The lattice changes from the square of the tetragonal structure to the rectangle of orthorhombic one due to the quadrupole-strain coupling H_{QS} accompanying the lattice distortion $\varepsilon_{x^2-y^2} = \varepsilon_{xx} - \varepsilon_{yy}$. A maximal nonisomorphic orthogonal subgroup D_{2h}^1 is an appropriate space-group for this symmetry lowering from D_{4h}^1.

Furthermore, we found the acoustic de Haas-van Alphen (AdHvA) oscillation in C_T with the frequency 690 T, which has not been observed experimentally. On the other hand, the theoretical study treating 4*f* electrons as itinerant has shown a hole Fermi surface with the frequency ~ 690 T [4]. Thus, we proposed the origin of the AdHvA oscillation in terms of the quadrupole-strain coupling in the *k*-space based on the deformation potential theory [5].

We also discussed the quantum state possessing the electric quadrupole. The delocalization of 4*f* electrons and the in-plane type *p*-*f* hybridization are candidate interactions constructing the quantum state in high fields.

References
[1] P. J. Moll *et al*., Nat. Commun. **6**, 6663 (2015).
[2] F. Ronning *et al*., Nature (London) **548**, 313 (2017).
[3] R. Kurihara *et al*., Phys. Rev. B **101**, 115125 (2020).
[4] D. Hall *et al*., Phys. Rev. B **64**, 064506 (2001).
[5] M. Kataoka and T. Goto, J. Phys. Soc. Jpn. **62**, 4352 (1993).

Authors
R. Kurihara, A. Miyake, M. Tokunaga, Y. Hirose[a], and R. Settai[a]
[a]Niigata University

Discovery of Metamagnetic Transition in New Unconventional Superconductor UTe_2

Tokunaga Group

News of the discovery of unconventional superconductivity in a paramagnetic heavy-fermion system UTe_2 at the end of 2018 has excited strongly the researchers working on the condensed matter physics. Within a few years since the first report in arXiv, many new aspects have been unveiled both experimentally and theoretically. One of the intriguing phenomena in UTe_2 recognized in the very early stage is its large superconducting critical fields. For the magnetic fields applied along the hard magnetization *b*-axis, the superconducting transition can survive well above the Pauli paramagnetic limit [1,2]. This fact suggests the realization of the long-sought spin-triplet superconductivity. Such unconventional superconductivity is believed to realize in the ferromagnetic superconductors (FMSCs), such as URhGe and UCoGe. In the case of UTe_2, however, the ground state is paramagnetic. Here, we introduce our observation of metamagnetic transition in UTe_2 and discuss the relation between metamagnetism and superconductivity by compared to FMSCs [3].

The high-field magnetization was measured by using the pulse magnets installed in the International MegaGauss Science Laboratory. Figure 1(b) shows the magnetization curve for the field along the *b* axis at 1.4 K. At $\mu_0 H_m$ ~ 35 T, magnetization suddenly increases with a large step of ~0.6 μ_B. Because of the hysteric behavior against the magnetic field, this metamagnetic transition is of first-order. From the magnetization curves at various temperatures, we summarized a magnetic phase diagram of UTe_2 in Fig. 1(a). The field hysteresis disappears above 11 K, indicating the existence of the critical end point (CEP), and the transition changes to crossover. As known in many paramagnets, the energy scale of metamagnetic transition, $\mu_0 H_m$, corresponds to T_χ^{max}, where the temperature dependence of magnetic susceptibility shows a broad maximum. This relation is further supported by the fact that $\mu_0 H_m(T)$ connects to $T_\chi^{max}(\mu_0 H)$. At almost the same time, the high-field magnetoresistance measurements independently revealed a similar phase diagram [4]. A sharp step-like increase in the resistance across the H_m may reflect the modification of the Fermi surface, although it is not clear yet. More interestingly, the superconducting (SC) phase shows a reentrant behavior above 16 T and is suddenly suppressed above $\mu_0 H_m$ [5] [see

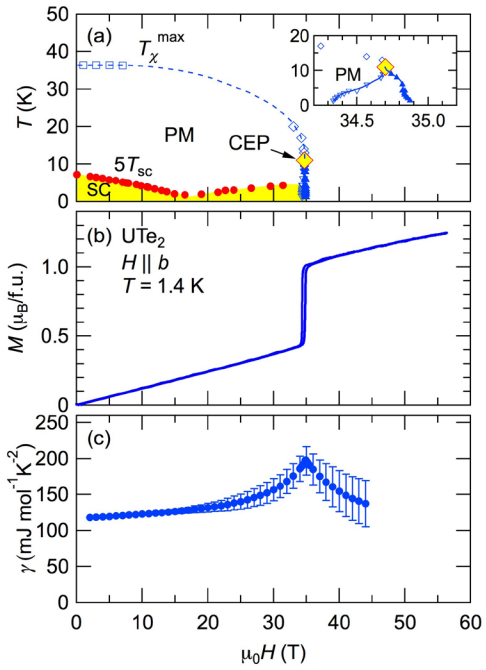

Fig. 1. (a) Magnetic phase diagram of UTe_2 for $H \parallel b$ determined by H_m and T_c^{max}. CEP denoted by a diamond is critical end point. (b) Magnetization curve for $H \parallel b$ at 1.4 K. (c) Magnetic field dependence of the electronic specific heat derived from magnetization curves by the Maxwell relation.

Fig. 1(a)]. This unusual T_c enhancement can be explained qualitatively by a simple mass-enhancement model as follows. Figure 1(c) represents the magnetic-field evolution of the electronic specific heat g, derived by the thermodynamic Maxwell relation using the temperature dependencies of magnetization at constant fields [3]. With increasing fields, the γ increases and shows a maximum at H_m. This enhancement is also confirmed by the direct specific heat measurement using a pulse magnet in ISSP [6]. This enhancement on going to metamagnetic transition indicates that the development of the fluctuation evolves around H_m. This fluctuation may stabilize the SC phase even at high magnetic fields as has been adapted to explain the reentrant superconductivity in URhGe. Using a simplified McMillan-type formula, the field-enhancement of the superconducting transition temperature can be reproduced qualitatively [see Refs. 3 and 6 for more detail and references therein].

Now, it is no doubt that the high-field studies make an important role to reveal the superconductivity on UTe_2. Soon after our work [4], more exciting phenomena in high fields were reported [7]: Surprisingly, another SC phase appears at H_m when the field is applied intermediate angles between the a and c axis. This is in stark contrast to the fact of suppression of SC at H_m for the b axis. Our struggles continue.

References

[1] S. Ran, C. Eckberg, Q.-P. Ding, Y. Furukawa, T. Metz, S. R. Saha, I.-L. Liu, M. Zic, H. Kim, J. Paglione, and N. P. Butch, Science **365**, 684 (2019).
[2] D. Aoki, A. Nakamura, F. Honda, D. X. Li, Y. Homma, Y. Shimizu, Y. J. Sato, G. Knebel, J.-P. Brison, A. Pourret, D. Braithwaite, G. Lapertot, Q. Niu, M. Vališka, H. Harima, and J. Flouquet, J. Phys. Soc. Jpn. **88**, 043702 (2019).
[3] A. Miyake, Y. Shimizu, Y. J. Sato, D. Li, A. Nakamura, Y. Homma, F. Honda, J. Flouquet, M. Tokunaga, and D. Aoki, J. Phys. Soc. Jpn. **88**, 063706 (2019).
[4] W. Knafo, M. Vališka, D. Braithwaite, G. Lapertot, G. Knebel, A. Pourret, J.-P. Brison, J. Flouquet, and D. Aoki, J. Phys. Soc. Jpn. **88**, 063705 (2019).
[5] G. Knebel, W. Knafo, A. Pourret, Q. Niu, M. Vališka, D. Braithwaite, G. Lapertot, M. Nardone, A. Zitouni, S. Mishra, I. Sheikin, G. Seyfarth, J.-P. Brison, D. Aoki, and J. Flouquet, J. Phys. Soc. Jpn. **88**, 063707 (2019).
[6] S. Imajo, Y. Kohama, A. Miyake, C. Dong, J. Flouquet, K. Kindo, and D. Aoki, J. Phys. Soc. Jpn. **88**, 083705 (2019).
[7] S. Ran, I.-L. Liu, Y. S. Eo, D. J. Campbell, P. Neves, W. T. Fuhrman, S. R. Saha, C. Eckberg, H. Kim, J. Paglione, D. Graf, J. Singleton, and N. P. Butch, Nat. Phys. **15**, 1250 (2019).

Authors

A. Miyake, Y. Shimizu[a], Y. J. Sato[a], D. Li[a], A. Nakamura[a], Y. Homma[a], F. Honda[a], J. Flouquet[b], M. Tokunaga, and D. Aoki[a, b]
[a]Tohoku University
[b]CEA-Grenoble

High-Magnetic-Field X-Ray Diffraction Study in Solid Oxygen

Y. Matsuda Group

Molecular oxygen is a unique homonuclear diatomic molecule because it possesses a spin quantum number S = 1. After M. Faraday had noticed that gaseous oxygen exhibits magnetism, condensed phases, namely liquid and solid phases have been extensively studied as intriguing magnetic materials. Solid oxygen undergoes successive phase transitions with lowering temperature, and three distinct phases, γ-phase, β-phase, and α-phase appear at 54, 44, and 24 K, respectively. One of the most intriguing findings on these three phases is that they have different crystal symmetries,

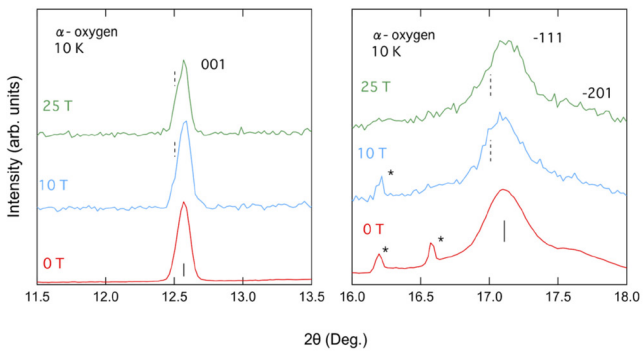

Fig. 1. High-magnetic-field X-ray diffraction profiles of the α-phase of solid oxygen at 10 K. Vertical dashed lines indicate the positions that are expected from the previous report [2]. (a) 001 reflection peaks are shown. (b) -111 and -201 peaks are shown. Peaks with * are considered to be due to impurities on the window of the sample cell.

meaning that the successive phase transitions are not merely magnetic phase transitions but structural phase transitions. The γ-phase, β-phase, and α-phase have a cubic, rhombohedral, and monoclinic crystal structure, respectively. The lowest temperature phase, the α-phase is an antiferromagnet at a low temperature below 24 K, while the β-phase only exhibits a short-range antiferromagnetic correlation and the γ-phase is paramagnetic. We have been sharing the idea that magnetic energy between oxygen molecules should play an important role for having different crystal structure for a long time. However, no direct experimental evidence of the strong spin-lattice coupling had ever been obtained before the discovery of the novel magnetic-field-induced θ-phase at 120 T [1]. It has been proved that controlling spins induces a novel oxygen crystal.

Microscopic investigation of the crystal lattice of solid oxygen in magnetic fields is important. Actually, there was a report of the high magnetic field x-ray diffraction of the solid oxygen using a synchrotron x-rays up to 8 T and significantly large magnetostriction was likely to occur in the α-phase of solid oxygen [2]. The volume striction $\Delta V/V$ was found to reach around 10^{-2}. In the present study, we have extended the magnetic field range to 25 T for the x-ray diffraction experiment.

The high-field XRD experiments have been performed at the Institute for Materials Research of Tohoku University with a DC magnet up to 5 T, and at BL22XU in SPring- 8 up to 25 T using a pulsed magnet. Pure oxygen gas (purity > 99.99995%) was liquified by cooling into a sample cell designed for each experiment. For the 5 T DC-magnet experiment, a CuKα (1.54 Å) characteristic emission line

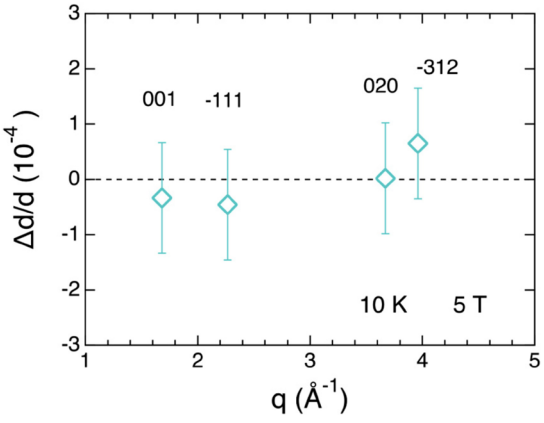

Fig. 2. The relative changes of the diffraction plane spacing at 5 T are shown at different reciprocal vectors.

was used as the x-ray source. The measurement temperature was controlled to be 10 K. In the 25 T pulse-magnet experiments, the photon energy (wavelength) of the synchrotron x-ray used is 15 keV (0.8266 Å). The time interval of the successive pulsed magnetic field measurements is 10–20 min, which is necessary for cooling the magnet after heating due to the discharge for field generation. The variation of the magnetic field ΔB/B during the measurement time (100 μs) is around 2% [3].

The measured XRD profiles in pulsed magnetic fields at 10 and 25 T are shown in Fig. 1 along with the zero-field profile. The XRD at 0 T is measured with an exposure time of 10 ms. The profiles at 10 and 25 T are obtained by averages of six times and five times the repetition of the measurements, respectively. The obtained XRD profiles at different magnetic fields seem to be identical at first glance.

In order to confirm the unexpectedly small magnetic field effect, we have also analyzed the steady field XRD data that have higher precision in terms of the longer accumulation time. And also, we need to exclude a possibility that the dynamics of the crustal lattice is slower than the pulsed magnetic field of which duration time is 1 ms in this study.

Figure 2 shows the obtained linear magnetostriction Δd/d at 5 T. The Δd/d of several diffraction plane spacing is found to be as small as 10^{-4} which is more than one order of magnitude smaller than the values reported previously [2].

The reason for the contradiction between our results and the previous study is not very clear. One of the possible causes for the contradiction is that there had been some mechanical influence on the experimental configuration by applying DC magnetic fields. Small mechanical movements of measurement apparatuses can cause a change in the observed XRD peak positions [3].

The high-field XRD experiments on α oxygen at 10 K has revealed that the linear magnetostriction Δd/d is smaller than 10^{-4} T^{-1} in magnetic fields of up to 25 T [3]. The absence of the giant magnetostriction in α oxygen is also in agreement with the experimental fact that the magnetic field induced α-θ transition is first order [1]. The deformation of the crystal lattice in a magnetic field is not significant below the critical magnetic field around 100 T. It is likely that a drastic symmetry change in the crystal lattice takes place discontinuously at the phase transition.

References

[1] T. Nomura, Y. H. Matsuda, S. Takeyama, A. Matsuo, K. Kindo, J. L. Her, and T. C. Kobayashi, Phys. Rev. Lett. **112**, 247201 (2014).
[2] K. Katsumata, S. Kimura, U. Staub, Y. Narumi, Y. Tanaka, S. Shimomura, T. Nakamura, S. W. Lovesey, T. Ishikawa, and H. Kitamura, J. Phys.: Condens. Matter **17**, L235 (2005).
[3] Y. H. Matsuda, A. Shimizu, A. Ikeda, T. Nomura, T. Yajima, T. Inami, K. Takahashi, T. C. Kobayashi, Phys. Rev. B **100**, 214105 (2019).

Authors

Y. H. Matsuda, A. Shimizu, A. Ikeda, T. Nomura, T. Yajima, T. Inami[a], K. Takahashi[b], and T. C. Kobayashi[c]

[a]National Institutes for Quantum and Radiological Science and Technology
[b]Tohoku University
[c]Okayama University

Observation of Quantum Spin-Nematic Phase in Volborthite

Kohama, Kindo and Hiroi Groups

For a long time, it was believed that matter could exist in only three different forms, solid, liquid and gas. However, in the second half of the nineteenth century, it became clear that not all substances could be described as solid, liquid or gas. Liquid crystals came of age in the twentieth century, as both a subject of fundamental research and the basis for modern display technology. Since we know examples of quantum gases, liquids and solids, it is natural to ask, *are there quantum liquid crystals, too*? For a long time, this question remained a mathematical curiosity. However, in recent years, potential quantum analogues of a liquid crystal state have been discussed in real material, which is called a quantum spin-nematic state. Its experimental observation has proved much more challenging, since the order parameter of the spin nematic state, spin quadrupole moment, is hard to detect with conventional magnetic probes.

In this research, with an exotic frustrated magnet, volborthite, we provided the possible evidence of quantum analogue of the nematic crystal, and resolved a long-standing mystery about the magnetism of volborthite [1]. Here we applied thermodynamic measurement techniques, the magnetocaloric effect (MCE) and specific heat(C) measurements, which measure entropy and sensitive to any phase transition irrespective of the type of the order parameter. The state-of-art experimental capability in IMGSL; high-field calorimetry in magnetic fields up to 60 T and low temperatures down to 0.5 K, enabled observation of quantum spin-nematic state in volborthite.

First, we show the MCE curves obtained in the adiabatic condition, $T(H)$, in Fig. 1(a). The adiabat $T(H)$ initially decreases with increasing fields, before passing a broad minimum at ~25 T and then increases at higher fields. Below 1.7 K, a notable change occurs as seen in the enlarged plot (Fig. 1(b)). The broad minimum in $T(H)$ acquires small dips, indicative of phase transitions at 22.5, 25.5 and 27.5 T. Each of these three critical fields has also been found in measurements of MCE under nearly isothermal conditions

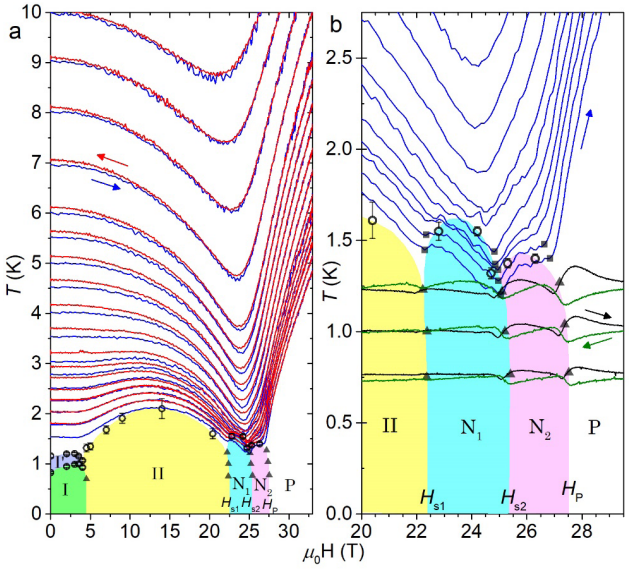

Fig. 1. Magnetocaloric effect and magnetic phase diagram of volborthite. (a) Experimental data of the MCE in volborthite. (b) Enlarged plot of MCE curve. The phase boundaries deduced from the MCE and $C(T)$ measurements were plotted by solid symbols and open circles.

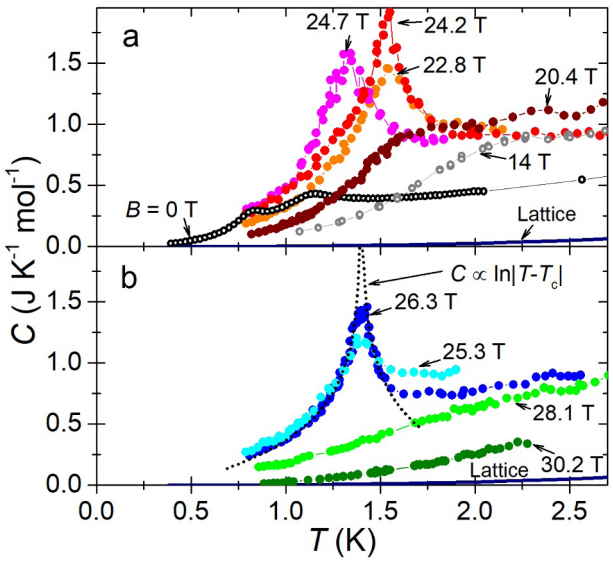

Fig. 2. Specific heat in volborthite. (a) Experimental results for specific heat $C(T)$ for magnetic fields spanning the low-field phase I, phase II (SDW), and phase N_1. (b) Specific heat within the hidden-order phase N_2 and the plateau state P.

as shown in Fig. 1(b) as black and green curves. In Fig. 1(b), we also plot the phase boundary deduced from MCE and $C(T)$ measurements.

We have further investigated the temperature-dependence of C in magnetic fields up to 30.2 T as seen in Fig. 2. In the absence of magnetic field, $C(T)$ exhibits small peaks as reported previously (See Fig. 2(a)). The onset of SDW order (Phase II) is also revealed as a broad shoulder in $C(T)$. Different behavior is observed above 22.5T where the transition is marked by a substantial λ-shaped anomaly. An extremely sharp peak (Fig. 2(b)) is developed above 25.5 T, consistent with the phase boundary identified in MCE. Above the crossover field to the plateau state (P) at 27.5T, no anomaly is observed in $C(T)$. These observations provide unequivocal evidence that there are two different magnetic states between SDW and plateau states, i.e., Phases N_1 and N_2 as seen in Fig. 1(b). It is important to note that the earlier NMR results [2], however, failed to resolve the phase N_2. Since the spin quadrupole moment cannot be detected by conventional magnetic probes such as NMR, it is reasonable to consider the phase N_2 between 25.5 and 27.5 T is the ordered state of the quadruple moment that is so-called a quantum spin nematic state.

References

[1] Y. Kohama, H. Ishikawa, A. Matsuo, K. Kindo, N. Shannon, and Z. Hiroi, PNAS **116**(22) 10686 (2019).

[2] H. Ishikawa, M. Yoshida, K. Nawa, M. Jeong, S. Kramer, M. Horvatic, C. Berthier, . Takigawa, M. Akaki, A. Miyake, M. Tokunaga, K. Kindo, J. Yamaura, Y. Okamoto, and Z. Hiroi, Phys. Rev. Lett. **114**, 227202 (2015).

[3] O. Janson, S. Furukawa, T. Momoi, P. Sindzingre, J. Richter, and K. Held, Phys. Rev. Lett. **117**, 037206 (2016).

Authors

Y. Kohama, H. Ishikawa, A. Matsuo, K. Kindo N.Shannon[a], and Z. Hiroi

[a]Okinawa Institute of Science and Technology Graduate University

Magnetization Process of the Breathing Pyrochlore Magnet $CuInCr_4S_8$ in Ultrahigh Magnetic Fields up to 150 T

Kohama Group

Breathing pyrochlore magnets with an alternating array of small and large tetrahedra have recently attracted attention because of their potential realization of exotic magnetic states. One promising candidate is the S = 3/2 chromium spinel oxide, $LiInCr_4O_8$, characterized by the small breathing factor J'/J~0.1, where J and J' are the exchange interactions on the small and large tetrahedra, respectively (inset of Fig. 1) [1]. In this system, the spin-lattice coupling (SLC) as well as the breathing factor govern its magnetic properties, as represented by a tetramer-singlet formation [1] and a field-induced transition to a 1/2-magnetization plateau phase [2]. Another intriguing system is the sulfide, $CuInCr_4S_8$, where the antiferromagnetic (AFM) J and the ferromagnetic (FM) J' coexist [3]. As shown in Fig. 1, the previously reported M-H curves at 1.4 K (orange and cyan lines for up and down sweeps, respectively) show a metamagnetic behavior with a large hysteresis loop at around H_{c1}=20~40 T, while M reaches only 45 % of the saturation magnetization of ~3.06 μ_B/Cr at 73 T [3].

In this work, we performed magnetization measurements on a polycrystalline powder sample of $CuInCr_4S_8$ by using a single-turn coil system. The observed M-H curve and its derivative dM/dH at 5 K up to 150 T are shown in Fig. 1 (red and blue lines for up and down sweeps, respectively) [4]. Remarkably, a wide 1/2-plateau emerges from H_{c2} ~ 65 T

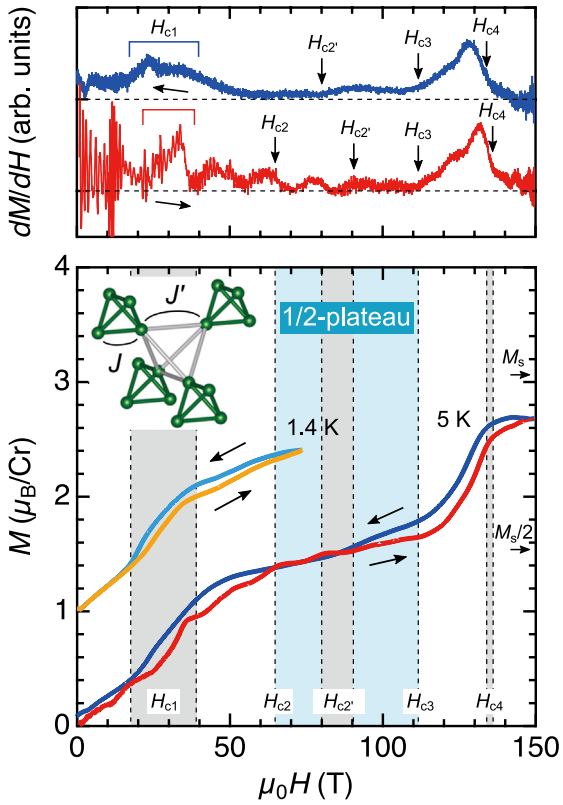

Fig. 1. M-H curves of $CuInCr_4S_8$ measured at ~5 K in a single-turn coil megagauss generator up to 150 T (red and blue curves for up and down sweeps, respectively). Derivatives dM/dH are shown in the upper panel. The previously reported M-H curve measured at 1.4 K up to 73 T are also shown (orange and cyan curves for up and down sweeps, respectively) [3]. Transition fields are denoted by brackets or arrows in the upper panel, and drawn by the shaded areas (first order) or dashed lines (second order) in the lower panel. Inset shows the schematic of the breathing pyrochlore lattice.

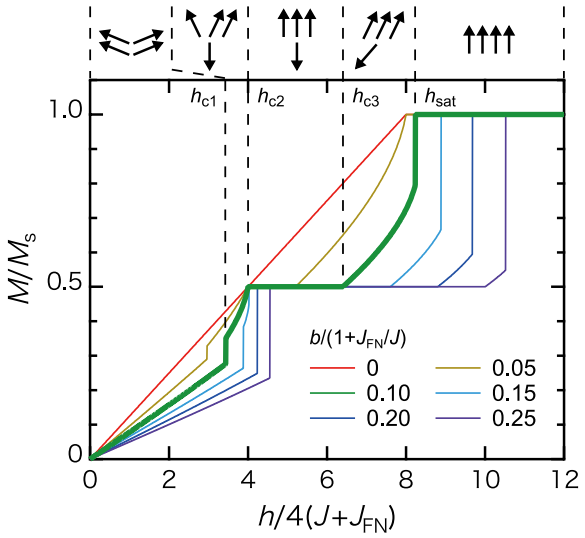

Fig. 2. Calculated magnetization curves as a function of magnetic field h for $b/(1 + J_{FN}/J) = 0$ to 0.25 in steps of 0.05. The spin structures corresponding to the curve for $b/(1 + J_{FN}/J) = 0.10$ (thick green line) are shown in the upper part of the figure.

to H_{c3} ~ 112 T as in Cr spinel oxides. Besides, two inherent features are observed: A slight change in the slope of the *M-H* curve at $H_{c2'}$ ~ 85 T and a shoulder like shape at H_{c4} ~ 135 T. Both are accompanied by a hysteresis, suggesting first-order transitions. The saturation is estimated to H_{sat} ~ 180 T under the assumption that *M* increases linearly above 150 T, where *M* already reaches ~2.7 μ_B/Cr.

For interpreting the observed magnetization process, we constructed an effective spin model mapped onto the fcc lattice, which is derived from the microscopic spin model on the breathing pyrochlore lattice with the SLC as proposed in Ref. [5]. Figure 2 summarizes the calculated *M-H* curves for given values of the SLC parameter *b* and the corresponding spin structures. In spite of the simplification in our model, the calculation well reproduces the main feature of the *M-H* curve of $CuInCr_4S_8$, including a relatively wide intermediate (canted 2:1:1) phase as well as the 1/2-plateau phase with collinear 3:1 spin configuration.

It is noteworthy that the *M-H* curves of $LiGaCr_4S_8$ and $LiInCr_4S_8$, where the FM interaction *J'* is expected to be strong, do not exhibit the 1/2-plateau [3]. Bearing this in mind, the exotic magnetic behaviors on $CuInCr_4S_8$ can be attributed to the relatively dominant AFM interactions $J+J_{FN}$ compared to the FM *J'*, which is achieved only by the moderate breathing distortion in the Cr spinel sulfide. On the other hand, the origins of the hysteretic behaviors on $CuInCr_4S_8$ at $H_{c2'}$ and H_{c4} remain unsolved at the moment. They might originate from the interplay between the SLC and the further neighbor interactions J_{FN}, or the thermal and quantum effects, which are not considered in the present theory. The macroscopic spin structures beyond four sites within small tetrahedra should also be clarified, which is crucial to prove the novelty of the magnetic properties in $CuInCr_4S_8$. Further experimental investigations such as magnetostriction, ESR, and magnetocaloric effect measurements in high magnetic fields are ongoing to elucidate the essence of the successive phase transitions.

References

[1] Y. Okamoto, G. J. Nilsen, J. P. Attfield, and Z. Hiroi, Phys. Rev. Lett. **110**, 097203 (2013).
[2] M. Gen, D. Nakamura, Y. Okamoto, and S. Takeyama, J. Magn. Magn. Mater. **473**, 387 (2019).
[3] Y. Okamoto, M. Mori, N. Katayama, A. Miyake, M. Tokunaga, A. Matsuo, K. Kindo, and K. Takenaka, J. Phys. Soc. Jpn. **87**, 034709 (2018).
[4] M. Gen, Y. Okamoto, M. Mori, K. Takenaka, and Y. Kohama, Phys. Rev. B **101**, 054434 (2020).
[5] K. Aoyama and H. Kawamura, Phys. Rev. B **99**, 144406 (2019).

Authors

M. Gen, Y. Okamoto[a], M. Mori[a], K. Takenaka[a], and Y. Kohama
[a]Nagoya University

Femtosecond Laser Pulse Generation with 20-GHz Repetition Rate

Kobayashi Group

Femtosecond laser pulses have widely used in the field of spectroscopy, metrology and material processing. Especially, material processing using the femtosecond laser has played an important role in the manufacturing because it does not induce thermal damages around the processing area, resulting in the high-quality micro-processing. One important laser parameter for these applications is a pulse repetition rate, which is typically in the range of 1 kHz to 100 MHz. Recent progress of the laser technologies has succeeded to generate femtosecond laser pulses with the gigahertz repetition rate. These high repetition rate pulses have performed efficient material processing compared with the low repetition rate laser pulses. Although the high repetition rate pulses are one candidate of the next-generation laser processing, mechanisms of the efficient material removal have not understood ever before. One reason is a lack of the multi-GHz femtosecond laser sources. Especially, material removal via laser pulses with the repetition rate above 10-GHz have not examined due to the difficulty of generating the multi-GHz laser pulses. We are interested in the generation of such kind of laser pulses.

Several methods have been used to generate multi-GHz repetition rate pulses. We focused on the Kerr-lens mode locked laser (KML), which provides the shortest pulse duration in the femtosecond lasers. The repetition rate of the KML is determined by the cavity length, with the relation of $f = c/L$, where f denotes the pulse repetition rate, c is the speed of the light and L is the cavity length. Therefore, the higher repetition rate is achieved with a shorter cavity length. To date, KML has realized up to 15 GHz repetition frequencies with a pulse duration of 150 fs. This repetition frequency corresponds to a cavity length of 20 mm. To increase the repetition rate above, the cavity length must be shorter than 20 mm. However, the cavity length is limited by the size of the optical element. In addition, typical KML is configured with 5 to 7 optical component, resulting in a large cavity.

In this work [1], we developed the KML with the repletion rate above 20 GHz only using three optical components. This was achieved by designing new cavity geometry, which includes a triangle-cut laser gain medium and multi-

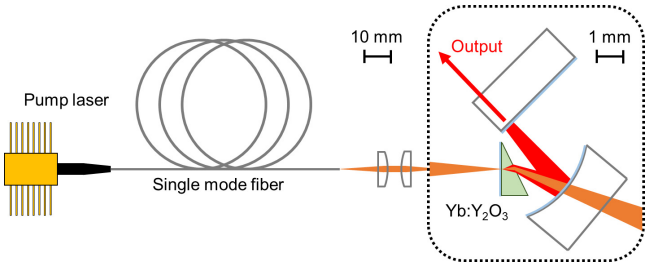

Fig. 1. The cavity geometry

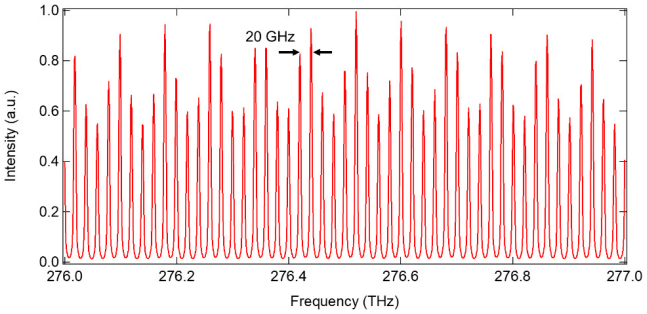

Fig. 2. A part of the output spectrum

functional dielectric coating. The detail cavity configuration is described in Figure 1. We use a gain medium of Yb:Y2O3 ceramic because an output light can be easily amplified by using a Yb-doped fiber amplifier. The pump source was an wavelength-stabilized laser diode coupled to a single mode fiber. One side of the gain medium was coated with a dichroic chirped mirror, while the other side was wedged at the Brewster angle. The concave mirror was dichroic-coated and its angle compensated an astigmatism that was introduced by the Brewster-cut gain medium. The plane mirror was high-reflection coated and was used as the output coupler.

Femtosecond pulse generation was achieved with the cavity length of 15 mm, which determines the pulse repetition rate as 20 GHz. A pulse duration was measured as 120 fs. The pulse repetition rate corresponds to the spacing of longitudinal cavity mode, which can be identified from the optical spectrum. Figure 2 shows a part of the optical spectrum. Each longitudinal mode is clearly observed because the mode spacing is wider than a spectrometer resolution of 4 GHz. To the best of our knowledge, the repetition rate of 20 GHz is the highest frequency in KMLs. Our results will enable the investigation of the material processing above the 10-GHz repetition rate.

Reference
[1] S. Kimura, S. Tani, and Y. Kobayashi, Optica **6**, 532 (2019).

Authors
S. Kimura S. Tani, and Y. Kobayashi

Geometrical Frustration of B-H Bonds in Layered Hydrogen Borides Accessible by Soft Chemistry

I. Matsuda Group

Electrically conducting materials have been essential elements for devices and also for redox reactions on electrodes to sustain our electronic and information society. Miniaturizations in nanotechnology have demanded to reduce the material size down to the atomic limit, however, there are only a few conducting atomic layers, such as graphene, up to now. A search of a novel atomic layer is significant to produce new physical/chemical properties and also to promote various functionalities by combining different types of layers.

In 2017, atomic sheets of hydrogen boride (HB) or borophene are synthesized by the ion-exchange process [1]. The HB sheet has been theoretically predicted to be conducting. However, preliminary experiments of the transport measurement have resulted in insulating properties. This fact has lead experimentalists to take great efforts of improving the purity of the samples to develop the conductivity. Eventually, in the present research [2], high-purity HB sheets were successfully synthesized, as shown in Fig. 1(a), and achieved the highest conductivity in hydrogen borides (0.13 S/cm). Moreover, suppression of the conductivity in previous samples were found to be due to adsorption of residual organic molecules on the sheet. Interestingly, the HB sheet becomes insulating at 30 °C when there are residual molecules and, reversely, returns to have high conductivity below the temperature, as shown in Fig. 1(b).

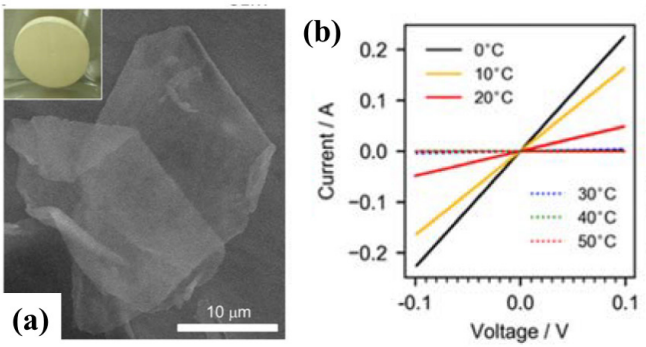

Fig. 1. (a) An image of scanning electron microscope of the hydrogen boride sheet. (b) Current-voltage curves acquired at various temperatures of the sheet [2].

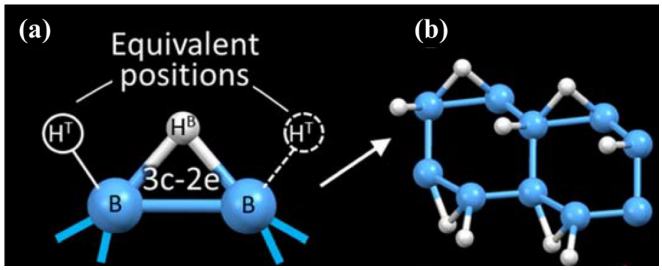

Fig. 2. Atomic structure model of the special local structure in the hydrogen boride sheet [2].

To reveal the intriguing phenomena in terms of the atomic structure, an X-ray scattering experiment was carried out at the synchrotron radiation facility, SPring-8. By analyzing the experimental pair distribution function with the Bayesian optimization, it became clear that there are locally special arrangements of hydrogen atoms in the sheet that allow adsorptions of the residual organic molecules. Figure 2 shows the atomic model. The structure consists of three-center, two-electron (3c-2e) B-H-B bridging bonds as well as ordinary two-center, two-electron (2c-2e) B-H terminal bonds. The present research revealed that conductivity of atomic sheets of hydrogen boride can be regulated by the tiny number of molecules, indicating promising functionalities in sensors or in catalysts.

References
[1] H. Nishino, T. Fujita, N. T. Cuong, S. Tominaka, M. Miyauchi, S. Iimura, A. Hirata, N. Umezawa, S. Okada, E. Nishibori, A. Fujino, T. Fujimori, S. Ito, J. Nakamura, H. Hosono, and T. Kondo, J Am Chem Soc. **139**, 13761 (2017).
[2] S. Tominaka, R. Ishibiki, A. Fujino, K. Kawakami, K. Ohara, I. Matsuda, H. Hosono, and T. Kondo, Chem **6**, 406 (2020).

Authors
S. Tominaka[a,b], I. Matsuda, and T. Kondo[c,d]
[a]International Center for Materials Nanoarchitectonics (MANA), National Institute for Materials Science (NIMS)
[b]Japan Synchrotron Radiation Research Institute
[c]Tokyo Institute of Technology
[d]University of Tsukuba

Ultrafast Unbalanced Electron Distributions in Quasicrystalline 30° Twisted Bilayer Graphene

I. Matsuda, Okazai, and Komori Groups

Layers of twisted bilayer graphene exhibit varieties of exotic quantum phenomena and the twist angle Θ has become an important degree of freedom for exploring novel states of matters. At Θ = 1.1°, the two-dimensional superconductivity was observed, while, at Θ = 30°, a two-dimensional quasicrystal is synthesized. For the quasi-crystalline twisted bilayer graphene (QCTBG), the interlayer interaction is the minimum due to the 30° twisted angle and the massless Dirac Fermions remain in the two layers. The electronic state results in the twelve-fold (dodecagonal) structure and it is composed of upper- and lower-layer Dirac cones, ULDs and LLDs, as shown in Fig. 1.

We explored this electronic structure by focusing on the ultrafast dynamics through time- and angle-resolved photoemission spectroscopy (TARPES), which allows us to directly observe the temporal evolution of fermions in the Dirac cones [1]. The measurement used the pump-probe approach with an infrared pulse with $h\nu$ = 1.55 eV serving as pump and an extreme-ultraviolet pulse with $h\nu$ = 21.7 eV serving as a probe to cover the entire two-dimensional Brillouin zone. Figure 2 shows a summary of the TARPES band diagrams taken at selected delay time for the ULD and LLD bands in a TBG quasicrystal. The results of the periodic non-twisted bilayer graphene (NTBG) are also shown for comparisons. After the pump pulse (intensity ~0.7 mJ/cm^2), the TARPES band diagram of individual bands of bilayers evolves on the femtosecond time scale. To enhance the temporal variations, the band diagrams are shown as the difference between the spectra before and after photoexcitation. The spectral weights for all bands decrease immediately below μ_{eq} and increase above μ_{eq} at Δt= 0.05 ps. This reflects the excitation of electrons from the occupied bands to the unoccupied bands. At Δt= 0.16 and 0.32 ps, the difference intensity decreases with delay time, which corresponds to the relaxation of photoexcited carriers.

To evaluate the occupation of Dirac cones by nonequilibrium carriers, we made energy distribution curves of the Dirac bands by integrating over momentum space and summarized the chemical-potential shift or the photo-induced potential as Fig. 3. As shown in the figure, the different time evolution for potential indicates that the ULD and LLD bands have the opposite behavior after Δt = 0.2 ps (*i.e.* the ULD undergoes a negative shift whereas the LLD undergoes a positive shift). Interestingly, the photo-induced potential for the NTBG band remains constant at essentially zero over the same time delay. The striking difference among the three types of the Dirac cones provides clear evidence of a carrier imbalance between the ULD and LLD bands of the QCTBG on the ultrafast time scale. Through the kinetic analysis, the key mechanism was found to involve the carrier transport between layers and the transient doping from the substrate interface. Our TARPES measurements on replicas of the ULD and LLD bands, shown in Fig.1, revealed that the ultrafast dynamics scheme continues after the Umklapp scattering. The dynamics in the atomic layer opens the possibility of new applications and creates interdisciplinary links in the optoelectronics of van der Waals crystals.

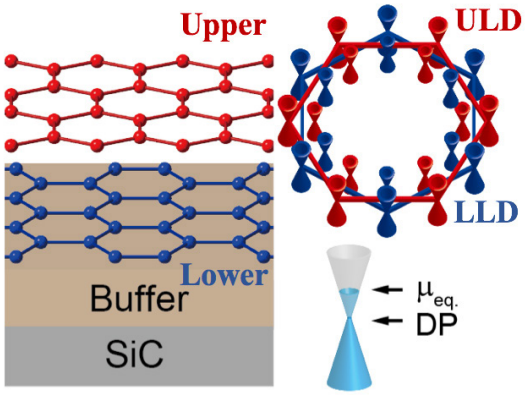

Fig. 1. Crystal and electronic structure of a twisted bilayer graphene quasicrystal on the SiC substrate. The upper- and lower-layer graphene sheets are twisted by 30 degrees with respect to each other. In the momentum space, electronic structure of a TBG quasicrystal is composed of the upper-layer Dirac (ULD) and lower-layer Dirac (LLD) bands. The inner-red and blue Dirac cones represent the replica bands of ULD and LLD bands by the umklapp scattering induced by the incommensurate interlayer stacking of the quasi-crystallinity. The quasi-crystalline twisted bilayer graphene was n-type: Dirac point and equilibrium chemical potential are denoted as DP and μ_{eq}, respectively.

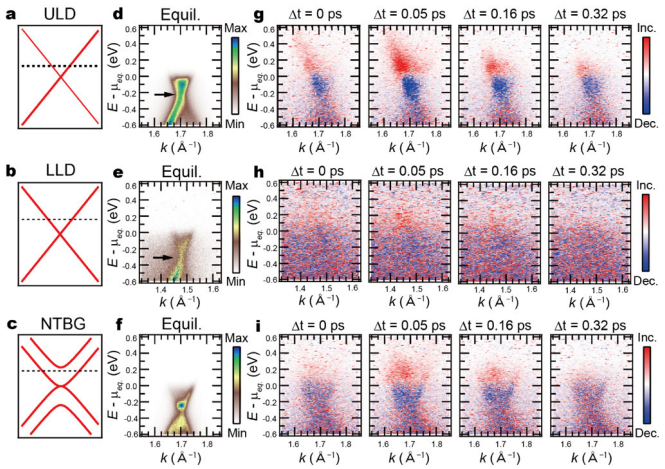

Fig. 2. Calculated band structures for the ULD and LLD bands in QCTBG and for non-twisted bilayer graphene (NTBG) band, respectively. Dashed lines indicate the μ_{eq} level. **d–f,** Equilibrium angle-resolved photoemission spectra for ULD, LLD, and NTBG bands. DP is indicated by an arrow. **g–i,** Difference images of TARPES for the ULD, LLD, and NBLG bands. Red and blue points represent increasing and decreasing photoemission intensity, respectively.

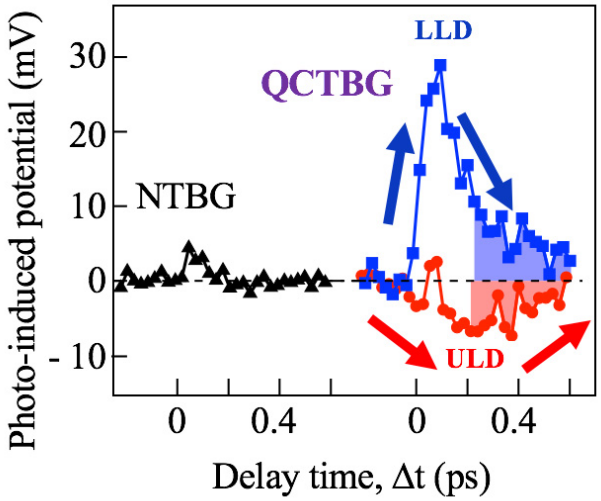

Fig. 3. Chemical-potential shift as a function of pump-probe delay time for LLD and ULD bands for QCTBG. For comparison, the result for NTBLG is also shown.

Reference
[1] T. Suzuki, T. Iimori, S. J. Ahn, Z. Yuhao, M. Watanabe, J. Xu, M. Fujisawa, T. Kanai, N. Ishii, J. Itatani, K. Suwa, H. Fukidome, S. Tanaka, J. R. Ahn, K. Okazaki, S. Shin, F. Komori, and I. Matsuda, ACS Nano **13**, 11981 (2019).

Authors
I. Matsuda, T. Suzuki, K. Okazaki, and F. Komori

Photoinduced Hydrogen Release from Hydrogen Boride Sheets

I. Matsuda Group

Materials consisting of one atomic layer, such as graphene, are one of the two-dimensional materials that have shown various physical and chemical properties that are different from ordinary ones. Recently, novel atomic layers of boron, so-called "borophene", were reported and the materials were found to surpass the performance of graphene by theoretical works. However, the growth requires special conditions such as appropriate metal substrates, high temperature and ultra-high vacuum.

Under these circumstances, we have succeeded in synthesizing a hydrogen boride (HB) sheet (Fig. 1(a)), which is hydrogenated borophene or borophane, under the ambient condition. Since the HB sheet is composed only of the light elements, boron and hydrogen, the mass hydrogen density is as high as 8.5%, and it was expected to be applied as a safe and lightweight material for the hydrogen carrier that replaces the conventional high-pressure hydrogen gas cylinder with a risk of explosion. However, it has required to consider a procedure to extract hydrogen atoms/molecules from the sheet before the actual use. In the present research, we designed and verified the hydrogen release by the light irradiation [1].

According to the first-principles calculation of the hydrogen boride sheet, the optical transition ($\alpha \rightarrow \beta$) occurs from the bonding orbital of boron to the antibonding orbital, as shown in Fig. 1(b). On the other hand, there is also an optical transition ($\alpha \rightarrow \gamma$) to the antibonding orbital of hydrogen. Since this transition energy corresponds to a photon energy of ultraviolet (UV) ray, it is hypothesized that hydrogen could be released from a hydrogen boride sheet only by the UV irradiation even under the ambient condition.

The experimental verification was made by analyzing the gas molecules emitted from the hydrogen boride sheets with using two types of light sources. One type of the sources irradiates visible light that can cause the optical transition ($\alpha \rightarrow \gamma$), while the other type irradiates ultraviolet light that can induce the optical transition ($\alpha \rightarrow \beta$). As shown in Fig. 2, it was confirmed that the hydrogen gas was generated by exposure of the ultraviolet ray. By quantifying the amount

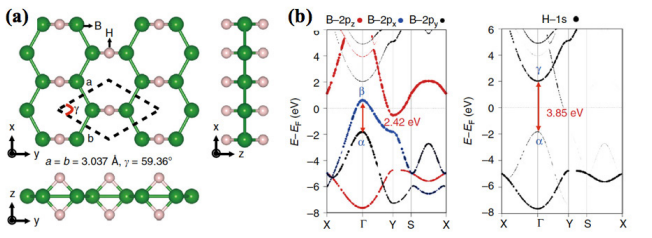

Fig. 1. (a) Top and side views of the atomic structure of the HB sheet. The unit cell is indicated by the dashed lines. (b) Projected band structures of B- and H-originated orbitals [1].

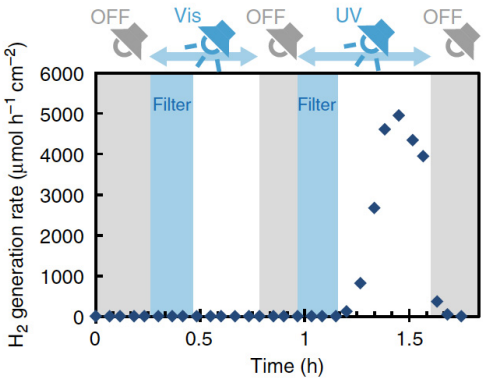

Fig. 2. A amount of H_2 production by the light irradiation with two different light sources [1].

of the hydrogen production, it was found that 8% of the mass of the hydrogen boride sheet was consumed for the hydrogen release. For conventional hydrogen storage alloys, the mass hydrogen density is up to 2%. Even a promising hydrogen carrier of the organic hydrides reaches mass hydrogen density of 6.2% with heating above 300 °C. Thus, the hydrogen boride sheet can be a safe, lightweight and simple portable hydrogen carrier with a simple light operation of the extremely high hydrogen release.

Reference
[1] R. Kawamura, N. T. Cuong, T. Fujita, R. Ishibiki, T. Hirabayashi, A. Yamaguchi, I. Matsuda, S. Okada, T. Kondo, and M. Miyauchi, Nature Commun. **10**, 4880 (2019).

Authors
I. Matsuda, T. Kondo[a,b], and M. Miyauchi[c]
[a]Tokyo Institute of Technology,
[b]University of Tsukuba
[c]Tokyo Institute of Technology

Surface-State Coulomb Repulsion Accelerates a Metal-Insulator Transition in Topological Semimetal Nanofilms

I. Matsuda, Sugino, and Komori Groups

By reducing the size of materials in the microscopic scale, the electronic states are governed by the rules of quantum mechanics and the various quantities, such as energy levels, take discrete values (the quantum size effect, QSE). Thus, there can be a case that gapless metal films become insulating at the nanoscale. Such a QSE-induced transition into an insulating phase in semimetallic nanofilms was predicted more than half a century ago on bismuth (Bi) films [1]. Despite the researches of spectroscopy and transport experiments, the previous results have remained contradictions, indicating an interesting mechanism behind.

In the present research, we revealed an unexpected mechanism of the transition in Bi by combining of high-resolution measurements of angle-resolved photoemission spectroscopy (ARPES) on high-quality films and the density-functional theory (DFT) calculations [2]. Figure 1 (a) shows peak-enhanced ARPES images resolving all quantized bulk bands and surface bands. One can see that the top quantized levels are clearly shifting below the Fermi level with decreasing thickness. This is the first direct observation of the QSE-induced transition into an insulating phase in Bi films.

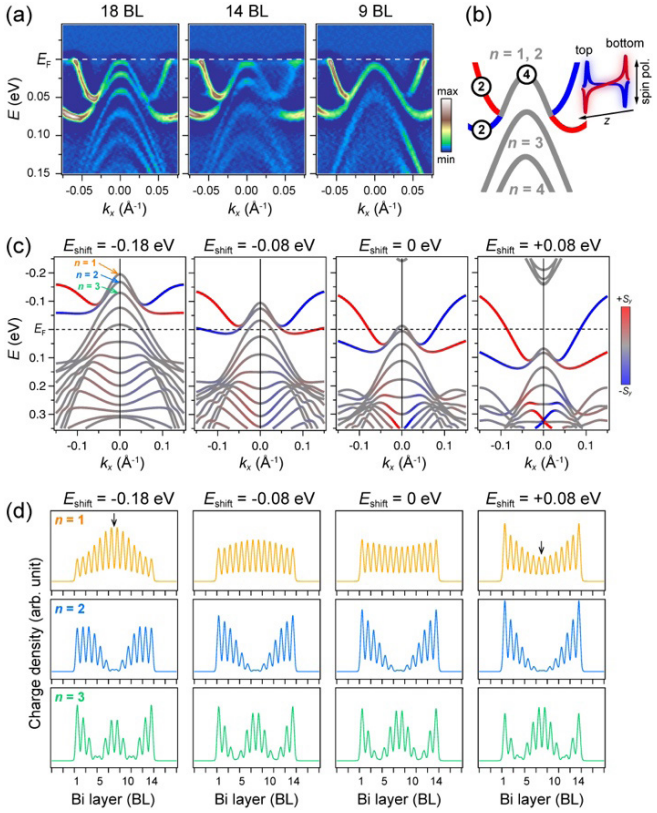

Fig. 1. (a) Peak-enhanced ARPES images measured on atomically thin Bi films. 1 bilayer (BL) of Bi corresponds to 3.9 Å. (b) Schematic of unusual band connections. The number indicates degeneracy of each band. (c) DFT band structures calculated on a 14 BL Bi slab with energy shifts manually induced. (d) Wave function characters calculated for n = 1, 2, 3 quantized states.

The high-resolution ARPES observation reveals an unusual signature: both of two surface bands connect to the top quantized bulk band. Because of the presence of surface states at the top and bottom of a film, these surface bands are doubly degenerate. Thus, this band connection readily means that the top quantized level must be quadruply degenerate. Although this breakup of conventional quantization rule was totally unexpected, our first-principles calculations reproduced the behavior. In Fig. 1(c) shows band structures that are intentionally shifted via modulation of lattice parameters. In the leftmost panel, quantized energy levels are regularly ordered, and n = 1, 2, 3 states possess wave function characters expected for ones confined in an ideal quantum well. From the leftmost to the rightmost panels, the separation between n = 1 and 2 levels is gradually reduced, and the wave function characters divert from the ideal cases and get localized near surfaces.

What is the essential mechanism for the unexpected level degeneracy and the bulk-to-surface transformation of quantized wave functions? In the DFT framework, an effective one-body potential and a total charge density are determined by a self-consistent cycle reflecting Coulomb interaction. From left to right in Fig. 1(c), the occupation of the surface bands increases and their relative contributions to the total charge density increase.

This tendency makes Coulomb repulsion among electrons compress the total charge density toward the film center. In the one-body picture of the DFT framework, a potential barrier around the film center is induced by this compressed total charge, which creates a double-well potential, as illustrated in Fig. 2(a). Such a double-well potential supports degenerate ground states whose wave functions are localized in both wells with opposite parity, which explains

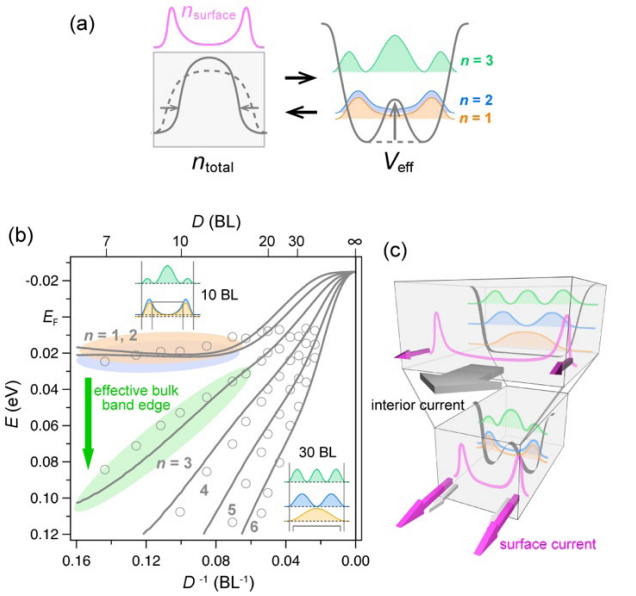

Fig. 2. (a) Schematic of a self-consistent cycle for a total charge density and an effective confinement potential. (b) Comparison of experimental thickness dependence of quantized levels (markers) and a numerical simulation (solid lines). The inset depicts wave function characters obtained in the simulation. (c) Schematics of the new class of size effects driven by increased Coulomb repulsion from surface states.

observations above. Furthermore, experimental thickness dependence of quantized levels was excellently reproduced by a numerical simulation using a single-well potential which gradually deforms into a double well (Fig. 2(b)).

This unprecedented picture naturally reconciles the strange contradiction observed in previous studies: even if the top quantized levels can cross the Fermi level, the states effectively behave as surface-conducting states, and the film interior is insulating as observed in transport experiments, as shown in Fig.2(c). Thus, we established the complete picture of the half-century problem in Bi, which demonstrates a new class of size effects driven by increased Coulomb repulsion from surface states.

References

[1] V. B. Sandomirskii, Quantum size effect in a semimetal film. *Soviet Physics JETP* **25**, 101 (1967).

[2] S. Ito, M. Arita, J. Haruyama, B. Feng, W.-C. Chen, H. Namatame, M. Taniguchi, C.-M. Cheng, G. Bian, S.-J. Tang, T.-C. Chiang, O. Sugino, F. Komori, and I. Matsuda, Science Advances **6**, eaaz5015 (2020).

Authors

S. Ito, O. Sugino, F. Komori, and I. Matsuda

Real-Time Observation of Electronic, Vibrational, and Rotational Dynamics in Nitric Oxide with Attosecond Soft X-Ray Pulses at 400 eV

Itatani Group

Attosecond science has made tremendous progress in the past two decades along with the advance of Ti:sapphire-based ultrafast laser technologies. Intense ultrashort pulses in visible and near infrared regions are now routinely produced, which allow to produce attosecond pulses in the extreme ultraviolet (EUV, photon energy <200 eV) by using the physics of high harmonic generation (HHG). Since the

maximum photon energy (or the high harmonic cut off) is scaled by the ponderomotive potential that is proportional to the square of laser wavelength, intense ultrashort-pulse IR sources are required to extend the spectral range of attosecond pulses towards the soft X-ray (SX) range. Such spectral extension of high harmonics paves a way to element-specific ultrafast spectroscopy using atomic absorption edges. The features of atomic selectivity, photon-in/photon-out methodology, and the preservation of temporal resolution on the attosecond time scale are attractive to construct attosecond transient spectroscopy that can generally be applicable to atoms, molecules, and condensed matters even in the presence of strong external fields.

Since 2008, Our group developed a carrier-envelope phase-stable ultrashort-pulse IR source that used BiB_3O_6 (BiBO) crystals as an optical parametric chirped-pulse amplification (OPCPA) medium. Because of the extremely broadband gain of BiBO-OPCPA in 1.2-2.2 μm, we successfully produced CEP-stable sub-two-cycle IR pulses (1.5 mJ, 10 fs) at a repetition rate of 1 kHz [1]. The high pressure gas cell that is filled with Ne or He gases allow to generate attosecond continua that cover nearly all of the water window.

Using the BiBO-OPCPA and a high-pressure He target (2.4 bar), we demonstrated attosecond SX spectroscopy of NO molecules that were exposed to intense IR fields as shown in Fig. 1 [2]. The output from BiBO-OPCPA (1.6 μm, 10 fs, 1.5 mJ, 1 kHz, CEP stable) was split to pump and probe pulses. The pump pulses induced field ionization, followed by multi-scale coherent dynamics in NO molecules. The probe pulses produced attosecond SX pulses that monitored the unoccupied energy levels by inner shell excitation. The transmitted SX spectra were then recorded with a grating-based spectrometer with a back-illuminated x-ray CCD camera.

Figure 2(a) shows the measured transient differential absorbance of NO (pump intensity: ~1×10^{14} W/cm^2). The static absorbance of NO without the pump pulses is shown in Fig. 2(b). The main feature in Fig. 2(a) is the appearance of upshifted absorbance of the 1s-2π peak at 402.5 eV when the IR pulse precedes the SX pulse. This upshift comes from NO^+ generated by tunnel ionization. Figure 2(c) shows the differential absorbance at 403.1 eV around the time origin (pump intensity: ~2×10^{14} W/cm^2). A step-like absorbance increase with a period of 2.7 fs (half cycle of the pump IR pulse) was observed. These steps are characteristic of tunnel ionization. Figure 2(d) shows the oscillation of the central energy of the NO^+ 1s-2π peak with a period of 14.5 ± 0.1 fs. Figure 2(e) shows the differential absorbance of the NO 1s-2π peak (pump intensity: ~1×10^{14} W/cm^2). The peak structure around 100 fs can be explained by laser-induced molecular alignment. As far as we know, this attosecond

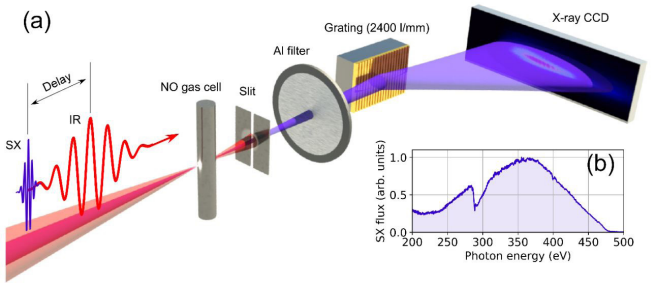

Fig. 1. (a) Schematic of the experimental setup. (b) Typical SX spectrum obtained by HHG in Helium.

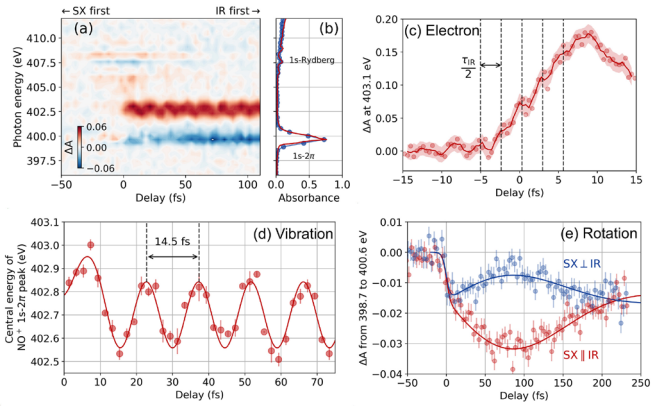

Fig. 2. (a) Time-resolved absorption spectra of NO. (b) Static absorbance of NO without the pump pulses measured in our experiment (blue circles) and a synchrotron (red curve). (c) Absorbance change of the NO^+ 1s-2π peak at 403.1 eV (red circles) and its 3-point rolling average (red curve). (d) Central energy of the NO^+ 1s-2π peak (red circles) and the fitting by a cosine and Gaussian function (red curve). (d) Absorbance change of the NO 1s-2π peak (398.7 to 400.6 eV) with parallel (red circles) and perpendicular (blue circles) IR and SX polarizations. The solid curves are calculation results considering molecular alignment. The pump intensity is ~1×10^{14} W/cm^2 for (a, b, d, e) and ~2×10^{14} W/cm^2 for (c). The polarizations of the IR and SX are parallel for (a, c, d).

transient spectroscopy is at the highest photon energy, and the first experiment to measure the field-induced alignment of molecular ions.

Attosecond transient spectroscopy of NO molecules reveals that the absorption spectra near the nitrogen K-edge (~400 eV) allow to capture full quantum dynamics (i. e., electronic, vibrational, and rotational dynamics) with a single spectrogram. These results show that attosecond soft-x-ray absorption spectroscopy is a powerful technique to trace the molecular dynamics of various freedoms in a different time and energy scales.

References
[1] N. Ishii, K. Kaneshima, T. Kanai, S. Watanabe, and J. Itatani, J. Opt. **20**, 014003 (2018).
[2] N. Saito, H. Sannohe, N. Ishii, T. Kanai, N. Kosugi, Y. Wu, A. Chew, S. Han, Z. Chang, and J. Itatani, Optica **6**, 1542 (2019).

Authors
N. Ishii, K. Kaneshima, T. Kanai, S. Watanabe[a], N. Saito, H. Sannohe, N. Kosugi[b], Y. Wu[c], A. Chew[c], S. Han[c], Z. Chang[c], and J. Itatani
[a]Tokyo University of Science
[b]Institute of Materials Structure Science, High Energy Accelerator Research Organization
[c]University of Central Florida

Efficient Terahertz Harmonic Generation with Coherent Acceleration of Electrons in the Dirac Semimetal Cd_3As_2

Matsunaga, Tsunetsugu, and Itatani Groups

Intense waveform-controlled light field has revealed highly-intriguing nonlinear and nonperturbative light-matter interactions such as high-order harmonic generation (HHG). Recently, HHG in solids with mid-infrared (IR) excitation has been reported, opening a new route toward laser-based stable and compact extreme ultraviolet (EUV) sources. Meanwhile, in the long wavelength limit, efficient third harmonic generation (THG) in the terahertz (THz) frequency regime has also been reported in a superconducting film [1]. Realization of such extreme nonlinear photonics in the

THz region at room temperature is highly desired for high-speed THz electronics and for nonlinear frequency mixing in sensitive detection of cosmic microwave background. From these perspectives, graphene has attracted tremendous attention as a candidate for efficient THz frequency multiplication using massless Dirac electrons because the current flow across the Dirac node in the momentum space is expected to exhibit remarkably large nonlinearity [2], as schematically shown in Fig. 1(a). Very recently, HHG in the THz frequency range in graphene was clearly demonstrated by using a very intense light source that is based on a large-scale electron accelerator [3]. In their experiment, the nonlinear coefficients in graphene were found to be much larger than typical materials, whereas the conversion efficiency is still limited by its monolayer nature.

In our work [4], we investigated THz nonlinear spectroscopy for thin films (thickness of 240 nm) of the three-dimensional Dirac semimetal Cd_3As_2 at room temperature using a laboratory-scale laser source. We have observed intense THz pulse generation using this laser-based setup and performed nonlinear transmission spectroscopy of quasi-monochromatic intense THz pulse with the center frequency of 0.8 THz [4]. Figure 1(b) shows the results of the spectral amplitude for transmitted pulses. A sharp peak of THG is clearly observed at 2.4 THz, which demonstrates the efficient nonlinear frequency conversion of the THz light. For comparison, we examined monolayer graphene with the same excitation condition, and also observed the THG signal. The nonlinear coefficient for graphene was estimated as ~10^{-9} m^2V^{-2}, which is consistent with the previous literature, and several orders of magnitude larger than typical materials. Compared to graphene, the conversion efficiency in Cd_3As_2 is much larger due to the film thickness, and the observed THG field amplitude is ~100 V/cm under the pump field of 6.5 kV/cm inside the film. In the next step, we can reduce the Fresnel reflection loss at the sample surface by using an antireflection coating on the film or directly applying the field via contact electrodes, which will allow to generate further stronger harmonics for realistic applications in ultrafast electronics.

To understand the efficient HHG mechanism in Cd_3As_2 in a microscopic picture, we also performed THz pump-THz probe spectroscopy. In the case of graphene, the origin of the THz HHG was successfully explained by a thermodynamic model where electrons were assumed to be in quasi-equilibrium with repeating heating and cooling processes very rapidly within the THz timescale [3]. However, such a picture of incoherent electron dynamics is essentially different from the originally proposed scheme to induce large nonlinearity in massless Dirac systems [2]. Our time-resolved THz spectroscopy in this work has revealed that the relaxation rate of the carriers in Cd_3As_2 is ~8 ps, which

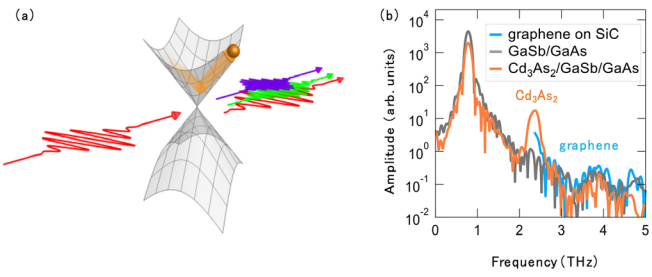

Fig. 1. (a) A schematic of high harmonic generation due to the coherent acceleration of Dirac electrons. (b) Amplitude spectra of the transmitted intense THz pulse with appearance of the THz THG in Cd_3As_2 thin film.

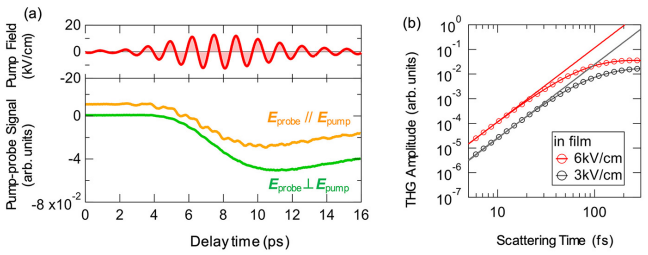

Fig. 2. (a) Pump THz field waveform (upper). THz pump-THz probe signal as a function of the pump-probe delay time with different polarization configurations. (b) Calculated THG amplitude in the intraband acceleration model as a function of the scattering time.

is much longer than one optical cycle of the pump field (1.25 ps) in contrast to the rapid cooling in graphene (<< 1 ps). We performed the thermodynamic-model calculation and confirmed that this model cannot reproduce the efficient THG with realistic parameters.

In addition, we experimentally investigated the electron dynamics during the THz wave irradiation and found that the nonlinear response manifests itself almost only for the pump polarization direction, as shown in Fig. 2(a). The result can be well explained by the intraband current model [2]. When electrons are accelerated by the pump field, the electron distribution function in the momentum space moves rapidly back and forth along with the pump polarization direction, but it appears as if "nothing happens" in other probe polarization directions, which was observed as the anisotropic nonlinearity. We also calculated the nonlinear current by considering the intraband acceleration in a simple linear dispersion model and confirmed that the intraband acceleration model can reproduce the value of the THG amplitude and its saturating behavior which we observed.

Our results show that, even though the scattering time of ~145 fs in Cd_3As_2 is still shorter than the pump field cycle of 1.25 ps, the nonlinear response is well described by the intraband current by coherent acceleration of electrons. It can be explained by the fact that asymmetric non-thermal electron population distribution in momentum space can be developed as rapidly as in ~85 fs. Figure 2(b) shows the calculated result of the THG amplitude as a function of the scattering time. If the scattering time is as long as 100 fs, the THG amplitude strongly saturates. Therefore, the scattering time of 145 fs in this material is "long enough" for nonperturbative intraband acceleration driven by the optical field of a few-kV/cm.

In future, even longer scattering times might be achieved in other topological semimetals with massless dispersion, which will allow us more efficient frequency conversion, perhaps at sub-kV/cm field strength. Our results will open a new pathway towards a novel frequency convertor in the THz frequency based on Dirac semimetals.

References

[1] R. Matsunaga *et al.*, Science **345**, 1145 (2014).
[2] S. A. Mikhailov, Europhys. Lett. (EPL) **79**, 27002 (2007).
[3] H. A. Hafez *et al.*, Nature **561**, 507 (2018).
[4] B. Cheng†, N. Kanda†, T. N. Ikeda, T. Matsuda, P. Xia, T. Schumann, S. Stemmer, J. Itatani, N. P. Armitage, and R. Matsunaga, Phys. Rev. Lett. **124**, 117402 (2020). (†: equal contribution)

Authors

B. Cheng[a,†], N. Kanda[†], T. N. Ikeda, T. Matsuda, P. Xia, T. Schumann[b], S. Stemmer[b], J. Itatani, N. P. Armitagea, and R. Matsunag[a] ([†]: equal contribution)
[a]The Johns Hopkins University
[b]University of California

Observation of Terahertz Anomalous Hall Effect in Weyl Antiferromagnet Mn_3Sn Thin Films

Matsunaga and Nakatsuji Groups

Control of magnetism has been a key issue for modern data processing and recording in spintronic devices. From the viewpoint of manipulation speed, antiferromagnets are promising materials because spin precession motion occurs typically at terahertz (THz = 10^{12} per second) frequencies, a few orders of magnitude higher than ferromagnets. Readout of the magnetization information in antiferromagnets is, however, still very difficult since they are generally not sensitive to the external field because of the much smaller net magnetization than in ferromagnets, which has made their practical application challenging. In 2015, Nakatsuji group in ISSP has discovered large anomalous Hall effect (AHE) in an antiferromagnet Mn_3Sn at room temperature comparable to ferromagnets in spite of the vanishingly-small net magnetization [1]. The exceptionally-large response originates from an inverse-triangular spin structure where the spins form a 120-degree order with negative vector chirality in the ab plane. Such noncollinear antiferromagnetic spin order in the Kagome bilayer is characterized by cluster magnetic octupole moments, which macroscopically breaks time-reversal symmetry. Deep understanding of the dynamical properties of Mn_3Sn in the THz frequency range is highly desired for ultrafast readout of the antiferromagnetic spin order to develop novel functional devices.

In another point of view, Mn_3Sn has also been interested as a possible candidate for Weyl semimetals with broken time-reversal symmetry, or "Weyl (antiferro)magnets", which host massless electron dispersions with opposite chirality in the vicinity of the Fermi energy [2]. Since the ac anomalous Hall effect is directly related to the interband excitation across the Weyl nodes, a number of theoretical efforts have been recently devoted to investigating the ac anomalous Hall conductivity in $\sigma_{xy}(\omega)$ Weyl semimetals. Investigating $\sigma_{xy}(\omega)$ experimentally is therefore important for understanding novel electromagnetic responses related with the Berry curvature in Weyl semimetals.

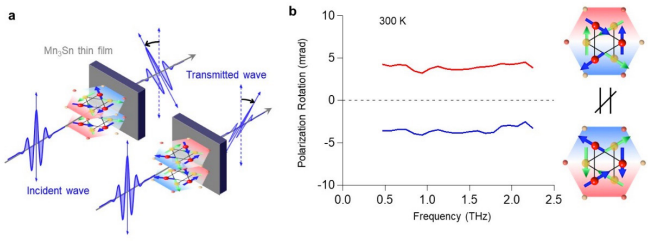

Fig. 1. (a) A schematic of THz wave polarization rotation in Mn3Sn thin films depending on the antiferromagnetic spin order. (b)The experimental results of the polarization rotation spectra with different antiferromagnetic spin orders.

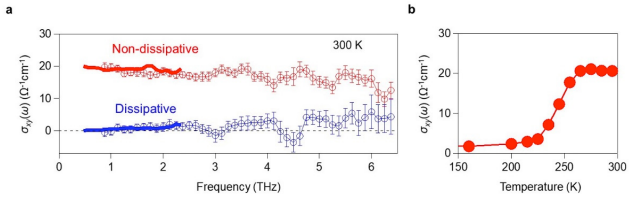

Fig. 2. (a) Frequency dependence of real- and imaginary-part anomalous Hall conductivity, indicating non-dissipative and dissipative part, respectively. (b) Temperature dependence of the real-part anomalous Hall conductivity.

Frequency dependence of the AHE can be observed in an optical method by measuring the polarization rotation of transmitted light. It is based on the relation between $\sigma_{xy}(\omega)$ and the polarization rotation angle $\theta(\omega)$:

$$\theta(\omega) + i\eta(\omega) = \frac{\sigma_{xy}(\omega)Z_0 d}{1 + n_s + \sigma_{xy}(\omega)Z_0 d}$$

where $\eta(\omega)$ an ellipticity angle, d the film thickness, Z_0 the vacuum impedance, n_s the substrate refractive index, and σ_{xx} the longitudinal conductivity. In the present work, we developed polarization-resolved THz time-domain spectroscopy setups with precise polarization resolution up to 0.05 mrad in 0.5-2.0 THz frequency window for 20-min accumulation time [3]. Figure 1(a) shows a schematic of our measurement. Using Mn_3Sn thin films with 50-200 nm thicknesses [4], we clearly observed the polarization rotation of transmitted THz wave at room temperature and zero magnetic field as shown in Fig. 1(b), depending on the direction of the cluster magnetic octupole moments. The result quantitatively agrees with the large AHE previously reported in the DC resistivity measurement.

We also performed the polarization-resolved THz spectroscopy with broad band frequency range up to 6 THz (25 meV) [3]. Figure 2(a) shows the result of real- and imaginary-part $\sigma_{xy}(\omega)$, corresponding to the non-dissipative and dissipative Hall current, respectively. The results demonstrate small dissipation in the AHE up to THz frequencies, which is consistent with an intrinsic origin of it. Figure 2(b) shows the temperature dependence of $\sigma_{xy}(\omega)$. The strong suppression of $\sigma_{xy}(\omega)$ below 250 K is consistent with the spin-reorientation phase transition from the inverse-triangular structure to a helical spin ordering along the c-axis. The development of the helical spin ordering along the c-axis recovers the macroscopic time-reversal symmetry, which results in the disappearance of the AHE.

The observation of the THz AHE at room temperature demonstrates the ultrafast readout for the antiferromagnetic spintronics using Mn_3Sn. Our all-optical approach in a noncontact way with picosecond time resolution also opens a new avenue for studying nonequilibrium dynamics in Weyl antiferromagnets.

References

[1] S. Nakatsuji, N. Kiyohara, and T. Higo, Nature **527**, 212 (2015).
[2] K. Kuroda *et al.*, Nature Mater. 16, 1090 (2017).
[3] T. Matsuda, N. Kanda, T. Higo, N. P. Armitage, S. Nakatsuji, and R. Matsunaga, Nature Commun. **11**, 909 (2020).
[4] T. Higo, D. Qu, Y. Li, C. L. Chien, Y. Otani, and S. Nakatsuji, Appl. Phys. Lett. **113**, 202402 (2018).

Authors

T. Matsuda, N. Kanda, T. Higo[a], N. P. Armitage[b], S. Nakatsuji, and R. Matsunaga
[a]CREST, Japan Science and Technology Agency
[b]The Johns Hopkins University

Photoinduced Possible Superconducting State with Long-Lived Disproportionate Band Filling in FeSe

Okazaki Group

Photoexcitation is a very powerful way to instantaneously drive a material into a novel quantum state without any fabrication, and variable ultrafast techniques have been developed to observe how electron, lattice, and spin degrees of freedom change. One of the most spectacular phenomena is photoinduced superconductivity, and it has been suggested in cuprates that the transition temperature T_c can be enhanced from the original T_c with significant lattice modulations.

Here, we demonstrate the possibility for another photo-induced high-T_c superconducting state in the iron-based superconductor FeSe using time- and angle-resolved photoemission spectroscopy (TARPES) [1]. We find that a photo-induced superconducting gap appears as a result of significant lattice modulation. Our demonstration of how we can change electron- as well as lattice-structure in FeSe by strong photo-excitation provides important insight into the next-generation devices using photo-induced superconductors, e.g. ultrafast switches or quantum engineering.

Figures 1**a** and 1**b** show the time-dependent oscillatory components of the photoemission intensity integrated above the Fermi level (E_F) after photo-excitation for the hole and electron Fermi surfaces (FSs), respectively. The fits by sinusoidal functions are shown as black solid lines. The clear appearance of single cosine-like signature is noticed both for the hole and electron FSs. The frequency of this oscillation is 5.3 THz, which corresponds to the A_{1g} coherent phonon mode shown in Fig. 1**c**. Moreover, the amplitude of the oscillation significantly increases with the increase of pump fluence shown in Fig. 1**d**. These signatures indicate that the observed coherent phonons is explained by the displacive excitation mechanism, in which coherent phonons are generated as a result of the photo-induced modulation of the lattice structure.

In order to study the photo-induced electronic state in more detail, we further conducted long time-scale measurements. Figures 2**a** and 2**b** show the photo-induced leading-edge midpoint (LEM) shifts for the electron and holes FSs as a function of time and pump fluence, respectively. One can notice that the LEM shift at the hole FS is negative, while the LEM shift at the electron FS is negligibly small. This unbalanced shift is due to disproportionate band filling schematically shown in Fig. 2**c**. It is of note that the disproportionate band filling lasts for a quite long time of ~1ns owing to the indirect semimetallic band structure, where the electron-hole recombination must accompany the assistance of phonons with a large momentum.

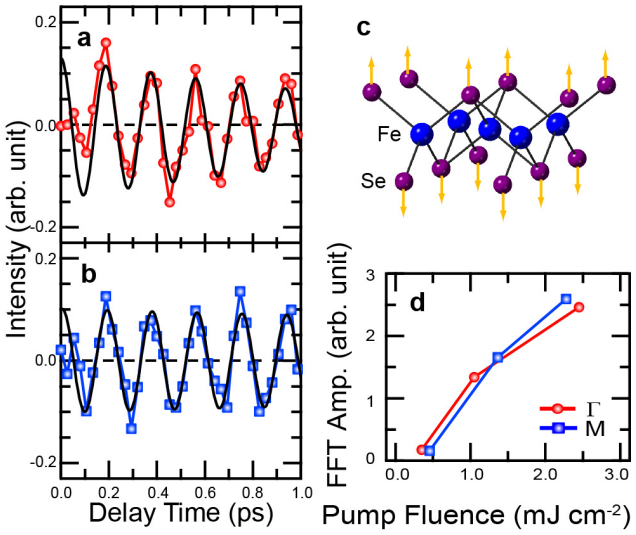

Fig. 1. **a**, **b**. Oscillatory components for the time-dependent photoemission intensities integrated above Fermi Energy for the hole and electron Fermi surfaces. **c**. Illustration of lattice modulation by photoexcitation, corresponding to A_{1g} phonon mode. **d**. Fast Fourier transform (FFT) amplitude at 5.3 THz for the hole and electron FSs as a function of the pump fluence.

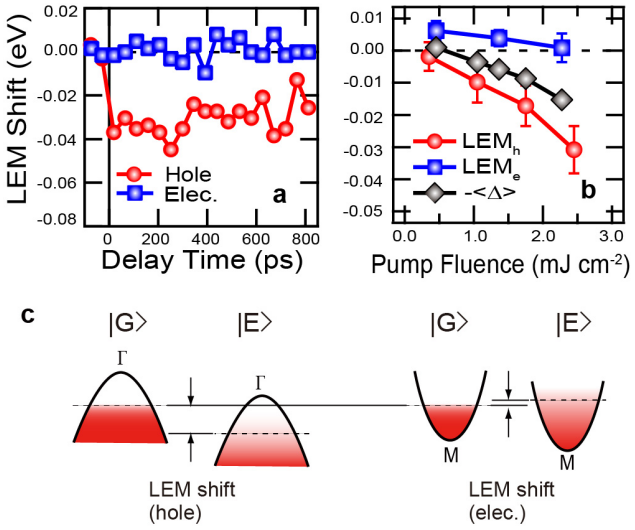

Fig. 2. **a**, **b**. Shifts of the leading-edge midpoints (LEM) as a function of time and pump fluence for the hole and electron FSs. In Fig. 2b, the averaged superconducting gap, <Δ> is shown as black solid lines and markers. **c**. Illustration of photoinduced LEM shifts for the hole (Γ) and electron (M) bands. |G> and |E> represent the ground and photoexcited states, respectively.

The origin of the disproportionate band filling is most likely ascribed to the emergence of photo-induced superconducting gap because FeSe has no other competing orders such as the anti-ferromagnetic order in the equilibrium state. To further investigate the photo-induced superconducting gap, we extract the superconducting gap and performed photo-intensity dependent measurements, as shown in Fig. 2**b**. We find that with increasing photo intensity, the superconducting gap also increases, which suggests that the enhancement of superconducting order is enabled by tuning light intensity.

In summary, our finding of the possible photo-induced superconducting state for FeSe can provide another platform of photo-induced superconductivity. The significant property in this system is the longevity of the photo-induced state, which is also called metastable. According to the report in photo-induced superconducting state in cuprates, the carrier lifetime of FeSe is more than two orders of magnitude longer than that of cuprates. In terms of device applications, this signature is quite powerful because one can perform multiple and complicated processes during this metastable state.

Reference

[1] T. Suzuki, T. Someya, T. Hashimoto, S. Michimae, M. Watanabe, M. Fujiwara, T. Kanai, N. Ishii, J. Itatani, S. Kasahara, Y. Matsuda, T. Shibauchi, K. Okazaki, and S. Shin, Communications Physics, **2**, 115 (2019).

Authors

T. Suzuki, T. Someya, T. Hashimoto, S. Michimae, M. Watanabe, M. Fujiwara, T. Kanai, N. Ishii, J. Itatani, S. Kasahara[a], Y. Matsuda[a], T. Shibauchi[b], K. Okazaki, and S. Shin

[a]Kyoto University

[b]The University of Tokyo